

Miniature Pulsed Laser Sources: Repetition Rates from Kilohertz to Gigahertz

A dissertation submitted to the
Swiss Federal Institute of Technology Zürich

for the degree of
Doctor of Natural Sciences

presented by

Reto Andreas Häring
Dipl. Phys. ETH
born on January 9, 1971
citizen of Arisdorf BL, Switzerland

Accepted on the recommendation of

Prof. Dr. Ursula Keller, examiner
Prof. Dr. Anne Tropper, co-examiner
Dr. Rüdiger Paschotta, co-examiner

December 2001

Table of Contents

LIST OF ABBREVIATIONS AND PHYSICAL SYMBOLS	III
PUBLICATIONS.....	VII
Refereed papers.....	VII
Conference Presentations.....	VIII
Various talks.....	IX
Patent	IX
ABSTRACT.....	X
KURZFASSUNG	XII
INTRODUCTION	1
PASSIVELY Q-SWITCHED MICROCHIP LASER AT 1.5 μM.....	5
1.1 Microchip laser setup	6
1.2 Operation parameters of Q-switched microchip lasers.....	8
1.3 Semiconductor saturable absorber mirror (SESAM).....	9
1.3.1 Parameters of a SESAM.....	9
1.1.2 Top reflector	10
1.1.3 SESAMs for 1.5 μm Q-switching experiments.....	12
1.1.4 Optimization of top reflector	13
1.4 Damage measurements	15
1.5 Optimized SESAM and laser performance.....	18
GAIN STRUCTURES FOR VERTICAL-EXTERNAL-CAVITY SURFACE-EMITTING	
LASERS.....	23
3.1 Design of the structure.....	25
3.2 Thermal management	30
3.2.1 Analytical temperature model	31
1.1.2 Numerical temperature simulation.....	33
1.1.3 Dependence of performance on pump spot size.....	36
1.3 Growth.....	38
1.3.1 Calibration of composition and thickness.....	39
Atomic force microscopy.....	39

X-ray diffraction	43
Transmission Electron Microscopy.....	46
1.3.2 Calibration of optical properties.....	47
Optical spectrum.....	47
Photoluminescence	49
1.1.3 Wafer inhomogeneity	50
1.4 Processing.....	51
1.4.1 Soldering.....	52
Sn/Au solder.....	52
Indium solder.....	53
1.1.2 Etching.....	55
1.5 Characterization.....	57
1.5.1 Dark line defects (photoluminescence microscopy)	57
1.1.2 Surface quality (atomic force microscopy).....	60
1.1.3 Degradation.....	62
MODE LOCKING OF VERTICAL-EXTERNAL-CAVITY SURFACE-EMITTING LASERS	
.....	65
1.1 Mode locking mechanisms	66
1.2 First demonstration.....	70
1.3 Improved laser with thinned structure.....	74
1.4 Mode locking with ELO structures.....	77
SUMMARY AND OUTLOOK.....	83
REFERENCES.....	85
DANKSAGUNG.....	99

List of Abbreviations and Physical Symbols

A	laser mode area
a	lattice constant
AFM	atomic force microscope
Al	aluminum
A_L	area of laser mode
AlAs	aluminum arsenide
AlGaAs	aluminum gallium arsenide
α	angle of incidence
APM	additive pulse mode locking
AR	anti-reflective
As	arsenic
Au	gold
c	speed of light
Ca	calcium
CCD	charge-coupled device
Co	cobalt
Cr	chromium
Cr:YAG	chromium-doped yttrium aluminum garnet ($\text{Cr}^{4+}:\text{Y}_3\text{Al}_5\text{O}_{12}$)
$\text{CuK}\alpha$	spectral line of copper with $\lambda = 1.5410 \text{ \AA}$
d	thickness of layer
Δa	difference in lattice constant for a layer on a substrate (x-ray)
d_{abs}	thickness of absorber
DBS	dichroic beamsplitter
DCXD	double crystal x-ray diffraction
Δf	frequency spacing of cavity modes
DIN	Deutsches Institut für Normierung e.V.
dp	double periodic
ΔR	modulation depth
ΔR_{AR}	modulation depth of an anti-reflective coated SESAM
ΔT_{1d}	temperature drop over material with one-dimensional heat flow
ΔT_{3d}	temperature drop over material with three-dimensional heat flow

$\Delta\theta$	diffraction angle relative to substrate peak (x-ray)
ELO	epitaxial lift-off
E_p	pulse energy
Er	erbium
Er:Yb:glass	erbium-doped (phosphate) glass with ytterbium co-doping
$E_{\text{sat, A}}$	saturation energy of absorber
$E_{\text{sat, L}}$	saturation energy of gain medium
F	fluorine
f	misfit of layer lattice on a substrate
F_{abs}	fluence on the absorber
F_{AR}	fluence on the absorber for an anti-reflective coated SESAM
F_d	damage fluence of the absorber
f_{rep}	repetition rate
F_{sat}	saturation fluence of SESAM
FWHM	full-width at half-maximum
Ga	gallium
GaAs	gallium arsenide
GaAsP	gallium arsenide phosphide
GDD	group delay dispersion
H_2O_2	hydrogen peroxide
HCl	hydrochloric acid
Hf	hafnium
HF	hydrofluoric acid
HR	high reflector
In	indium
InGaAsP	indium gallium arsenide phosphide
InGaP	indium gallium phosphide
InP	indium phosphide
κ_{1d}	thermal conductivity in material with one-dimensional heat flow
κ_{3d}	thermal conductivity in material with three-dimensional heat flow
KLM	Kerr lens mode locking
L	cavity length
La	lanthanum
λ	wavelength
Li	lithium
λ_1	laser wavelength
l_{ns}	non-saturable losses

$l_{ns,AR}$	non-saturable losses of a SESAM
L_{opt}	optical cavity length
λ_p	pump wavelength
l_{par}	parasitic losses
$m + 1$	order of Bragg reflection for pump light (mirror design)
m	order of Bragg reflection (x-ray)
M^2	beam quality factor
MBE	molecular beam epitaxy
Mg	magnesium
ML	monolayer
MOCVD	metalorganic chemical vapor deposition
n	refractive index
Nb	niobium
Nd	neodymium
Nd:YAG	neodymium-doped yttrium aluminum garnet ($Nd^{3+}:Y_3Al_5O_{12}$)
Nd:YVO ₄	neodymium-doped yttrium ortho vanadate
n_H	refractive index of high index material
NH ₄ OH	Ammonium Hydroxide
\tilde{n}_l	effective refractive index at laser wavelength
n_L	refractive index of low index material
\tilde{n}_p	effective refractive index at pump wavelength
ν	Poisson ratio
ν_L	laser frequency
O	oxygen
OC	output coupler
OPG	Optical parametric generator
OPO	optical parametric oscillator
opt	optimized
P	phosphorus
P_{av}	average output power
P_{heat}	heating power
PL	photoluminescence
QW	quantum well
QWOT	quarter wave optical thickness
QX/Er	trade mark of a phosphate glass from Kigre, Inc
R	ratio of temperature drops in semiconductor and heat sink
RF	radio-frequency

ρ	heat source
$R_{ns,AR}$	reflectivity of the saturated SESAM
ROC	radius of curvature
r, θ, ϕ	spherical coordinates
s	saturation parameter
Se	selenium
SESAM	semiconductor saturable absorber mirror
SHG	second-harmonic generation
Si	silicon
σ_L	cross-section for stimulated emission
σ_L^{abs}	cross-section for re-absorption at the laser wavelength
Sn	tin
Sn/Au	tin-gold (solder)
SPM	self-phase modulation
Sr	strontium
τ, τ_p	FWHM pulse duration
τ_A	recovery time of absorber
TEM	transmission electron microscopy
θ	angle for Bragg condition (x-ray)
Ti	titanium
Ti:sapphire	titanium-doped sapphire ($Ti^{2+}:Al_2O_3$)
Tm	thulium
T_{oc}	transmittance of the output coupler
T_t	transmittance of the top reflector of a SESAM
U	uranium
VECSEL	vertical-external-cavity surface-emitting laser
w	gaussian mode radius
w_{crit}	critical beam radius (for one-dimensional heat flow)
ξ	proportionality factor for intensities in a anti-resonant Fabry-Perot
Y	yttrium
Yb	ytterbium
Zn	zinc

Publications

Parts of this thesis are published in the following journal papers and conference proceedings:

Refereed papers

- R. Häring, A. Aschwanden, R. Paschotta, E. Gini, F. Morier-Genoud, and U. Keller,, "Passively mode-locked semiconductor laser with high power", *in preparation for Appl. Phys. B*.
- R. Häring, R. Paschotta, R. Fluck, E. Gini, H. Melchior, and U. Keller, "Passively Q-switched Microchip Laser at 1.5 μm ," *to appear in J. Opt. Soc. Am. B*, **18**, 12 (2001).
- R. Häring, R. Paschotta, E. Gini, F. Morier-Genoud, H. Melchior, D. Martin, and U. Keller, "Picosecond surface-emitting semiconductor laser with >200 mW average power," *Electron. Lett.* **37**, p766 (2001).
- S. Hoogland, S. Dhanjal, A. C. Tropper, S. J. Roberts, R. Häring, R. Paschotta, and U. Keller, "Passively mode-locked diode-pumped surface-emitting semiconductor laser," *IEEE Photon. Technol. Lett.* **12**, p1135 (2000).
- R. Paschotta, R. Häring, E. Gini, H. Melchior, U. Keller, H. L. Offerhaus, and D. J. Richardson, "Passively Q-switched 0.1 mJ fiber laser system at 1.53 μm ," *Opt. Lett.* **24**, p388 (1999).
- R. Fluck, R. Häring, R. Paschotta, E. Gini, H. Melchior, and U. Keller, "Eyesafe pulsed microchip laser using semiconductor saturable absorber mirrors," *Appl. Phys. Lett.* **72**, p3273 (1998).

Conference Presentations

- A. L. Aschwanden, R. Häring, R. Paschotta, E. Gini, F. Morier-Genoud, and U. Keller, "Passively mode-locked surface-emitting semiconductor laser with nearly 1 W average power " *submitted to Conference on Laser and Electro-Optics CLEO'02*, (Optical Society of America, Washington, D. C., 2001), 2002.
- E. Innerhofer, T. Südmeyer, F. Brunner, R. Häring, A. Aschwanden, R. Paschotta, U. Keller, C. Hönniger, and M. Kumkar, "60 W average power in picosecond pulses from a passively mode-locked Yb:YAG thin-disk laser," *submitted to Conference on Laser Electro-Optics CLEO'02*, (Optical Society of America, Washington, D. C., 2001), 2002.
- R. Häring, R. Paschotta, E. Gini, F. Morier-Genoud, H. Melchior, D. Martin, and U. Keller, "Passively mode-locked surface-emitting semiconductor laser with >200 mW average power," *in Conference on Lasers and Electro-Optics CLEO '01*, (Optical Society of America, Washington, D. C., 2001), paper CMB1, 2001.
- R. Häring, R. Paschotta, F. Morier-Genoud, U. Keller, A. Garnache, U. Oesterle, J. S. Roberts, S. Hoogland, S. Dhanjal, and A. C. Tropper, "Passively mode-locked diode-pumped surface-emitting semiconductor laser," *in Conference on Lasers and Electro-Optics*, (Optical Society of America, Washington, D. C., 2000), paper CMS1, 2000.
- R. Häring, R. Paschotta, F. Morier-Genoud, U. Keller, J. S. Roberts, S. Hoogland, S. Dhanjal, and A. C. Tropper, "Passively mode-locked diode-pumped surface-emitting semiconductor laser," *in Advanced Solid-State Lasers*, (Optical Society of America, Washington, DC, 2000), paper TuC5, 2000.
- H. L. Offerhaus, D. J. Richardson, R. Paschotta, R. Häring, E. Gini, H. Melchior, and U. Keller, "0.1 mJ pulses from a passively Q-switched fiber source," *in Conference on Lasers and Electro-Optics CLEO '99*, (Optical Society of America, Washington, DC, 2000), paper CWE8, 1999.
- R. Häring, R. Paschotta, E. Gini, H. Melchior, and U. Keller, "Sub-nanosecond pulses from passively Q-switched microchip lasers at 1.53 μm ," *in Conference on Lasers and Electro-Optics CLEO '99*, (Optical Society of America, Washington, D. C., 1999), paper CFD6, 1999.

- R. Häring, R. Fluck, R. Paschotta, E. Gini, A. Melchior, and U. Keller, "Eyesafe pulsed microchip laser using SESAMs," *Swiss Society for Optics and Microscopy / Swiss Priority Program Optics II meeting*, Neuchâtel (Switzerland), Sept. 1999.
- R. Häring, R. Fluck, R. Paschotta, E. Gini, A. Melchior, and U. Keller, "Eyesafe pulsed microchip laser using SESAMs," in *Advances in Lasers and Applications*, Summer School in Physics, SUSSP52, 1998.
- R. Häring, R. Fluck, R. Paschotta, J. Aus der Au, G. J. Spühler, and U. Keller, "Compact High-Peak-Power Laser Systems," *Swiss Society for Optics and Microscopy / Swiss Priority Program Optics II meeting*, Bern (Switzerland), 1998.

Various talks

- "Semiconductor Saturable Absorber Mirrors and their Application for a Passively Mode-Locked Diode-Pumped Surface-Emitting Semiconductor Laser" Graduiertenkolleg, Philipps-Universität Marburg, July 14, 2000
- "Eyesafe Passively Q-switched Microchip Lasers using SESAMs" Leica Geosystems AG, Heerbrugg (Switzerland), Feb. 29, 2000
- "Er:Yb:glass passively Q-switched Microchip Lasers" Leica Geosystems AG, Heerbrugg (Switzerland), Aug., 1998

Patent

- R. Paschotta, R. Häring, U. Keller, "Passively mode-locked optically pumped semiconductor external-cavity surface emitting laser," US patent application (Priority date Feb. 11, 2000)

Abstract

This thesis presents investigations on compact, pulsed lasers sources. Two approaches are explored, yielding lasers with properties covering a wide range of parameters. In both cases, we have taken care to use techniques suitable for practical applications. Consequently, the lasers are diode pumped and semiconductor saturable absorber mirrors (SESAMs) are used for the pulse formation.

A SESAM consists of an absorber layer embedded in a mirror structure. The functionality of a SESAM is based on a designed amount of loss for exposure to low intensity light while pulses with high intensities experience a high reflectivity. The choice of the semiconductor materials allows one to adapt the SESAM to the wavelength of the gain material.

With the simplest laser resonator design, the three elements needed for operation with passive pulse formation are joined together resulting in a quasi-monolithic device: Output coupler and SESAM are directly attached to the gain material from both sides to close the cavity. Depending on the SESAM parameters and the laser cavity such a laser runs in Q-switched or mode-locked mode of operation. Here we explore Q-switching with a microchip laser using an erbium-doped glass as gain material and mode locking with a multi-quantum-well semiconductor gain structure (with a slightly more complex cavity at this experimental stage).

The microchip approach is a very compact way to set up a laser ($\approx 1 \text{ mm}^3$ without the pump optics) and enables operation on a single longitudinal and transverse mode. Q-switching allows one to achieve high pulse energies at low repetition rates, as required for applications using the pulses in a time-of-flight configuration for distance measurements (e.g. three-dimensional imaging or geodesy). The wavelength at $1.5 \mu\text{m}$ is

in the ‘eye-safe’ window, permitting the use of increased power in Laser Class 1. The challenge in obtaining high pulse energies is avoiding damage to the absorber. We investigated the damage fluence of the InP-based SESAMs under Q-switched operation. The conclusions are used to improve the SESAM design and to optimize the whole laser. Pulses with 11.2 μJ pulse energy, 0.84 ns pulse duration and peak powers exceeding 10 kW can be achieved at a repetition rate of ≈ 1 kHz.

The second part of this thesis presents a high-power semiconductor laser, mode-locked with high repetition rates. We use an optically pumped vertical-external-cavity surface-emitting laser (VECSEL) to achieve a diffraction-limited beam with high average power. For this device, the key features are a low thermal impedance to meet the power requirements and a smooth gain spectrum for undisturbed mode locking. We have developed a gain element with a thin semiconductor structure on a copper heat sink that fulfills both demands. Design, growth and fabrication of the gain element are discussed and a thermal model for the device is derived. Under mode-locked operation a performance is reached with up to 950 mW average power with 15 ps pulse duration at a repetition rate of 6 GHz. Nearly chirp-free pulses with 4 ps duration are achieved at 530 mW. These are the highest average powers reported from a mode-locked semiconductor laser, making it very attractive for many applications such as commercial printing, improved schemes for data transmission or even laser display systems requiring efficient non-linear frequency conversion.

Kurzfassung

Diese Dissertation behandelt kompakte, gepulste Laserquellen. Zwei Ansätze werden untersucht und führen zu Lasern, die ein großes Spektrum an Eigenschaften abdecken. In beiden Fällen legen wir Wert auf Techniken, die auch für Anwendungen benützt werden können. Deshalb werden Laserdioden als Pumpquellen und sättigbare Halbleiterabsorber (SESAM: semiconductor saturable absorber mirror) zur Pulserzeugung verwendet.

Ein SESAM besteht aus einer Absorberschicht, die in eine Spiegelstruktur eingebettet wird. Bei der Reflexion an einem SESAM erfährt intensitätsschwaches Licht eine definierte Menge an Verlust, während ein Puls mit hoher Intensität besser reflektiert wird. Die Wahl der Halbleitermaterialien erlaubt es, das SESAM an die Wellenlänge des Verstärkungsmaterials anzupassen.

Die drei Elemente, die für einen Laser mit passiver Pulserzeugung benötigt werden, können im einfachsten Fall zu einem quasi-monolitischen Resonator zusammengefügt werden: Auskoppler und SESAM werden von je einer Seite mit dem Verstärkermaterial in direkten Kontakt gebracht. Bei geeigneter Wahl der SESAM- und Kavitäitseigenschaften kann der Laser gütegeschaltet oder modengekoppelt betrieben werden. Hier untersuchen wir Güteschaltung mit einem Mikrochiplaser mit einem Erbium-dotierten Glas als Verstärkermaterial und Modenkopplung mit einer Verstärkerstruktur mit mehreren Quantentöpfen (vorläufig noch mit einer geringfügig komplizierteren Kavität).

Der Ansatz des Mikrochiplasers beschreibt eine sehr kompakte Art, einen Laser aufzubauen ($\approx 1 \text{ mm}^3$ ohne die Pumpoptik) und ermöglicht den Betrieb auf der Grundmode sowohl in transversaler wie auch in longitudinaler Richtung. Güteschaltung führt zu hohen Pulsenergien bei einer niedrigen Repetitionsrate, wie sie für Anwendungen

wie der Messung einer Distanz mittels Reflexionszeit benötigt werden (z. B. dreidimensionales Abbilden oder Geodäsie). Die Wellenlänge um $1.5\ \mu\text{m}$ ist im 'augensicheren' Bereich und erlaubt höhere Leistungen in der Laserklasse 1. Um hohe Pulsenergien zu erzeugen, muss ein möglicher Defekt des Absorbers vermieden werden. Wir untersuchen den kritischen Pulsfluss für die Beschädigung im gütegeschalteten Betrieb des auf InP basierenden SESAMs. Die Ergebnisse werden verwendet, um den Aufbau des SESAMs zu verbessern und um den ganzen Laser zu optimieren. Pulse mit $11.2\ \mu\text{J}$ Pulsenergie, $0.84\ \text{ns}$ Pulsdauer und Spitzenleistungen über $10\ \text{kW}$ wurden bei einer Repetitionsrate von $\approx 1\ \text{kHz}$ realisiert.

Im zweiten Teil dieser Dissertation entwickeln wir einen Hochleistungslaser aus Halbleitermaterialien, der bei einer hohen Repetitionsrate modengekoppelt wird. Wir verwenden einen optisch gepumpten, oberflächenemittierenden Laser mit externem Resonator (VECSEL: vertical-external-cavity surface-emitting laser), um einen beugungsbegrenzten Strahl mit hoher Durchschnittsleistung zu erhalten. Entscheidend für diesen Laser sind ein geringer Wärmewiderstand zur Erzeugung der hohen Leistungen und ein glattes Verstärkungsspektrum für störungsfreie Modenkopplung. Wir haben ein Verstärkerelement mit einer dünnen Halbleiterstruktur auf einem Kühlkörper aus Kupfer entwickelt, das beiden Anforderungen genügt. Aufbau, Wachstum und Fertigstellung des Verstärkerelements werden diskutiert, und ein Wärmemodell für dessen Beschreibung wird hergeleitet. Mit einer Pulsdauer von $15\ \text{ps}$ und einer Repetitionsrate von $6\ \text{GHz}$ können modengekoppelt bis zu $950\ \text{mW}$ Durchschnittsleistung erreicht werden. Bei einer Leistung von $530\ \text{mW}$ können Pulse mit nahezu konstanter Phase und einer Pulsdauer von $4\ \text{ps}$ erzielt werden. Das sind die höchsten Durchschnittsleistungen, die je mit einem modengekoppelten Halbleiterlaser erreicht wurden. Anwendungen wie kommerzielles Drucken, verbesserte Methoden für die Datenkommunikation oder sogar Laserprojektion beruhend auf nicht-linearer Frequenzkonvertierung werden in Zukunft auf diesen Leistungen aufbauen können.

CHAPTER 1

Introduction

Rhythm has conducted life since its genesis. Already the first creatures had to deal with the rhythms of daylight, with the forces of the tides and the temperature differences of the seasons. Even though animals have adapted to the natural timing, it was reserved to mankind to consciously play with new rhythms. The drum has been invented in most indigenous cultures and the development of a reliable calendar is one of the major achievements of ancient peoples. Concerted timing is also a sign for a highly developed system. For example, the synchronized international time zones were established 1884 when the railway network required accurate timing to properly schedule track use and avoid head-on collisions. The technical acquisitions of the last centuries made shorter and shorter time periods significant: While the shortest time a person can react on is 0.1 s^* , a computer already made a hundred million operations!

With lasers one can go even more to the extremes. The shortest time scale accessible by technical means are laser pulses with $\approx 5 \text{ fs}$ duration [1, 2, 3, 4, 5, 6], and the highest repetition rate produced by a laser is 1.54 THz [7]. However, not all applications need high repetition rates. In this thesis, lasers are presented covering a range of 10^7 in terms of repetition rates (from less than a kilohertz to several gigahertz).

Pulsed laser sources can be divided in mainly two classes dependent on their temporal output: Q-switched and mode-locked lasers. (Strictly speaking there are a few more such as Q-switched mode-locked lasers, a combination of the first two; gain switched lasers, a close relative to the Q-switched laser; or quasi-continuous-wave lasers with extremely long pulses.) Characteristic of a Q-switched laser is a pulse duration longer than the cavity round-trip time, while a mode-locked laser has a short pulse circulating in its cavity.

* The shortest time an athlete is expected to react on the starting shot is 0.1 s , while shorter times are considered false start. Neuro-psychological tests use visual stimuli shorter than $100\text{-}150 \text{ ms}$ to evade the tracking motion of the eye.

Pulsed operation can be achieved in both cases using a passive or an active mechanism. We consider here only passive mechanisms, which makes the laser sources simpler, more reliable and generally shorter pulses can be achieved. Passive pulse formation is realized by the use of a saturable absorber, an optical element introducing higher intracavity losses for low intensities and lower losses for high intensities. In this way, pulsed operation with its high intensity for the short pulse period is favored in comparison to continuous operation at a low intensity. Depending on the laser and absorber parameters, Q-switching or mode-locking is obtained.

We are working with semiconductors as saturable absorbers. In semiconductors one has a precise control of the nonlinearities, and the bandgap can be varied over a wide range by the selection of the semiconductor compound. The semiconductor saturable absorber mirror (SESAM, [8, 9]) is a device in which an absorber layer is embedded in a mirror structure all grown with semiconductor materials. The SESAM has been developed in recent years and has allowed to reliably mode-lock and Q-switch a number of different lasers in different wavelength regimes [10]. The application of a SESAM is easy as it simply forms one end mirror of the cavity.

Sources with low repetition rates are often used for applications requiring a long temporal and spatial distance between the pulses. For example, using laser pulses in a time-of-flight configuration for geodesy allows a unique determination of a distance only when the pulses have a larger separation than the maximal range of the instrument. Another aspect of a low repetition rate is the high pulse energy achievable with the same average power. For example, material ablation is more effective with pulsed lasers, but to reach the required pulse energies, repetition rates are typically restricted to a few kilohertz. To achieve low repetition rates for a continuous-wave pumped laser relying solely on passive elements, a gain material with a long upper-state life-time must be selected. Rare-earth doped crystals and glasses are the state of the art with the capability to store energy on an upper laser level for several microseconds [11, 12].

We investigate Q-switching of an erbium doped glass laser with a SESAM. The laser is set up as a microchip laser: a very compact device allowing relatively short pulses (<1 ns) and a single longitudinal laser mode. An erbium transition at a wavelength of $1.5 \mu\text{m}$ is used because liquid water is strongly absorbing in this wavelength range, protecting the retina of the human eye from harmful amounts of irradiation. Consequently, pulse energies of several microjoules at a repetition rate of one kilohertz can be used in the Laser Class 1 (considered safe upon current medical knowledge, DIN EN 60825-1), making such laser sources very attractive for geodesy and other open space applications.

The most widespread application of high repetition rate lasers is telecommunication where the pulse stream is modulated with data. For data transmission a minimal pulse energy at the receiver is required to ensure a low bit error rate. Increasing the transmission distance (thereby raising the losses) and using increasingly high bit rates requires more powerful laser sources. Even though conventional telecommunication systems can be operated with distributed feedback lasers, new schemes for higher bit rates are proposed requiring much more power: the broad spectrum of a short pulse is split and a data stream is impressed on each frequency component independently. Operation of more than a thousand wavelength channels served by a single pulse source are demonstrated [13].

Another application for lasers with high repetition rate and high average power are laser display systems. Projecting images with laser light requires ≈ 1 W per color (red, green and blue) for home cinema and several watts for large screen applications [14, 15]. Semiconductor lasers, which would make home cinema affordable, have not yet reached these power levels in the visible. However, with pulsed laser sources providing enough light at the right wavelength in the infrared, the color can be achieved efficiently with single-pass second-harmonic generation (SHG). A high repetition rate is beneficial because it can be regarded as a continuous wave source for much slower modulations. For example when a picture is scanned pixel by pixel then each point is illuminated for only a fraction of a microsecond and repetition rates in the gigahertz range are required to avoid perturbation of the image by the discrete number of pulses.

A vertical-external-cavity surface-emitting laser (VECSEL) is a semiconductor laser allowing output powers exceeding 1 W in a diffraction limited output beam [16, 17, 18]. We investigate passive mode locking of such a device giving a high power gigahertz source with excellent properties for future commercial applications: it can be miniaturized to a volume of a few cubic centimeters, it is efficient, it can be mass produced in wafer technology, and the flexible design properties of compound semiconductors allow to adapt the performance parameters (e.g. the wavelength can be tuned to enable red, green or blue generation with SHG [19].)

The text is organized as follows: In Chapter 2, the results on the passively Q-switched microchip lasers are presented. Special emphasis is put on the design of SESAMs in such a way that they will withstand the high pulse fluences obtained by such a laser. Measurements of the damage fluence of SESAMs under Q-switching operation are performed, and the results are used to optimize the performance of the laser. The second part of the thesis treats passively mode-locked VECSELs and is split into two Chapters. In Chapter 3, the design, fabrication and characterization of the gain structure is described.

In a part of this chapter we review previously known techniques used to grow and fabricate the gain elements while new considerations are presented in the Sections 3.1 and 3.2, where the design of the layer structure and the thermal properties of the devices are discussed. In Chapter 4, we shortly review the basic principles of mode locking and then present the results obtained with mode-locked VECSELs. In Chapter 5, conclusions are drawn from the presented work and an outlook shows what can be expected in the near future.

CHAPTER 2

Passively Q-switched microchip laser at 1.5 μm

Applications involving free space propagation of short laser pulses can take advantage of much higher peak and average power, when using the wavelength regime around 1.5 μm . In this spectral range the light is strongly absorbed in the water-rich parts of the eye and does not reach the sensitive retina. Applications of such sources include sensing of gases and contamination in air, distance measurements and three-dimensional imaging. Different approaches for adequate laser sources have been reported in recent years. Peak powers > 100 kW and pulse durations < 200 ps have been reported with frequency conversion in an optical parametric generator (OPG) [20, 21]. Gain switching of a Cr⁴⁺:YAG laser pumped with a Q-switched Nd:YAG microchip laser was demonstrated recently [22]. A more direct, simple and efficient approach is passive Q-switching of a 1.5- μm laser with an absorber crystal (e.g. Co²⁺:LaMgAl₁₁O₁₉ [23, 24], Er:Ca₅(PO₄)₃F [25], U⁴⁺:CaF₂ [26, 27], U⁴⁺:SrF₂ [28], Co²⁺:ZnSe [29], Cr²⁺:ZnSe [30]) or with a semiconductor saturable absorber mirror (SESAM) [31]. Laser emission around 1.5 μm has been reported from several gain materials including Cr⁴⁺:YAG (review on Cr⁴⁺-doped garnets [32]), Yb³⁺,Tm³⁺:YLiF₄ [33], Er:Ti:LiNbO₃ [34] and, most commonly used for diode pumped bulk lasers, Er:Yb:glasses (review in Ref. [35]).

SESAMs [8, 9, 10] have been extensively used for passive mode locking and Q-switching of solid-state lasers. Using a SESAM as a passive Q switch has a variety of advantages over other approaches. The flexibility of SESAMs allows to ‘custom tailor’ the parameters needed for a specific application. Design guidelines [36] for Q-switched microchip lasers with SESAMs can be used to vary the operation parameters in large ranges and can be applied to lasers operating in different wavelength regimes, e.g. at $\approx 1 \mu\text{m}$ [37, 38], $\approx 1.3 \mu\text{m}$ [39] and $\approx 1.5 \mu\text{m}$ [31]. SESAMs allow to realize a significantly shorter cavity length (in comparison to doped bulk crystals used as a

saturable absorber) and therefore can generate shorter pulses. Indeed, the shortest Q-switched pulse from a solid-state laser, 37 ps, has been achieved with a Nd:YVO₄ microchip laser using a SESAM [36]. Lasers with low threshold and high efficiency can be designed with SESAMs because the losses can be kept well below 1%. For example, we measured a threshold of 38 mW for a device emitting 0.85- μ J pulses at 1.5 μ m with 7 ns duration.

In previous work for eye-safe microchip lasers [31], peak power and pulse energy were limited by damage of the SESAM. We present here a strategy to obtain higher powers by designing SESAMs with higher damage threshold. After this introduction, in Section 2.1 we describe the setup of passively Q-switched microchip lasers. Section 2.2 summarizes the functional principal of these devices. In Section 2.3 we discuss some general aspects of SESAMs, then the detailed structure for a 1.5- μ m Q-switching element, and at last a method to avoid damage of the absorber. In Section 2.4 measurements of the damage threshold under Q-switched laser operation for InP/InGaAsP SESAMs are presented. Finally, in Section 2.5 we report the performance of an optimized device.

2.1 Microchip laser setup

The setup of a microchip laser and the diagnostics is shown in Figure 1. The cavity of a microchip laser consists of two parallel flat mirrors [40]. To be able to investigate a large variety of different laser parameters, we used discrete components for the output coupler, the gain medium and the SESAM. Platelets of Er:Yb:glass (QX/Er from Kigre, Inc.) with 5 mm x 5 mm cross-section were polished to thickness values of 0.2, 0.3, 0.5, 0.8, and 1 mm, respectively. The erbium doping concentrations are 2.75 wt% of Er₂O₃ for the thinner glasses (0.2 mm to 0.5 mm) and 2.2 wt% for the thicker ones. The ytterbium co-doping is at a level of 21 wt% of Yb₂O₃ for both melts. The polished faces were anti-reflection (AR) coated for both the laser and the pump wavelength. These glass plates were positioned with two molybdenum knives of 100 μ m thickness, touching from the side to allow free access from both faces. The output coupler was approached to the front face while the SESAM was used from the other side to close the cavity. Air gaps of a few microns were left between the three components in order to allow for fine adjustment of the cavity. Compared with similar setups using other gain media such as Nd:YVO₄ or Nd:YAG, we found that the alignment of the output coupler and SESAM is much more delicate for Er:Yb:glass lasers. The reason for this is the negative dn/dT of the

phosphate glass which has a destabilizing effect on the cavity mode. This effect competes with the stabilizing effects of thermal bulging of the end faces and gain guiding [41, 42]. Small wedge angles in the order of a milliradian between output coupler and SESAM lead to a significant increase of the threshold and can affect the pulse shape. (This might lead to multiple pulses but can also significantly reduce the pulse duration [43].)

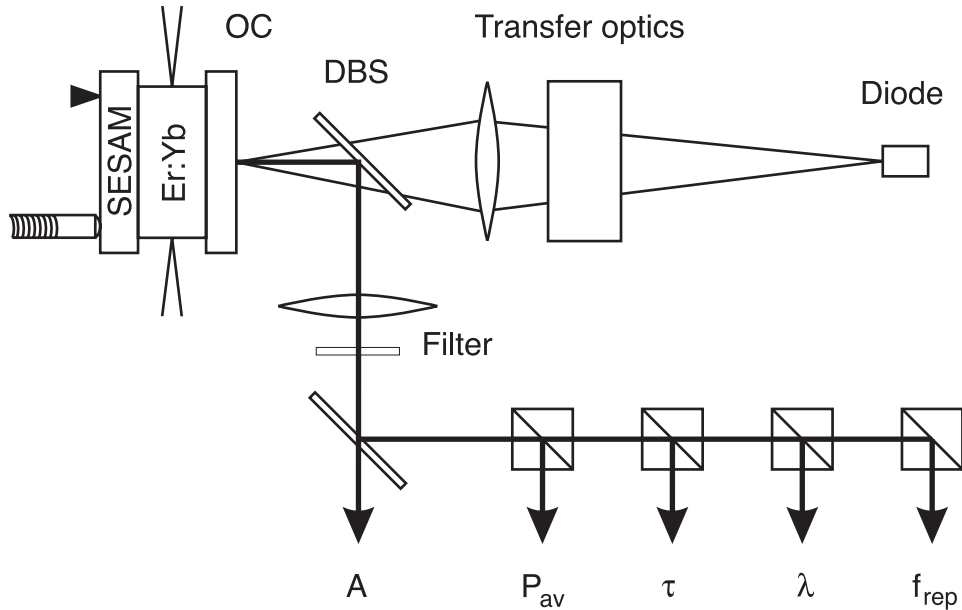


Figure 1. Scheme of the laser and diagnostic setup. A polished and AR-coated Er:Yb:glass plate is held from the side with two knife edges. Output coupler (OC) and SESAM are aligned to be parallel within an angle < 0.1 mrad. We used up to 1 W pump power from a 100- μm strip width diode. The output is separated from the pump light with a dichroic beamsplitter (DBS). The output is divided with beamsplitters to monitor several parameters simultaneously: A = laser mode area imaged with a vidicon tube camera; P_{av} = Average power; τ = Pulse duration measured with a 45-GHz detector and a 50-GHz sampling head; λ = optical spectrum, and f_{rep} = repetition rate monitored with a digital oscilloscope.

The laser is pumped with a 100- μm strip width laser diode (Nortel Networks, Zürich). The diode can produce up to 3 W of pump power at 975 nm. However, we could apply only up to ≈ 1 W of pump power because we observed cracking of the glass for higher powers. We pumped the laser through a dichroic beamsplitter and the output coupler.

The diagnostics were set up to monitor all the important parameters simultaneously. With a vidicon tube camera we monitored the laser mode area and the transverse mode quality.

We define the mode area as $\pi w^2/2$ (with w being the gaussian mode radius) so that the peak intensity (on the symmetry axis) is simply the power divided by the mode area. The repetition rate was determined with a 500-MHz digital oscilloscope. To measure the pulse shape and the pulse width we used a 45-GHz photodetector and a 50-GHz sampling head. The optical spectrum was monitored with an optical spectrum analyzer with a resolution of 0.1 nm, and the average output power was measured with a thermal powermeter.

2.2 Operation parameters of Q-switched microchip lasers

The dependence of the laser output on the design parameters has been described theoretically and confirmed experimentally by Spühler et al. [36]. The model is based on a few assumptions which are usually well fulfilled for Q-switched microchip lasers: *i*) small gain and loss during one cavity round trip (a few percent) were assumed, *ii*) spatial hole burning was neglected, *iii*) no transverse intensity variations within the area of the laser mode A_L were considered, and *iv*) the total non-saturable losses (transmittance of the output coupler T_{OC} and parasitic losses l_{par}) are assumed to be larger than the modulation depth ΔR , which is favorable for both the slope efficiency and a symmetric pulse shape with short duration. The modulation depth ΔR is defined as the amount of losses of the saturable absorber that can be bleached with high intensities. Here we summarize the most important results.

The **pulse energy** E_p can be written as

$$E_p = 2 A_L F_L \Delta R \frac{T_{OC}}{T_{OC} + l_{par}} . \quad (1)$$

$F_L = (h\nu_L)/(2\sigma_L + 2\sigma_L^{abs})$ is the saturation fluence of the gain material with ν_L the laser frequency and σ_L and σ_L^{abs} the cross-section for stimulated emission and re-absorption at the laser wavelength, respectively. The fraction $T_{OC}/(T_{OC} + l_{par})$ accounts for the output coupling efficiency.

To obtain a high pulse energy, one can enlarge the mode area, but a good beam quality can not be obtained for too large modes. Choosing a gain material with a small gain cross-

section leads to a high saturation fluence and thus to a high pulse energy. Finally, the modulation depth of the SESAM can be increased, as is discussed in the Section 2.3.

The **pulse duration** is given by

$$\tau_p = \frac{7nL}{c\Delta R}, \quad (2)$$

[44] where n is the index of refraction of the gain material, L is the cavity length, and c the speed of light. The cavity round trip time is $2nL/c$.

A reduction of the pulse duration can be achieved by shortening of the cavity or by using a SESAM with larger modulation depth. Both measures, however, are limited by the requirement that sufficient gain must be generated to overcome the laser threshold.

The **repetition rate** is calculated as the average power divided by the pulse energy. As the pulse parameters are only weakly dependent on the pump power as long as the mode area is not significantly changed, an increase of pump power simply increases the repetition rate.

Er:glass has a high saturation fluence and we can achieve μJ -pulses already with a modulation depth below 1%. These pulse energies can lead to SESAM damage. To some extent, this can be avoided by using improved SESAM designs as discussed in the next section.

2.3 Semiconductor saturable absorber mirror (SESAM)

2.3.1 Parameters of a SESAM

Figure 2 shows the reflectivity of a SESAM as a function of the incident pulse fluence. The modulation depth ΔR is defined as the maximum reflectivity change between low and high intensity. The remaining losses at high intensity we call non-saturable losses, and the fluence needed to switch 1/e of the saturable losses is the saturation fluence F_{sat} .

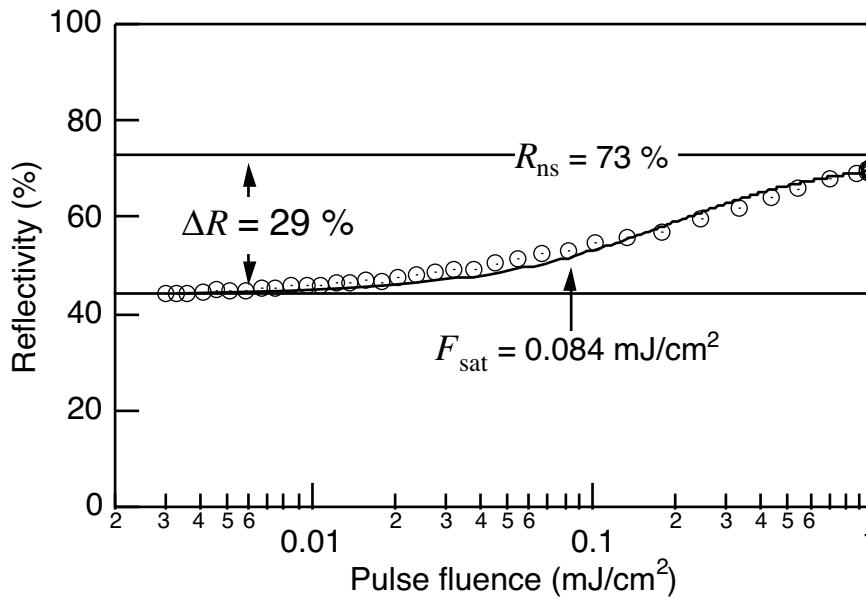


Figure 2. Reflectivity of a SESAM as function of the incident pulse fluence. The data was measured with 100-fs pulses from an optical parametric oscillator (OPO) system. The SESAM is an AR coated reference sample from the same growth run as SESAM No 8 and 9 in Table 1.

The dynamic response of the absorber plays a minor role for Q-switching as long as the recovery time τ_A of the absorber is larger than the pulse duration τ_p and smaller than the pulse-to-pulse duration $1/f_{\text{rep}}$. Having a recovery time shorter than the pulse duration reduces the efficiency of the laser, but does not help to decrease the pulse duration. Therefore, we typically use SESAMs with recovery times of several nanoseconds for Q-switched microchip lasers.

2.3.2 Top reflector

The SESAM design best suited for Q-switching with high pulse energies is the high-finesse anti-resonant Fabry-Perot saturable absorber [8, 9]. Here the semiconductor absorber is embedded in an anti-resonant cavity between a semiconductor bottom Bragg mirror of high reflectivity and a sputtered dielectric top reflector with a transmittance T_t (Figure 3).

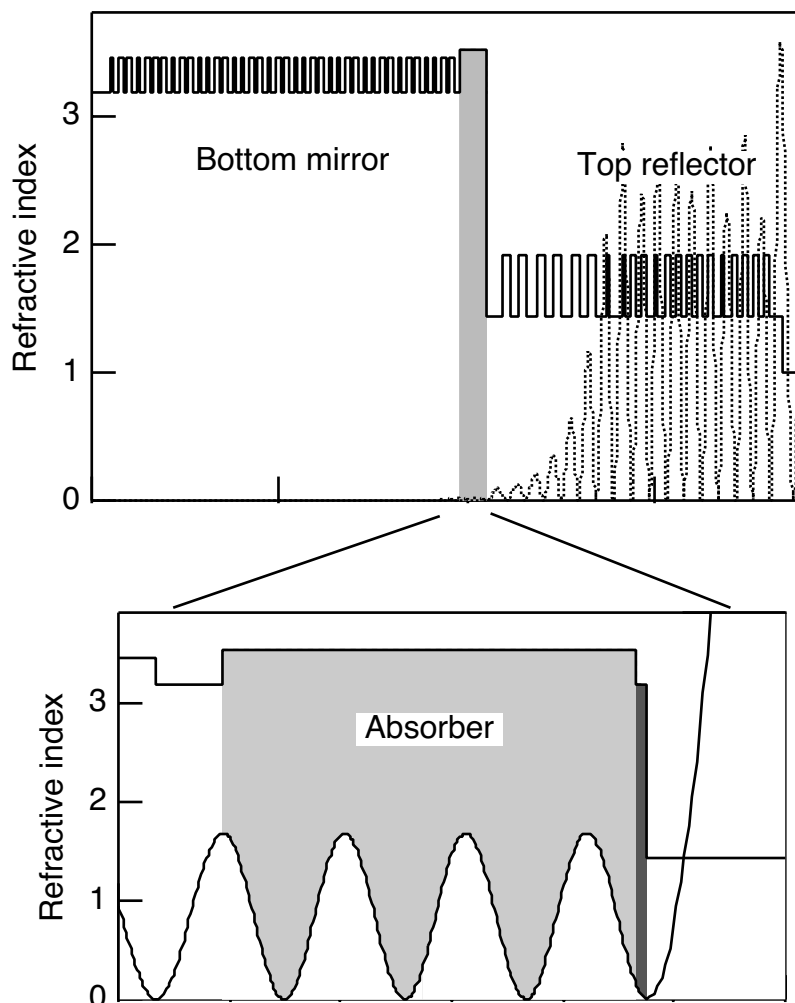


Figure 3. Refractive index profile and standing wave pattern of SESAM No 8 in Table 1. In the upper plot the bottom mirror and top reflector are well visible. The lower graph is a close up of the absorber region. The thickness of the absorber is adjusted so that the two mirrors are in anti-resonance. The last semiconductor layer is a 21 nm thick InP cap layer to prevent surface recombination of the carriers.

An advantage of using a combined structure with semiconductor and dielectric materials is the possibility of characterizing the semiconductor structure before the top reflector is produced. Usually we cleave several samples of the same growth run and apply different dielectric coatings as a top reflector, where at least one sample has an AR coating for a high modulation depth which facilitates precise characterization. We call the modulation depth of the AR coated sample ΔR_{AR} and the non-saturable losses $l_{ns,AR}$ (or we specify the reflectivity in the saturated state $R_{ns,AR} = 1 - l_{ns,AR}$).

With the transmittance of the top reflector T_t we can adjust the intensity allowed to enter the absorber. Decreasing the transmittance T_t reduces the intensity on the absorber and thus increases the damage fluence and reduces the non-saturable losses, but also decreases the modulation depth and increases the saturation fluence. The fluence on the absorber F_{abs} can be calculated as

$$F_{\text{abs}} = \xi F_{\text{AR}} \quad (3)$$

[45] where F_{AR} is the fluence in the AR-coated reference sample. For low fluences and in anti-resonance the ξ -factor can be written as

$$\xi_{\text{low}} = \frac{T_t}{\left(1 + \sqrt{(1 - T_t) (R_{\text{ns,AR}} - \Delta R_{\text{AR}})}\right)^2}. \quad (4)$$

In saturated condition, ξ is

$$\xi_{\text{high}} = \frac{T_t}{\left(1 + \sqrt{(1 - T_t) R_{\text{ns,AR}}}\right)^2}. \quad (5)$$

For small non-saturable losses $l_{\text{ns,AR}} \ll 1$ ($R_{\text{ns,AR}} \approx 1$) the modulation depth is scaling with the same factor as the fluence for low intensities:

$$\Delta R \approx \xi_{\text{low}} \Delta R_{\text{AR}} \quad (6)$$

where ΔR is the modulation depth of the sample with the top reflector.

2.3.3 SESAMs for 1.5 μm Q-switching experiments

The Bragg mirror and the absorber were grown with metal-organic chemical vapor deposition (MOCVD) on an InP substrate. The materials used for the mirror as well as for the absorber were lattice matched to InP. For the bottom mirror, we used 40 pairs of InP/In_{0.65}Ga_{0.35}As_{0.73}P_{0.27} quarter-wave layers. The absorber was grown with In_{0.58}Ga_{0.42}As_{0.9}P_{0.1} and covered with a cap layer of InP. The cap layer is used to prevent carrier trapping and recombination at the semiconductor surface [31]. All absorbers were measured with a pump probe experiment to have a recovery time > 5 ns. For the top reflector we use a SiO₂/HfO₂ coating with a high reflectivity for the pump wavelength and a designed transmittance for the laser wavelength (Table 1).

Table 1. SESAM parameters. d_{abs} is the absorber thickness, and T_t is the transmittance of the top reflector. ΔR_{AR} is the modulation depth and $l_{\text{ns,AR}} = 1 - R_{\text{ns,AR}}$ are the non-saturable losses of the AR coated reference sample, respectively. ΔR is the modulation depth of the SESAM.

SESAM No	d_{abs} nm	T_t %	ΔR_{AR} %	$l_{\text{ns,AR}}$ %	ΔR %
1	40	8	5.7	1.2	0.12
2	40	12	5.7	1.2	0.19
3	40	29	5.7	1.2	0.50
4	90	8	7.4	5.4	0.17
5	90	12	7.4	5.4	0.25
6	310	8	15	16	0.37
7	310	12	15	16	0.57
8	740	8	29	27	0.87
9	740	12	29	27	1.32
optimized	2500	5	35	60	1.17

2.3.4 Optimization of top reflector

Let us compare two SESAMs, which have different transmittance T_t of the top reflector but with the same modulation depth of the final structure. That means the SESAM with the higher top mirror reflectivity has a thicker absorber. As long as both SESAMs still can be fully saturated, the resulting laser performance will be the same. However, the lower transmittance T_t reduces the pulse fluence on the absorber and thus increases the damage threshold.

We calculate the top reflector needed to prevent the SESAM from damage. The damage fluence F_d of the absorber is assumed to be known. Measurements for 1.5- μm absorber material will be presented in the Section 2.4. Equation (3) can be used to calculate the fluence on the absorber

$$F_{\text{abs}} = \frac{\xi_{\text{high}}}{T_{\text{OC}}} F_p, \quad (7)$$

where $F_p = E_p / A_L$ is the pulse fluence outside the cavity. The transmittance of the output coupler T_{OC} accounts for the fact that the SESAM is exposed to the intracavity intensity.

Using the pulse fluence described in Equation (1) and replacing the modulation depth with the approximation of (6), we obtain in a fluence on the absorber layer of

$$F_{\text{abs}} = 2F_L \Delta R_{\text{AR}} \frac{1}{(T_{\text{OC}} + l_{\text{par}})} \frac{T_t^2}{\left(1 + \sqrt{(1 - T_t) R_{\text{ns,AR}}}\right)^2 \left(1 + \sqrt{(1 - T_t)(R_{\text{ns,AR}} - \Delta R_{\text{AR}})}\right)^2}. \quad (8)$$

To avoid damage we should keep the fluence on the absorber below the damage fluence:

$$F_{\text{abs}} < F_d.$$

For a rough estimate one can neglect the parasitic losses l_{par} (which should be small compared with the transmittance of the output coupler) and replace the parenthesis in the second denominator with an intermediate value of 2. We obtain a condition for the transmittance of the top reflector to prevent the SESAM from damage:

$$T_t < \sqrt{2} \frac{F_d T_{\text{OC}}}{F_L \Delta R_{\text{AR}}}. \quad (9)$$

In Figure 4, the quality of the approximation made in equation (6) and the estimate of equation (9) are compared with a numerical simulation. The fluence on the absorber F_{abs} divided by the saturation fluence F_L is plotted versus the transmittance of the top reflector. The parameters used for the plot are non-saturable losses of $l_{\text{ns}} = 20\%$, modulation depth of the AR coated sample of $\Delta R_{\text{AR}} = 40\%$, transmittance of the output coupler of $T_{\text{OC}} = 10\%$, and parasitic losses of $l_{\text{par}} = 1\%$.

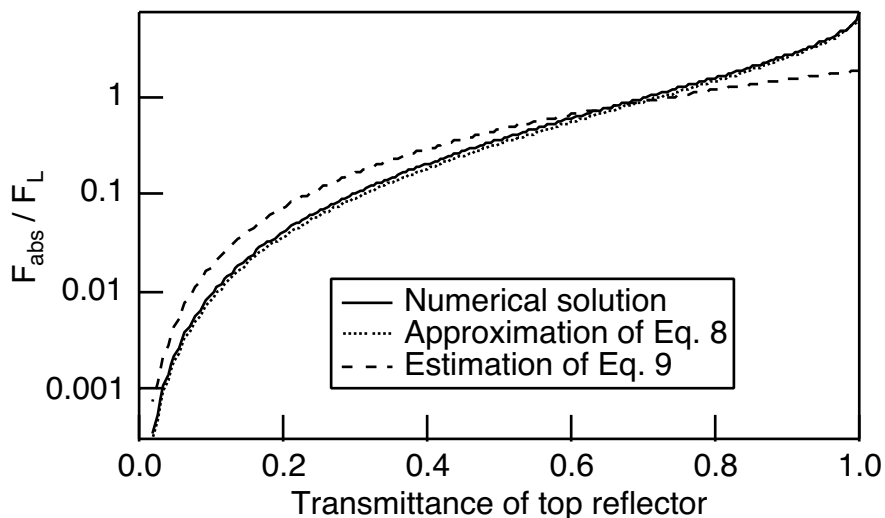


Figure 4. Pulse fluence on the absorber divided by the saturation fluence of the gain medium plotted versus the transmittance of the top reflector. The parameters used are non-saturable losses of $l_{ns} = 20\%$, modulation depth of the AR-coated sample $\Delta R_{AR} = 40\%$, transmittance of the output coupler $T_{OC} = 10\%$ and intracavity losses of $l_{par} = 1\%$. The solid line is a numerical simulation, the dotted line represents equation (8) (neglecting the non-saturable losses for the scaling of the modulation depth) and the dashed line is the solution for a rough estimate given in equation (9).

The strategy to achieve high modulation depth and avoid damage for a Q-switched microchip laser can be summarized as follows: First we grow the semiconductor part of the SESAM with as much modulation depth as we can get. This can be limited by the critical thickness for strained layers, or for lattice matched growth, the non-saturable losses will eventually reduce the modulation depth with further increase of the absorber thickness. The appropriate transmittance for the top reflector can be determined using equation 8.

2.4 Damage measurements

With this experiment, we determined the damage fluence of several absorbers when operated in the Q-switched laser and showed that damage is mainly caused by excessive pulse fluence on the absorber layer, not in the dielectric top mirror. This we concluded from a large set of damage data taken with different SESAM and laser parameters. We

combined the SESAMs listed in Table 1 with output couplers with transmittances of 0.43%, 6.0% and 11.3%. The gain medium was varied with the above mentioned glasses of 0.2 mm to 1 mm thickness. For the pump spot we used two settings, either diameters of $\approx 100 \mu\text{m} \times 105 \mu\text{m}$ or $\approx 180 \mu\text{m} \times 160 \mu\text{m}$. For each set, data was taken at pump powers near threshold, at an intermediate value, and at full pump power ($\approx 1 \text{ W}$ limited by glass fracture).

Out of 167 combinations investigated, 29 could not reach threshold or immediate damage of the SESAM was observed. For the rest we found stable Q-switched operation. However in this group, we could distinguish two classes: completely damage-free setups and lasers where we found a dependence on transverse position. (Probably damage occurs faster at spots where already some defects are present in the absorber layer.) 35 combinations are in this marginal class. Note that in the marginal cases an early damage mechanism can considerably increase the losses of the structure without completely destroying it. This results in a slow drop of the output power (seconds to minutes) and reduced pulse energy while the pulse duration is unchanged. It leads to a tendency that the pulse fluence is measured too low for these marginal cases because the intracavity losses have already increased during data acquisition.

From the measured pulse energy, laser spot size and reflectivities of the output coupler and top reflector of the SESAM we calculated the fluence on the absorber layer. Figure 5 a) shows this fluence versus average power. The solid circles indicate lasers without any sign of damage, while the open circles are the marginal cases. As a guide to the eye, we plotted an approximate upper ($F_d = 100 \text{ mJ/cm}^2$) and a lower boundary ($F_d = 10 \text{ mJ/cm}^2$) for the damage fluence. We see that the occurrence of damage does not depend on the average output power. Apparently the peak fluence of a single pulse, which is nearly independent of the average output power, is the critical quantity, and not the pulse repetition rate. In Figure 5 b) the pulse fluence is plotted versus the pulse width, indicating that damage occurs independent of pulse width. Figure 5 c) shows the fluence for the different SESAM samples. (The SESAM numbers correspond to Table 1.) It is surprising that even different SESAMs based on the same absorber structures (i.e., with only the top mirror varied) show damage at different fluence values. We believe that this is due to errors in the calculation of the pulse fluence on the absorber. Thickness variations particularly of the thicker absorbers lead to deviations from the anti-resonance condition, so that the actual fluence on the absorber can be higher than calculated assuming anti-resonance.

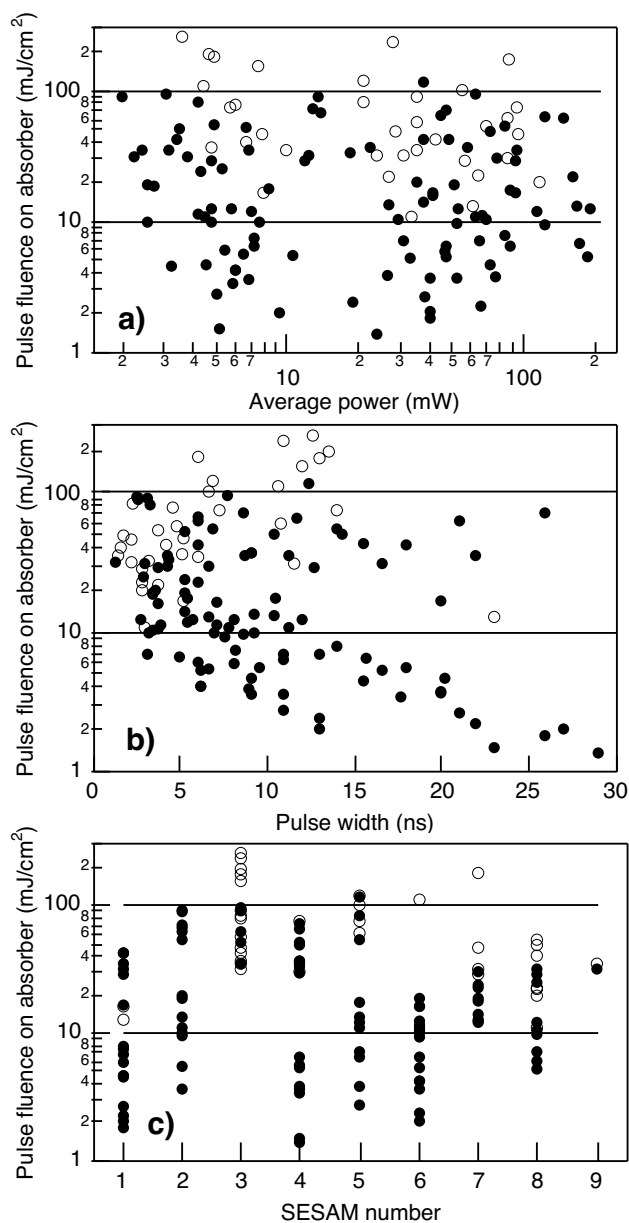


Figure 5. Results of damage measurements under operating conditions. Each point corresponds to a result from a specific laser. In all graphs, the pulse fluence on the absorber, calculated assuming anti-resonance of the SESAM, belongs to the vertical axis. The solid circles indicate experiments where no damage was observed, while open circles represent experiments where damage was observed only for certain spots on the absorber. The solid lines are a guide to the eye and indicate an upper and a lower limit for the safe parameter range.

a) Pulse fluence versus average power. b) Pulse fluence versus pulse duration. c) Pulse fluence versus SESAM number.

To verify that damage occurs in the semiconductor material and not in the top reflector, we used a surface profiler (alpha-step) to investigate the damaged spots. Two kinds of profiles could be distinguished: crater-like and hill-like features. However, removing the coating by selective etching, the absorber below shows similar structure for both kinds with a hole indicating that the initial damage occurs in the absorbing layer. Note that laser-induced damage in transparent dielectric materials has been investigated extensively elsewhere [46], but damage of semiconductor absorbers is a physically quite different phenomenon.

With this experiment we could show that damage typically occurs at a pulse fluence on the absorber above $\approx 10 - 100 \text{ mJ/cm}^2$.

2.5 Optimized SESAM and laser performance

Following the strategy discussed in section 4 for optimizing the SESAM performance lead us to the following design: on a Bragg mirror with 40 pairs of InP/InGaAsP quarter-wave layers an absorber was grown with $2.5 \mu\text{m}$ thickness resulting in a double pass absorption of $\approx 95\%$. For the top reflector we used $T_t = 5\%$, resulting in a modulation depth of 1.2% . An even thicker absorber of $4.5 \mu\text{m}$ has been investigated with the same top reflector. However, the sample shows large non-saturable losses, while the modulation depth could not be increased further.

The laser was set up with a 4% output coupler and a 0.5 mm thick glass doped with 2.75 wt\% erbium and 21 wt\% ytterbium oxide. The pump spot was $170 \mu\text{m} \times 190 \mu\text{m}$. In Figure 6, a sampling scope trace of the pulse is shown. The pulse has a full width at half maximum duration of 0.84 ns , a peak power of 10.6 kW and a pulse energy of $11.2 \mu\text{J}$. Figure 7 shows the optical spectrum of this pulse. With a pump power of 608 mW resulting in an output of 16 mW and a repetition rate of 1.4 kHz , nearly single-mode operation is achieved with a side mode suppression of 15 dB . Up to 51 mW average power could be obtained and were limited by glass fracture. However above 16 mW of average power the laser could no longer be operated with a single longitudinal mode.

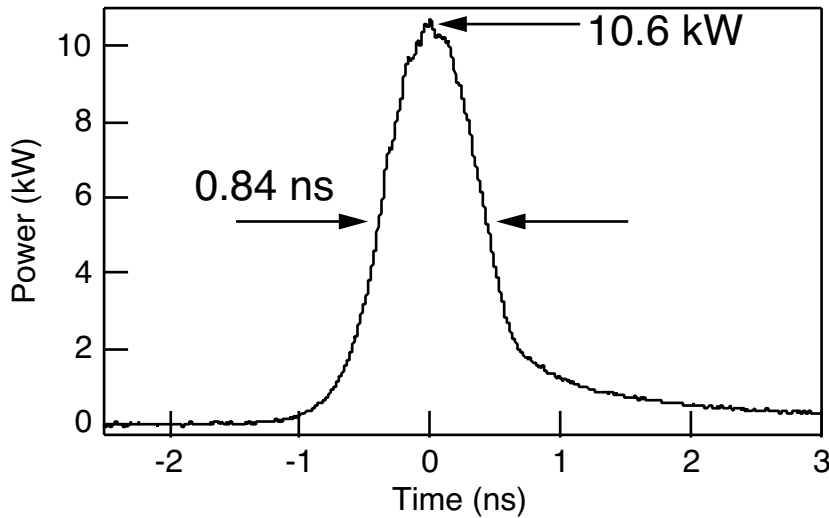


Figure 6. Sampling scope trace of the Q-switched output pulse measured with a 45-GHz photodetector and a 50-GHz sampling head. The repetition rate was 1.4 kHz and the pulse energy 11.2 μ J resulting in an average power of 16 mW.

For all setups we observed a dependence of the pulse-to-pulse jitter on the mode number. When the laser operates on a single longitudinal mode, the repetition rate has typically fluctuations below 2% (standard deviation). For operation on two longitudinal modes, the timing fluctuations become much stronger, typically around 10%, but sometimes even 30% and more. Here we often observe a hopping between two different pulse separations, either regularly or sometimes in a chaotic manner. This can be explained by spatial hole burning: When the laser reaches threshold, the longitudinal mode closest to the gain peak starts oscillating. After evolution of this first pulse the remaining inversion is spatially modulated. Another longitudinal mode may reach threshold earlier, when it has a better overlap with the undepleted inversion. With several modes (> 5) the jitter is weaker than with only two modes, but the variations typically remain much larger than in the single-mode case.

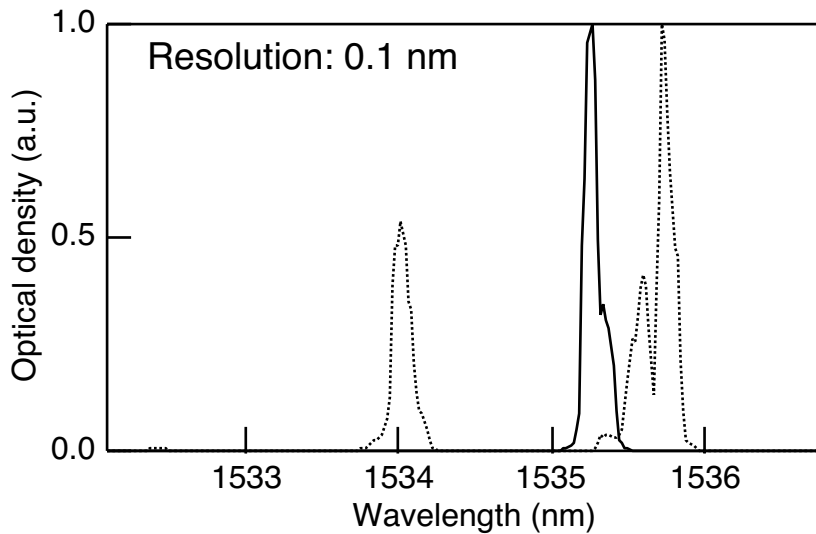


Figure 7. Optical spectrum of the laser corresponding to the pulses shown in Figure 6. The solid line shows a single longitudinal mode for 16 mW average power, while multi-longitudinal mode operation is observed at higher powers (dotted line, 45 mW). The shoulders of the peaks (particularly the single mode peak) indicate the presence of some higher order transverse modes.

We measured a laser spot diameter of $150\ \mu\text{m} \times 115\ \mu\text{m}$ in the laser. With this large mode the laser was no longer diffraction limited. We measured M^2 values of 2.0 and 2.7 parallel to the fast and slow axis of the pump diode, respectively. With pump spots of about $100\ \mu\text{m}$ diameter we get close to the diffraction limit with $M^2 < 1.3$. For the $11.2\text{-}\mu\text{J}$ pulses the fluence on the absorber is $130\ \text{mJ}/\text{cm}^2$. That is in the marginal regime and indeed we also found spots where the SESAM was damaged. However, once the laser is running we did not see any sign of degradation during the experiment which lasted for several hours.

Since there is no polarization dependent element in the cavity, one would expect an unpolarized beam. However, with some ellipticity of the pump beam, e.g. with the pump spot diameter in one direction being 30% smaller than in the other direction, enough strain is generated to stabilize a linear polarization state. For nearly circular pump beams, hopping between two linear polarization states can occur.

In conclusion, we have shown that the damage of InP/InGaAsP semiconductor saturable absorber mirrors (SESAMs) used for eye-safe passively Q-switched microchip lasers at $1.5\ \mu\text{m}$ is basically determined by a critical fluence in the order of $10 - 100\ \text{mJ}/\text{cm}^2$ for a single pulse within the absorber layer. We can obtain significantly higher pulse energies

of up to $11.2 \mu\text{J}$ from such microchip lasers by using antiresonant SESAM designs with relatively high top mirror reflectivity and a thick absorber layer, so that the fluence within the absorber layer is much smaller than the fluence incident on the SESAM. Pulses with sub-nanosecond duration and peak powers up to 10.6 kW have been obtained and make these lasers interesting for applications like range finding and three-dimensional imaging.

CHAPTER 3

Gain Structures for Vertical-External-Cavity Surface-Emitting Lasers

Laser sources with high power and good beam quality are the goal of many research projects. Various processes and applications depend on these two quantities either in terms of efficiency or they are not even possible at low intensities: for example non-linear frequency generation is more efficient with higher power, telecommunication can reach longer distances with more pulse energy and material processing is faster with a brighter beam. Using pulsed sources allows to benefit from much higher peak power making non-linear processes even more efficient but it also permits the use of short pulse duration for example for data transmission.

Recently a new type of semiconductor laser was invented which proved to generate both high average powers (> 1 W) and circular diffraction-limited output beams: An optically pumped vertical-external-cavity surface emitting lasers (VECSELs, Figure 8) [16, 17, 18]. A diode laser (with low beam quality) is used to pump the laser optically. One end mirror is integrated in the semiconductor gain structure while a curved mirror can enforce a diffraction limited output beam.

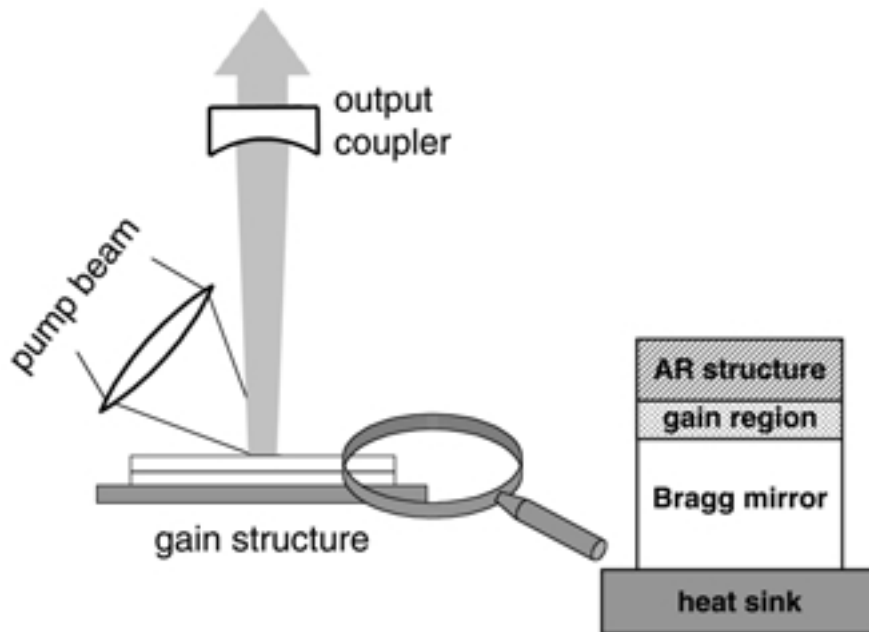


Figure 8. Setup of an optically pumped vertical-external-cavity surface-emitting laser (VECSEL). The inset shows the generic design of the gain structure for a mode-locked VECSEL.

The VECSEL approach is favorable compared with more conventional semiconductor lasers. In edge-emitting semiconductor lasers the intensity at the facet limits the achievable power due to optical damage. For high power performance the facet and thereby the cross-section of the waveguide has to be increased. In conventional ridge waveguides this leads to lasing on multiple transverse modes for ridges more than a few microns wide. Techniques to increase average power while maintaining a single lateral mode include flared waveguides [47], compound lasers with a tapered semiconductor amplifier section [48] and master-oscillator-power-amplifier systems with tapered [49] and inverse bow-tie amplifier geometry [50]. The problem of high intensities at the air-semiconductor interface is solved with a surface emitting device, where power scaling is done by increasing the active spot size while leaving the intensities constant. However, in monolithic vertical-cavity surface-emitting lasers the stability of the cavity is coupled with gain and heating properties in the active region and allows fundamental transverse mode operation only to device diameters of $<10 \mu\text{m}$, limiting the output power $<10 \text{ mW}$ [51, 52, 53]. An external cavity allows to match the cavity mode size to the device size and enables operation of the fundamental mode even with active spot sizes of several hundred micrometers. The remaining challenge for high power operation on the fundamental transverse mode is a smooth and homogeneous inversion over the laser mode area. High power performance with a ring electrode has been demonstrated by using the substrate as

an electron spreader [54]. But for mode-locking a beam path through the substrate would disturb pulse formation. Optical pumping with a laser diode is chosen instead.

To demonstrate and investigate mode locking of a VECSEL we choose to use GaAs based materials with InGaAs quantum wells designed to lase at 950 nm. Growth on GaAs wafers is used because the small lattice misfit of AlAs allows the growth of high quality mirror structures. A wavelength around 950 nm is used because suitable pump diodes at 805 nm are readily available and the strain in the InGaAs quantum well is still moderate enough to allow growth with a low defect rate but high enough to improve the gain [55, 56, 57, 58, 59]. However, semiconductor materials give a large design freedom and other wavelengths can be achieved with the same approach but different material compositions.

This chapter not only describes all steps needed to design and fabricate a gain structure for a VECSEL but also discusses techniques needed for growth and characterization. In Section 3.1 the design of the semiconductor structure is explained. The thermal properties are discussed in Section 3.2. Growth by metalorganic chemical vapor deposition (MOCVD), including the calibration of the growth rates, is treated in Section 3.3. To fabricate a structure with low thermal impedance we grow the gain structure in reverse order with intermediate etch-stop layers. Then a dice is soldered to a heat sink and the substrate is removed by selective etching, resulting in an epitaxial lift-off (ELO) device as described in Section 3.4. Characterization of the gain structure is the topic of Section 3.5.

3.1 Design of the structure

The gain structure has to fulfill several functions. It must include a highly reflective mirror for the laser wavelength, the pump light must be absorbed efficiently in the right place, it should provide a large and smooth gain spectrum, and a large saturation fluence is favorable for the pulse formation (see Section 4.1). Additionally, the thermal impedance must be low for high power performance. In the inset of Figure 8 a schematic of the generic gain structure is shown.

The demands are partly conflicting and compromises have to be taken. For example a large gain can be provided when the ‘anti-reflective’ structure is replaced with a partially reflecting mirror and the active area is placed in resonance, but then the form of the gain spectrum is defined by the narrow resonance and the saturation fluence is diminished by

the increased intensity in the active area due to the resonance. We therefore use an anti-reflective structure both for the laser and the pump wavelength.

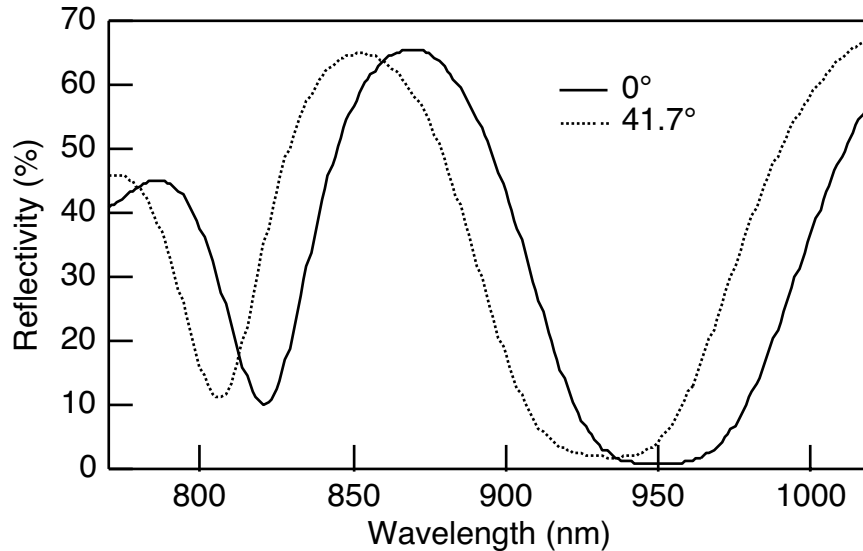


Figure 9. Reflectivity spectrum of the anti-reflective structure under normal incidence (solid) and under 41.7° angle of incidence for the unpolarized pump light (dotted).

In Figure 9 the reflectivity is shown for an anti-reflective structure design for laser emission at 950 nm pumped under an angle of 41.7° with an unpolarized 805 nm beam. A 10 nm GaAs cap layer is used to prevent oxidation of AlGaAs layers. Additionally, we use $\text{Al}_{0.2}\text{Ga}_{0.8}\text{As}$ for the last thick layer instead of AlAs to reduce the oxidation effect if the cap layer should experience minor damage. An $\text{In}_{0.485}\text{Ga}_{0.515}\text{P}$ layer could be considered as replacement because it is lattice matched to GaAs, has a low refractive index, does not absorb the pump light and is stable against oxidation. The residual reflectivities are 0.8% near the laser wavelength and 11% for the pump light with this 15-layer design. The improved transmission that can be achieved with thicker designs is typically counterbalanced when considering an error of the growth rate in the range of 1-3%.

The active area consists of a thick pump absorbing layer and quantum wells (QWs) placed in the antinodes of the standing wave pattern. Absorption in the spacer layers between the QWs allows for an efficient absorption. The generated carriers are then trapped in the QWs to provide the gain. The thickness of the active area is designed for resonance with the residual reflectivity of the anti-reflective structure for both laser and pump wavelength.

For more efficient pump absorption as well as to reduce heating, the mirror has a high reflectivity not only for the laser but also for the pump light. For example a design with reflectivities of 99.95% at 950 nm and 97% at 805 nm under a 45° angle of incidence can be achieved with 62 layer and was used for our last device.

An important issue in the design is its producibility. We have to consider a variations in the growth rate of about 1-3% for the metalorganic chemical vapor deposition (MOCVD) system we are using. The critical features of the design which are most sensitive to such variations are the residual reflectivity of the anti-reflective structure, the narrow stop band of the mirror for the pump laser and the resonances for pump and laser. Small errors in the absorption characteristics near the pump wavelength can be compensated for with a slight variation of the angle of incidence of the pump light. In fact we optimize the pump absorption by selection of the angle before setting up the cavity.

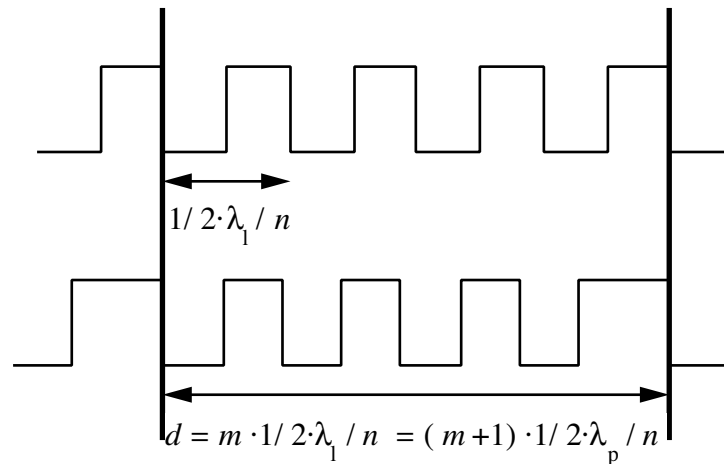


Figure 10. Double periodic Bragg grating. A periodic modification over $2 \cdot m$ layers can improve the $(m+1)^{\text{st}}$ order reflection drastically. Increasing the thickness of the $2 \cdot m^{\text{th}}$ layer and reducing the thickness of the other layers correspondingly proves to give a good modification.

For the mirror structure we found the most tolerant designs when the optical thickness of all layers is close to $\lambda/4$. With numerical optimization starting from a Bragg mirror or by random optimization we usually have some very thick or very thin layers in the design. To avoid this we start from an improved analytical design: The idea is to take the Bragg mirror for the laser wavelength and to increase a higher order reflection for the pump wavelength. In Figure 10 a suitable modification is illustrated. Consider the case, when the pump light

is reflected in phase with the reflection at the surface after m periods of the Bragg mirror. That means we obtain m periods of the standing wave pattern at the laser wavelength and $m + 1$ periods at the pump wavelength. This $(m + 1)^{\text{st}}$ order Bragg reflection of the pump wavelength can be greatly increased if every $2 \cdot m^{\text{th}}$ layer is enlarged and the other layers are adjusted that the package of $2 \cdot m$ layers keeps the thickness. (It also works when $2 \cdot m$ is an odd number. Then the enlarged layers are alternately made of high and low index material).

In Figure 11 the reflectivity spectrum of such a design is shown. The center wavelength of the original Bragg mirror is 1100 nm (solid line). The fifth order Bragg reflection occurs at 902 nm (when the dispersion of GaAs and AlAs is considered). That means we have an improved reflectivity at 902 nm when every 8th layer is enlarged. Plots are given for thicknesses of 1.21, 1.49 and 1.98 quarter wave optical thickness (QWOT) of the enlarged layer.

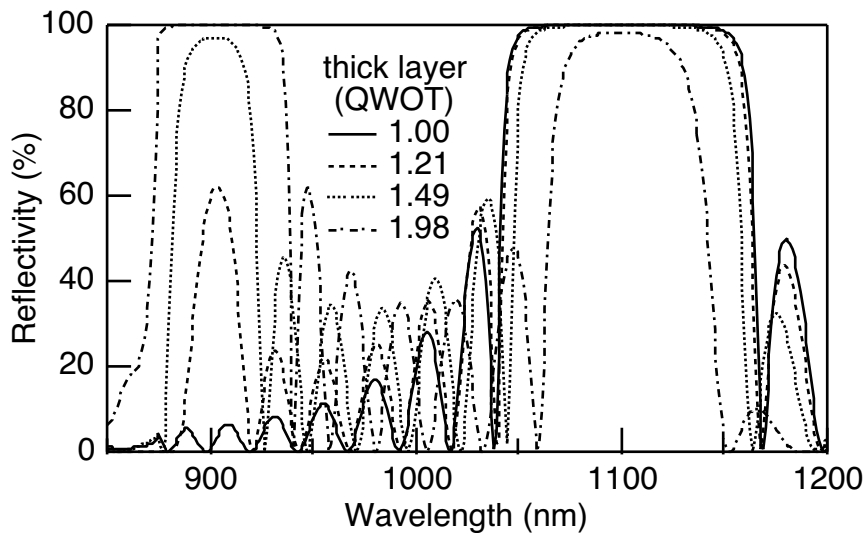


Figure 11. Reflectivity of double periodically modified Bragg reflector. The fifth order reflection of the Bragg grating can be strongly improved with a modification periodic over 8 layers.

The periodicity of the modification can be found when writing the Bragg condition for both the laser wavelength λ_1 and the pump wavelength λ_p and with effective refractive indices \tilde{n}_1 and \tilde{n}_p for laser and pump, respectively.

$$m \frac{\lambda_1}{2\tilde{n}_1} = d = (m + k) \frac{\lambda_p}{2\tilde{n}_p} \quad (10)$$

where $k \in \mathbb{Z}$ generally, but $k=1$ for most practical cases where pump and laser wavelength are relatively close together. Every $2 \cdot m^{\text{th}}$ layer should be enlarged:

$$m = \left(\frac{\lambda_1 \tilde{n}_p}{\lambda_p \tilde{n}_1} - k \right)^{-1} \quad (11)$$

For a Bragg mirror, the effective refractive index can be written in terms of the refractive index of the low index material n_L , the high index material n_H and the angle of incidence in air α

$$\tilde{n} = 2 \cdot \frac{\sqrt{n_L^2 - \sin^2 \alpha} \cdot \sqrt{n_H^2 - \sin^2 \alpha}}{\sqrt{n_L^2 - \sin^2 \alpha} + \sqrt{n_H^2 - \sin^2 \alpha}}. \quad (12)$$

Note, that even when the desired wavelength for the pump and for the laser are fixed, the angles can be used to fulfill the Bragg condition for both wavelengths.

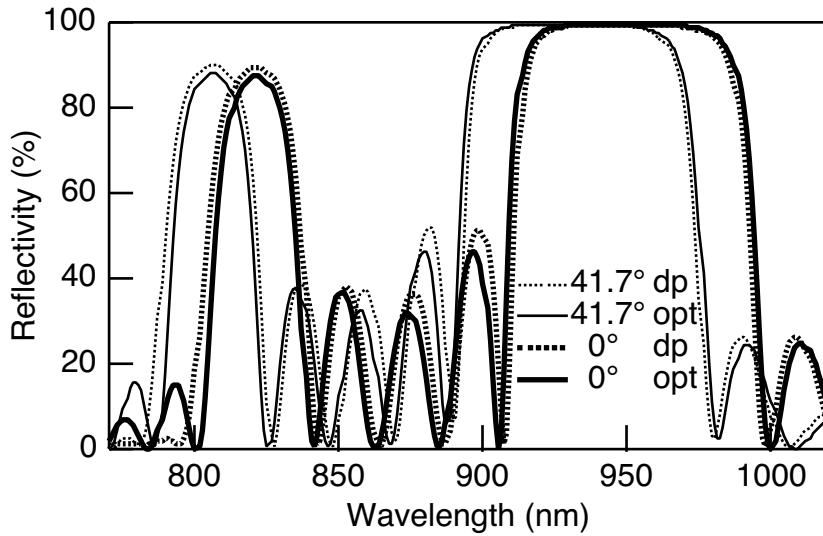


Figure 12. Reflectivity spectrum of the mirror under normal incidence (thick lines) and under 41.7° angle of incidence for unpolarized pump light (thin lines). The dotted lines are an analytical design (dp: double periodic) while the solid line is numerically optimized (opt: optimized).

In a design study we investigated the application-oriented case of a pump wavelength of 805 nm and a laser wavelength of 950 nm. We want to use a relatively large angle of

incidence for the pump light to allow pumping at an angle. Using $\text{Al}_{0.2}\text{Ga}_{0.8}\text{As}$ and AlAs the Bragg condition can be fulfilled for $2 \cdot m = 11$ with 41.7° angle of incidence for the pump light. In Figure 12 the calculated reflectivity is plotted for five periods of the eleven layers modified with 1.5 QWOT of the enlarged layer (55 layers total). The sequence is then numerically optimized. The reflectivities around 950 nm and 805 nm are only slightly improved. Figure 13 compares the start design with the optimized sequence. The periodicity is still clearly visible and no layer with extreme thickness has been introduced by the optimization.

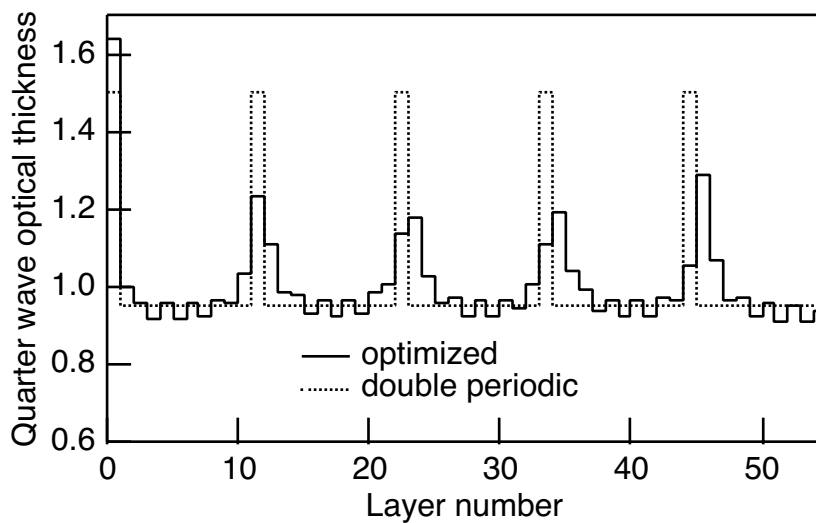


Figure 13. Quarter wave optical thickness for the mirror sequence. A periodic modulation of the start design (dotted) is still well visible after numerical optimization (solid).

3.2 Thermal management

In this Section we investigate the thermal property of an ELO gain structure. The reduced thickness of the semiconductor material leads to a nearly one-dimensional heat flow into the heat sink and makes the device power-scalable: for example the output power can be doubled by applying twice the pump power to twice the mode area without raising the temperature of the gain structure. However, at one point this power scalability breaks down, namely when the major part of the thermal impedance is caused by the heat sink and no longer by the semiconductor device.

3.2.1 Analytical temperature model

In Figure 14 a schematic of the parameters we use in this model are shown. We treat a thin layer (semiconductor Bragg mirror) of thickness d of material with relatively low thermal conductivity κ_{1d} in intimate contact with a good heat sink of conductivity κ_{3d} . The heat source has a gaussian lateral distribution with radius w ($1/e^2$ decay of the intensity) and a negligible thickness. The heat flow is one dimensional into the heat sink, which is kept at a constant temperature at its lower boundary. However, for mathematical convenience we assume that the heat sink expands to infinity. The assumption might seem surprising but it proves to be a good approximation (errors $<10\%$) for a heat sink thicker than $3w$ (determined numerically). That can be understood by the fact that the vicinity of the heat source contributes most to the thermal impedance because there the heat flow passes through the smallest cross-section. For the one-dimensional heat flow through the thin layer we get a temperature drop of ΔT_{1d} and to spread the heat in three-dimensional space we consider a contribution to the temperature of ΔT_{3d} in the heat sink material. (The temperatures are measured on the symmetry axis of the heat source). We make the assumptions that $\kappa_{1d} < \kappa_{3d}$ and $d \ll w$.

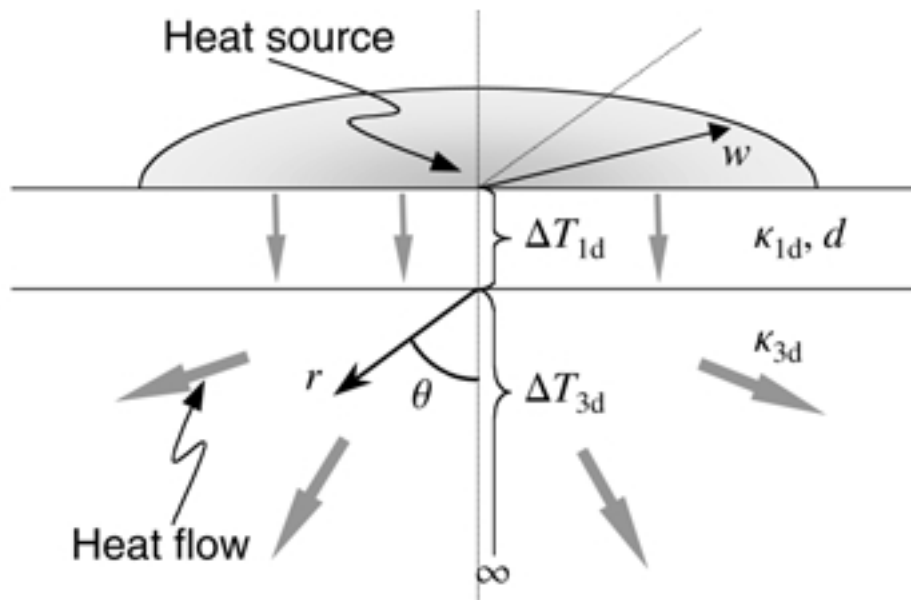


Figure 14. Schematic of the analytical heat model. The parameters are described in the text.

To transfer the heating power P_{heat} through the semiconductor layer, a temperature drop

$$\Delta T_{1d} = 2 \frac{P_{\text{heat}} d}{\pi w^2 \kappa_{1d}} \quad (13)$$

is needed at the peak pump intensity.

The further heat flow can be calculated when mirroring the half space of the heat sink to achieve infinite boundary conditions. We use a spherical coordinate system with the heat source centered in the origin

$$\rho(r, \theta, \phi) = 2 \frac{P_{\text{heat}}}{\pi w^2} \exp\left(-2 \frac{r^2}{w^2}\right) \left(\frac{\delta(\theta - \pi/2)}{r}\right), \quad (14)$$

where δ is the delta function and the factor $1/r$ accounts for a heat source with constant thickness in lateral direction. The temperature elevation in the center of the heat source compared to environment is

$$\Delta T_{3d} = 2 \frac{1}{4 \pi \kappa_{3d}} \int \frac{1}{r} \rho dV = \frac{P_{\text{heat}}}{\sqrt{2 \pi} w \kappa_{3d}}. \quad (15)$$

The factor of 2 takes into account that the heat flow is only into half space.

Note that ΔT_{1d} depends only on the heating intensity (in contrast to the heating power) while ΔT_{3d} increases with a larger pump spot but constant intensity. As a measure for the character of the heat spread (one-dimensional or three-dimensional) we can define the ratio R of the temperature drops in the thin layer and the heat sink

$$R = \frac{\Delta T_{3d}}{\Delta T_{1d}} = \sqrt{\frac{\pi}{8}} \frac{\kappa_{1d}}{\kappa_{3d}} \frac{w}{d}. \quad (16)$$

For $R \ll 1$ the main contribution of the thermal impedance is caused by the Bragg mirror and the heat flow is well approximated in a one dimensional model. The condition for power scaling is fulfilled and increasing the spot size proportional to the pump power leaves temperature, slope efficiency and the threshold intensity approximately constant. When we can provide enough pump power to keep the pump intensity constant, the output scales linearly with the spot area.

When $R > 1$ the thermal impedance is dominated by the three-dimensional heat flow in the heat sink. Increasing the pump spot while maintaining the pump intensity, raises the temperature. That does not mean necessarily that it is no longer possible to increase the output power by making the device larger (e.g. with a material system that shows good

performance even at high temperatures). But eventually threshold intensity and slope efficiency will be affected by the increased temperature and the loss in efficiency will dominate over the benefit of a larger device size.

We can define a critical radius w_{crit} when the crossover between one-dimensional and three-dimensional heat flow occurs. That means for $R = 1$ we find the critical radius to be

$$w_{\text{crit}} = \sqrt{\frac{8}{\pi} \frac{\kappa_{3d} d}{\kappa_{1d}}}. \quad (17)$$

Aiming for a good performance in terms of both efficiency and maximum output power, we will choose our pump radius to be $\approx w_{\text{crit}}$. In most cases, the thickness of the structure and the thermal conductivity of the semiconductor material do not allow much optimization. However, using a heat sink with a high thermal conductivity allows to increase the critical radius. Since the critical radius depends linearly on the thermal conductivity we find a quadratic dependence of the maximum output power. For example a copper heat sink with ≈ 10 times higher thermal conductivity than GaAs allows to extract 100 times more power than a gain structure on a thick GaAs substrate.

3.2.2 Numerical temperature simulation

To examine the limits of validity of the analytical model, we simulated the heat distribution in an ELO device using a commercially available finite element software (Solidis from ISE AG, Switzerland). For the heat sink we take a cube of 5 mm size cooled from the bottom (when the semiconductor layer is on top). The simulation is run with a $4.5 \mu\text{m}$ thickness of the Bragg mirror, a $1 \mu\text{m}$ thickness of the active area and a $1 \mu\text{m}$ thick AR structure. Heat sink and semiconductor are joined with a $1 \mu\text{m}$ thick solder junction. For the thermal conductivity we use $44 \text{ W}/(\text{K}\cdot\text{m})$ for GaAs [60], $1000 \text{ W}/(\text{K}\cdot\text{m})$ for Diamond, $400 \text{ W}/(\text{K}\cdot\text{m})$ for copper and $30 \text{ W}/(\text{K}\cdot\text{m})$ for the solder. For the gain structure, a superlattice of AlAs, $\text{Al}_{0.2}\text{Ga}_{0.8}\text{As}$ and GaAs, we take the value of $\text{Al}_{0.2}\text{Ga}_{0.8}\text{As}$ with $15 \text{ W}/(\text{K}\cdot\text{m})$ [60].

An example of the temperature distribution simulated for a device with a pump spot with $60 \mu\text{m}$ radius and a heating power of 512 mW is shown in Figure 15. For the heat sink copper is used. The center of the heat source is at the front edge of the cube and only a small fraction of the simulated volume is depicted. We refine the grid until a further intersection of the finite elements has only a negligible effect on the result (0.2% for

doubling the number of cells). The maximum temperature is reached in the center of the pumped spot, which is 22 K warmer than the bottom of the heat sink.

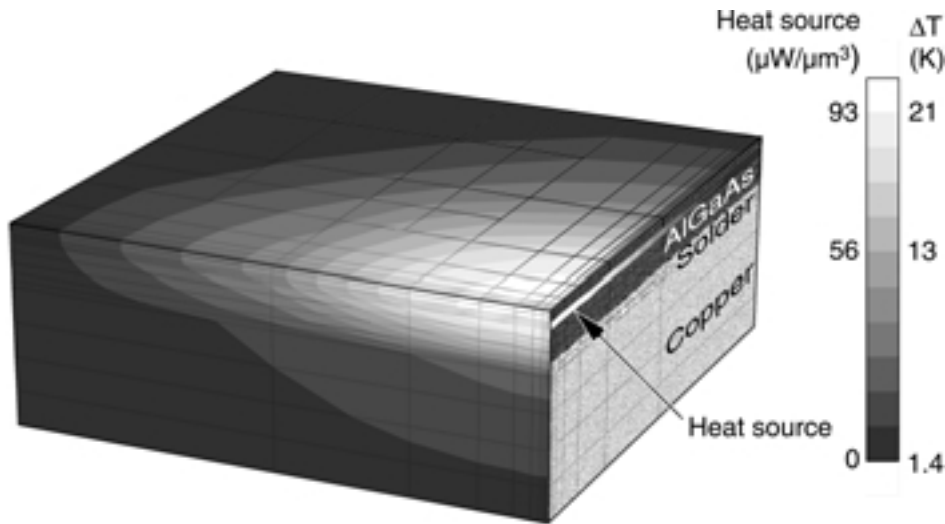


Figure 15. Temperature distribution in an ELO structure. The gain structure is soldered on a copper heat sink. The active area is heated with 512 mW on a pump spot with 60 μm radius. Only the close surrounding of the heat source is shown, while the simulation expands much further.

To compare the simulation with the analytical model we plot the temperature drops over the semiconductor and over the heat sink versus the pump beam radius (Figure 16). The heating intensity is kept constant at 10.2 kW/cm². The model for a one-dimensional heat flow in the semiconductor is accurate to 10% for pump radius >40 μm . For smaller spot sizes the cooling is more efficient because the heat spread in lateral direction has a significant contribution already in the semiconductor layer. The model for the three-dimensional heat flow in the heat sink is accurate to 10% for spot sizes <600 μm . For larger spots the analytical model underestimates the temperature because the heat flow is restricted by the sides of the heat sink. Cooling the copper heat sink from bottom and sides results in a slight overestimation of the temperature by the analytical model for large pump spots. After reaching the critical radius w_{crit} the main contribution to the temperature elevation is caused by the heat sink. Power scaling by simply increasing the pump spot will no longer work because the linear dependence of the temperature drop in the heat sink on the radius will eventually impair the efficiency of the laser. For the configuration with 5 μm semiconductor material and a copper heat sink the critical radius is 213 μm .

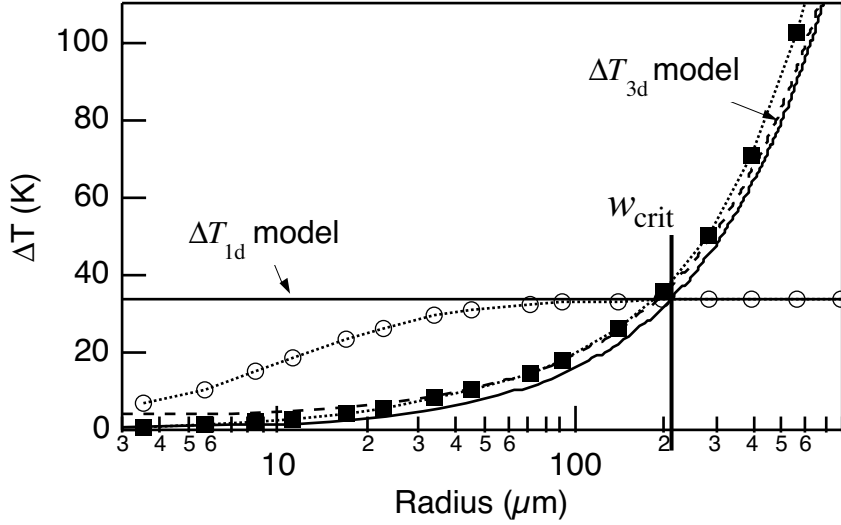


Figure 16. Comparison of analytical model with numerical simulations. The heating intensity is kept constant at 10.2 W/cm^2 while the radius of the pump spot is increased. Results from the numerical simulation are plotted for the temperature drop over the semiconductor ΔT_{1d} (circles) and over the heat sink ΔT_{3d} (squares). The analytical models are depicted as solid lines with the critical radius marked at the crossing point of the two lines. The dashed line also considers a one dimensional heat flow in the solder junction.

With further numerical tests we come to the following conclusions: The actual shape of the heat sink has little influence on the result e.g. a copper cube of 1000 times the volume results in a temperature increase of $\approx 2\%$ for a beam diameter of $400 \mu\text{m}$. Cooling the heat-sink from all sides rather than only from the bottom gives changes in the same range of a few percent. In contrast, removing the heat additionally by optically contacting a sapphire window to the device [18], reduces the temperature drop ΔT_{1d} by $\approx 50\%$. To find the range of validity of the model, the parameters are varied in the interval of $w \in [10, 850] \mu\text{m}$, $\kappa_{1d} \in [1, 50] \text{ W/(K}\cdot\text{m)}$, $\kappa_{3d} \in [1, 2000] \text{ W/(K}\cdot\text{m)}$, $d \in [3, 50] \mu\text{m}$ and $R \in [0.05, 100]$ under the conditions $w/d > 3.5$ and $\kappa_{3d} \geq \kappa_{1d}$. All combinations of the extreme values and additionally some intermediate sets are tested. For a large ratio ($w/d > 10$) the model is accurate to $\approx 10\%$ in all cases while for a smaller ratio the temperature is over estimated with the analytical model. The model is better when the thermal conductivity of the heat sink is much better than the one of the semiconductor.

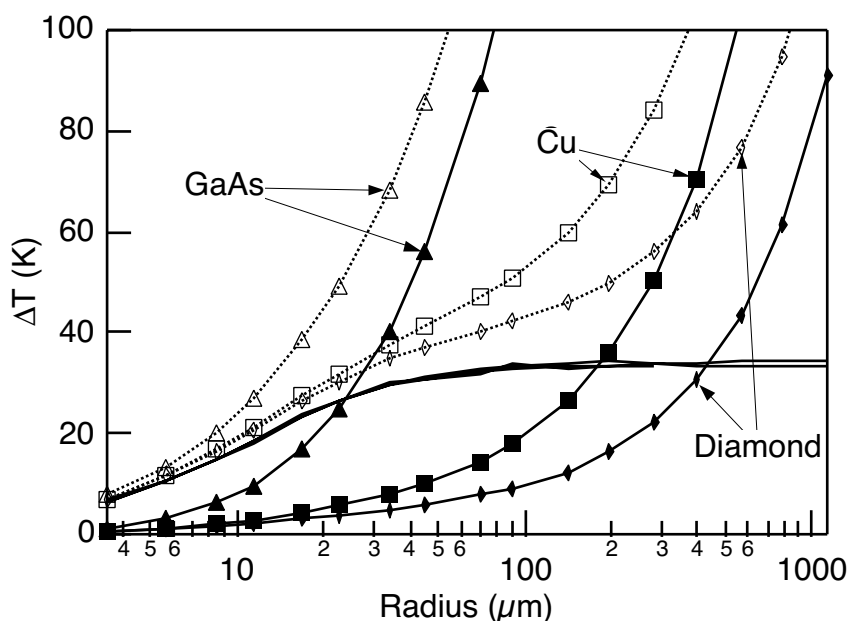


Figure 17. Temperature drop for a constant pump intensity plotted versus pump spot radius. The temperature differences are measured over the AlGaAs Bragg mirror (lines without marker), over the heat sink (solid lines with marker) and the total temperature elevation (dotted lines). Devices with a GaAs substrate (triangle) or directly mounted on a heat sink of copper (square) or diamond (rhombic) are simulated.

In Figure 17 devices on a heat sink made of diamond (rhombic marker), copper (square marker) or a $330\ \mu\text{m}$ GaAs wafer on copper (triangles) are simulated. The solid lines without markers are the temperature drops in the laser structure. As expected they are independent of the heat sink below and the three lines are covering. The solid lines with markers indicate the temperature drops in the heat sink and the dotted lines are the sum of the two. The critical radius obtained by this simulations are $24\ \mu\text{m}$ for the device remaining on the substrate, $185\ \mu\text{m}$ with a copper heat sink and $435\ \mu\text{m}$ using a diamond heat spreader.

3.2.3 Dependence of performance on pump spot size

We measure the slope efficiency and the threshold for different spot sizes. An ELO structure on a copper heat sink and the same structure sequence grown in reverse order on the $200\ \mu\text{m}$ thick GaAs substrate are investigated. The active area contains five quantum wells emitting at $950\ \text{nm}$. For pumping we use a Ti:sapphire laser at $808\ \text{nm}$. To vary the spot size we move the laser through the focus of the pump beam with minimal spot radius

of $12.7 \mu\text{m}$ and with a maximum of $239 \mu\text{m}$. The limitation for the spot size is given by the available pump power of 2 W and the threshold intensity of $\approx 4 \text{ kW/cm}^2$ or when the device is already overheated before reaching threshold. The laser is set up for continuous wave operation with a curved output coupler of 98.5% reflectivity and a radius of curvature of 15 mm. The heat sink temperature is stabilized at 3°C . For each sample four scans through the focus are taken at slightly different spots on the wafer.

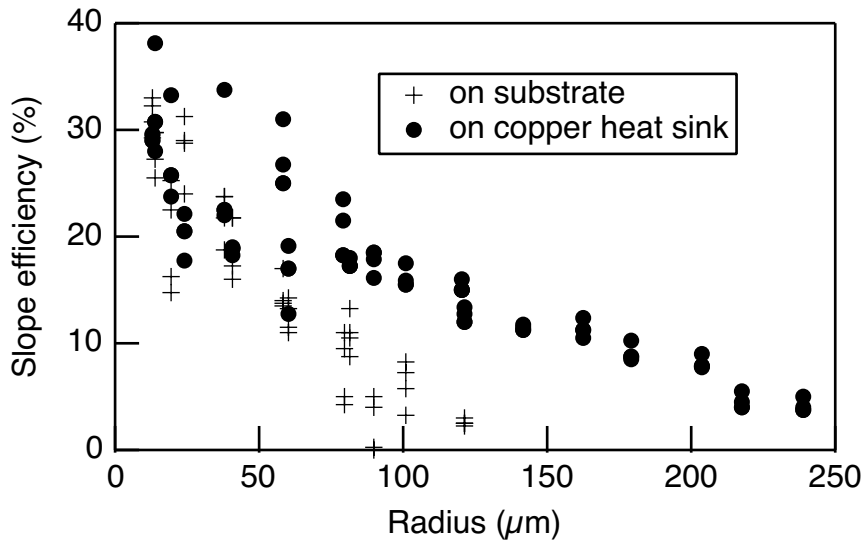


Figure 18. Slope efficiency versus pump radius. The slope efficiency is measured close to threshold.

In Figure 18 the slope efficiency is plotted versus the radius. The maximum slope efficiency can be achieved with small devices and reaches $\approx 35\%$ independent of the heat sink. The large deviations of the slope efficiency for small radii is mainly due to some astigmatism of the pump beam resulting in a variations of the overlap of laser mode and pump mode. For larger spots the laser is run with multiple transverse mode allowing the laser to adapt its mode to the pump spot. The slope efficiency of the structure remaining on the GaAs substrate lases only to a pump spot radius of $w = 110 \mu\text{m}$. For larger spots the thermal impedance is too high for the laser to reach threshold. The sample on the copper heat sink still lases with a slope efficiency of 5% for a spot size of $240 \mu\text{m}$.

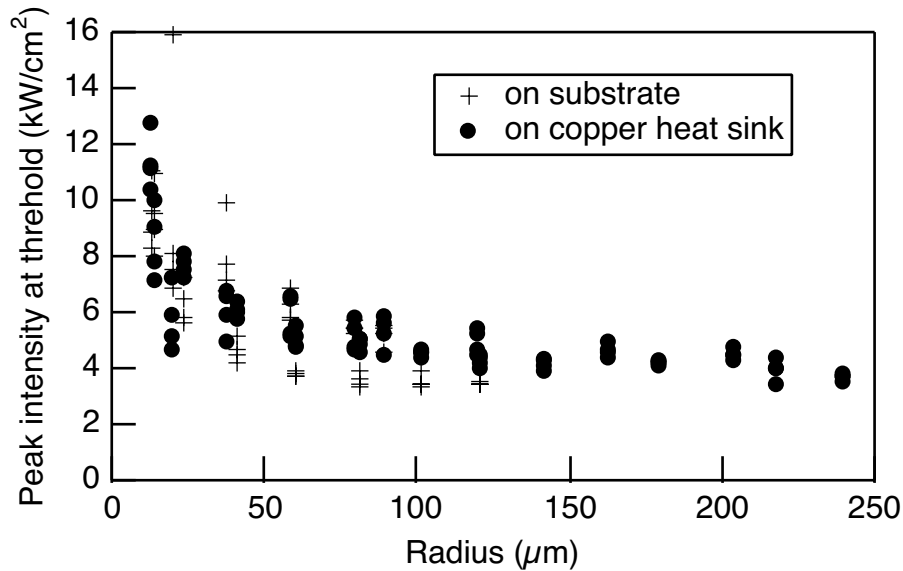


Figure 19. Intensity in the center of the pump beam at threshold dependent on the radius. The threshold is $\approx 4 \text{ kW/cm}^2$ for larger pump spots and increases for very small pump spots.

Figure 19 shows the threshold intensity for the scans through the focus of the pump beam. The threshold is $\approx 4 \text{ kW/cm}^2$ (peak intensity in the center of the pump beam) for spot sizes larger than $50 \mu\text{m}$ independently of the heat sink below. We believe the overlap of pump and laser beam as well as the cavity losses close to the stability limit to be responsible for the increased threshold for small radii.

3.3 Growth

For the growth we used a metalorganic chemical vapor deposition (MOCVD) system. The growth rates and compositions for the materials used on GaAs substrates had to be calibrated first and monitoring of the drift over the time is essential for high-quality structures. The gain structures are grown on $200 \mu\text{m}$ thick (100) GaAs wafers. We use a growth temperature of 750°C for the mirror and the anti-reflective structure and a reduced temperature of 610°C for the active region.

In a MOCVD reactor metalorganic and hydride compounds (so called precursors) are used to transport the elements of the semiconductor to the wafer. In a very simple model, the growth process can be described in four steps: 1) mass transport of the reactants to the

growth surface, 2) reaction at or near the surface, 3) incorporation of the new material, and 4) removal of the reaction by-products. For the material systems and the growth conditions we are using, the growth rate is determined by the transport of group III reactants to the growth surface [61, 62]. A direct consequence is a low dependence of the growth rate on the temperature (in contrast to reaction or incorporation limited growth). However, there is a spatial variation of the growth rate due to the depletion of the metalorganic compound in the gas flow. Partly this can be compensated for by rotating the wafer during growth while a laminar gas flow from one side is maintained. The remaining inhomogeneities have rotational symmetry over the wafer.

Theoretically the optical properties are completely defined with the material compositions and the layer thicknesses. However, to measure the material parameters accurate enough to know the optical properties to the desired accuracy is very difficult. So calibration is done preferably in two steps: In a first step physical thickness and material compositions are measured and adjusted and in a second step optical methods are used to fine tune the spectral properties. Several techniques for both types of calibration are discussed in this Section.

3.3.1 Calibration of composition and thickness

Atomic force microscopy

The technique described here takes advantage of different oxidation rates for several materials. Especially GaAs shows nearly no oxidation in air while AlAs and aluminum rich AlGaAs oxidizes very quickly. After cleaving, the newly exposed semiconductor material starts building in oxygen and thereby increases the volume. In absence of an other dimension of expansion, the oxide swells out of the cleaving plane. Scanning with the AFM over this plane gives a profile proportional to the amount of built in oxygen. This method allows to measure the physical thicknesses directly and a whole layer stacks can be analyzed layer by layer in one scan. For the analysis of mirror structures, limits of the resolution are caused by the oxidation rate of AlAs: after the first growth of the oxide perpendicular to the cleaving plane, it starts bulging in all directions and blurs the interface between the materials. With special structures designed for AFM measurements this bulging can be circumvented.

The pictures in Figure 20 – 22 are gray scale images of the heights over the scan. For measurements the scanned data were interpolated with a slight tilt calculated to match the

growth direction exactly with one scan direction. Then an average over the laterally separated single scans is taken. The average height over layer thickness is plotted in white.

In Figure 20 an example of a calibration structure for the $\text{Al}_{0.2}\text{Ga}_{0.8}\text{As}$ growth rate is shown. Five periods of 4 minutes $\text{Al}_{0.2}\text{Ga}_{0.8}\text{As}$ and 33 seconds AIAs were grown. That should roughly correspond to 150 nm $\text{Al}_{0.2}\text{Ga}_{0.8}\text{As}$ and 3 nm AIAs. Here, the AIAs layers are used as markers to measure the thickness of the AlGaAs. A possible error in the growth rate of AIAs does not derogate the measurement, since the percental thickness is so small. The AIAs markers can be clearly resolved and the distance between the AIAs markers is 152.1 ± 1.3 nm, giving a growth rate of 37.3 nm/min for $\text{Al}_{0.2}\text{Ga}_{0.8}\text{As}$. This method is suitable for materials with a low oxidation rate and which are close to lattice matched to the substrate.

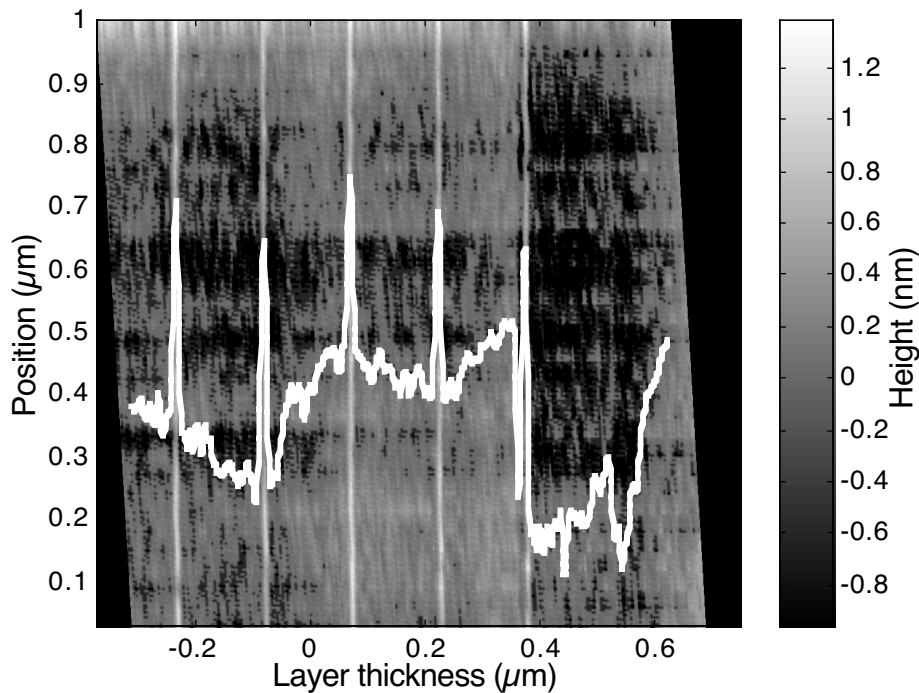


Figure 20. AFM picture of a calibration structure with 5 periods of 150 nm $\text{Al}_{0.2}\text{Ga}_{0.8}\text{As}$ / 3 nm AIAs. The white line is an average of the height over the image perpendicular to the growth direction. (Sample R2837)

The method can be inverted with low oxidizing markers in a strongly oxidizing material but with a lower accuracy. In Figure 21 a scan of such a structure is shown. Four time 15 minutes of AIAs growth were separated by 9 s of GaAs growth. In the scan, the dips

of the GaAs can still be resolved even so the bulging of the oxide has advanced quite far. Note the height of the oxide of roughly 70 nm compared to the thickness of 80 nm. At the moment of the scan, the cleaved surface was exposed to air for about an hour. Higher accuracy could be achieved when cleaving and measuring in an artificial atmosphere with a controlled amount of oxygen. The outer bulges can not be used for the measurement, since the edges are not well defined. However the thickness of the middle two AlAs layers is 76.1 nm and 70.5 nm, respectively, resulting in a growth rate of 4.89 nm/min for AlAs.

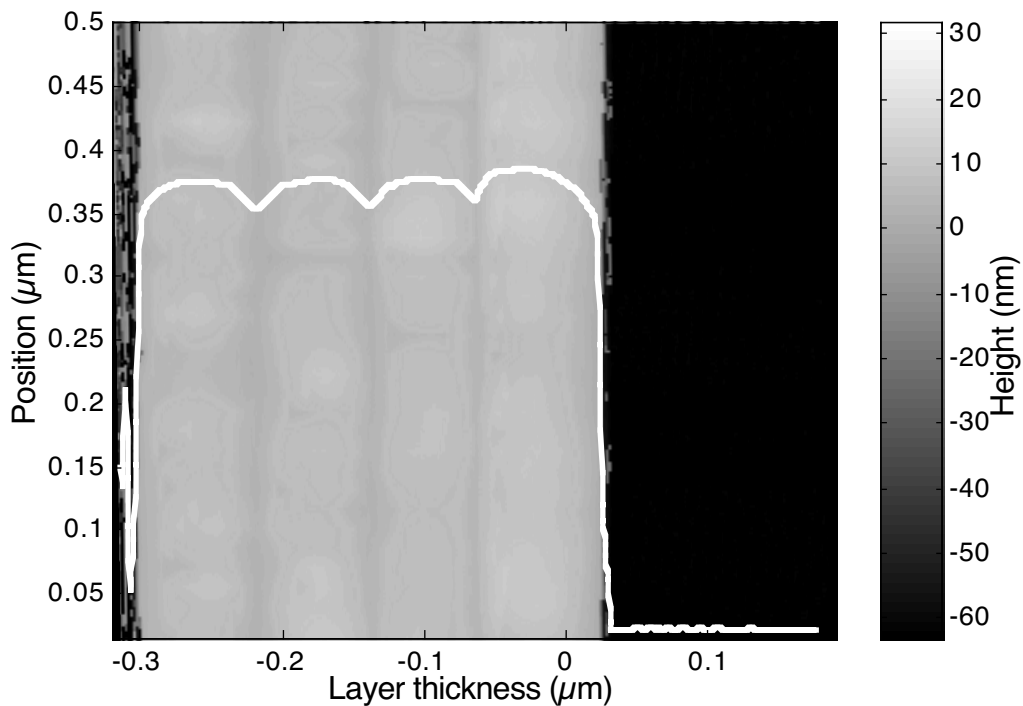


Figure 21. AFM picture of a calibration structure with 4 periods of 80 nm AlAs / 3 nm GaAs. The white line is an average over the image perpendicular to the growth direction. (Sample R2839)

In Figure 22 a) a concatenation of seven scans over a whole VECSEL structure designed for epitaxial lift-off is shown. Clearly visible is the double periodic structure of the mirror, the active area (the QWs are not visible) and the anti-reflective structure. The thick layer 6.5 μm deep in the structure is the first etch stop layer. Such a scan allows to measure the stability of the growth rate during a run lasting for about 15 hours. The oxidation has progressed to an extent, that most of the GaAs and Al_{0.2}Ga_{0.8}As layers are hidden under the bulging of the oxidized AlAs layers. Assuming that the minima in the height profile is

in the middle of the gallium rich layer allows to compare the designed thickness with the grown one. A plot of the expected and the measured spacing between the minima is given in Figure 22 c). A few layers (open circle in Figure 22 c) have not been completely covered by the oxide and the interface between the different materials cannot be defined clearly. For the others the ratio between expected and measured spacing is plotted in Figure 22 b). All measurements are within 5% of expectation and no significant drift of the growth rate can be observed.

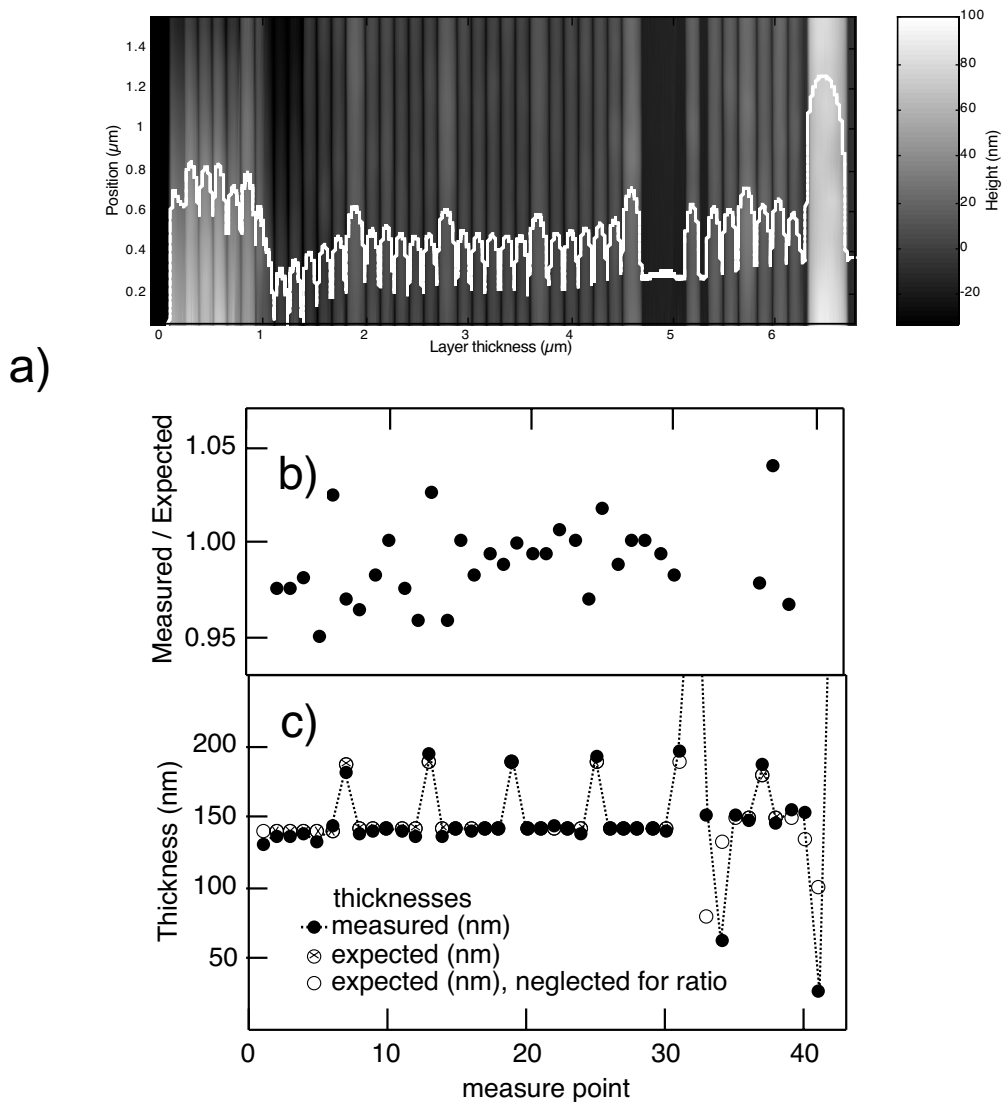


Figure 22. AFM analysis of a VECSEL structure. a) the AFM scan and the profile of the height over the cleaved surface is plotted. c) the designed and measured spacing of the fringes in the profile is plotted and in b) the ratio of the two indicates that the growth rates are stable during the growth run within the limits of measurement accuracy. (Sample R2990)

X-ray diffraction

Diffraction at the crystalline structure with x-ray is especially suited to determine the material composition. The short wavelength allows to resolve the lattice constant a of the crystal. For ternary materials we can assume a linear dependence of the lattice constant on the material composition. Hence, a measurement of the lattice constant is also a measure for the material composition. But also interfaces of a superlattice lead to interferences and allow to measure layer thicknesses.

The diffractometer we used has a x-ray source emitting at the CuK_α line with a wavelength $\lambda = 1.5410 \text{ \AA}$. To achieve a monochromatic collimated beam the (400) reflection from an InP crystal is used. The angle of the sample relative to the beam is varied while the diffracted photons are counted resulting in a so called rocking curve. Assuming a (100) wafer with the atomic layers parallel to the surface, we can use the Bragg condition

$$a \sin \theta = m \frac{\lambda}{2} \quad (18)$$

with θ the angle between the wafer surface and incident beam and with m the order of the Bragg reflection. A GaAs substrate has its fourth order Bragg reflection at $\theta = 33.03^\circ$. With a linear approximation we find the relative lattice mismatch of a grown material to be

$$\frac{\Delta a}{a} = -\frac{1-\nu}{1+\nu} \frac{\Delta \theta}{\tan \theta}, \quad (19)$$

with $\Delta \theta$ the relative angle between the substrate peak and the layer peak in the rocking curve, and ν the Poisson ratio ($\nu = 1/3$ as long as the misfit can be accommodated by elastic strain). In Table 2 some coefficients are listed used to transform the relative angles into material compositions.

Table 2. Coefficients to calculate the composition of a ternary GaAs based material from the peak separation $\Delta\theta$ in a rocking curve taken with the $\text{CuK}\alpha$ line. ($x = c \cdot \Delta\theta + d$, LC: lattice constants from www.matweb.com and Ref. [60])

	Factor c % / arcsec	Offset d %	LC($x = 0$) Å	LC($x = 1$) Å
$\text{Al}_x\text{Ga}_{1-x}\text{As}$	- 0.285	–	5.65330	5.66069
$\text{In}_x\text{Ga}_{1-x}\text{As}$	- 0.00520	–	5.65330	6.05838
$\text{GaAs}_{1-x}\text{P}_x$	0.01423	–	5.65330	5.45177
$\text{In}_x\text{Ga}_{1-x}\text{P}$	- 0.00505	48.5	5.45177	5.86875

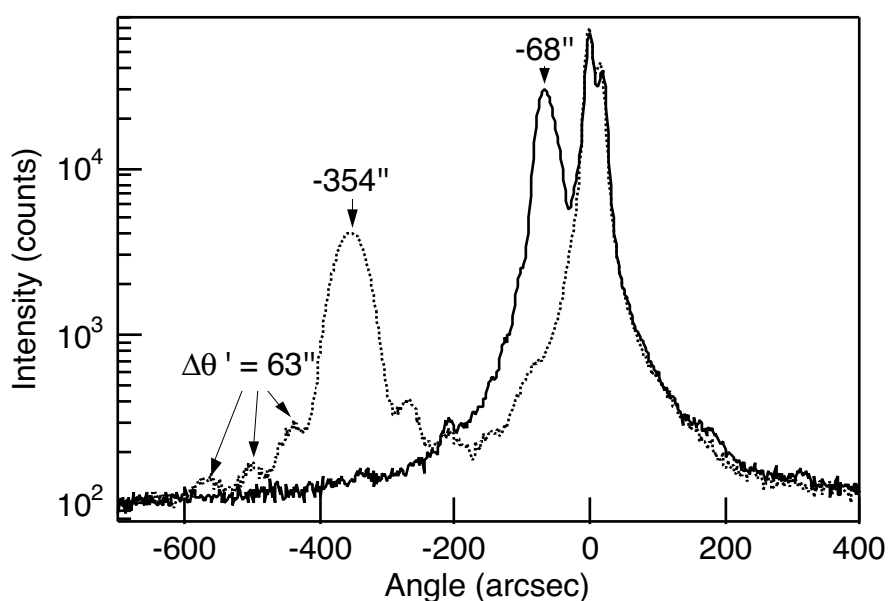


Figure 23. Rocking curves of the two samples shown in Figure 20 (solid) and Figure 21 (dotted). (Samples R2837 and R2839)

In Figure 23 the rocking curves of the two calibration structures described in the AFM section (Figure 20 and Figure 21) are shown. The peak at -354 arcsec from the substrate peak corresponds to pure AlAs (calculated $x = 101\%$) and -68 arcsec is a Aluminum content of $x = 19.4\%$. The fringes in the dotted curve are caused by interfaces between materials. The spacing corresponds to a layer thickness of 301 nm. That is in good

agreement with the AFM measurement of 302 nm for the complete AIAs package (4 AIAs layers of 73.3 nm and 3 GaAs markers of 3 nm).

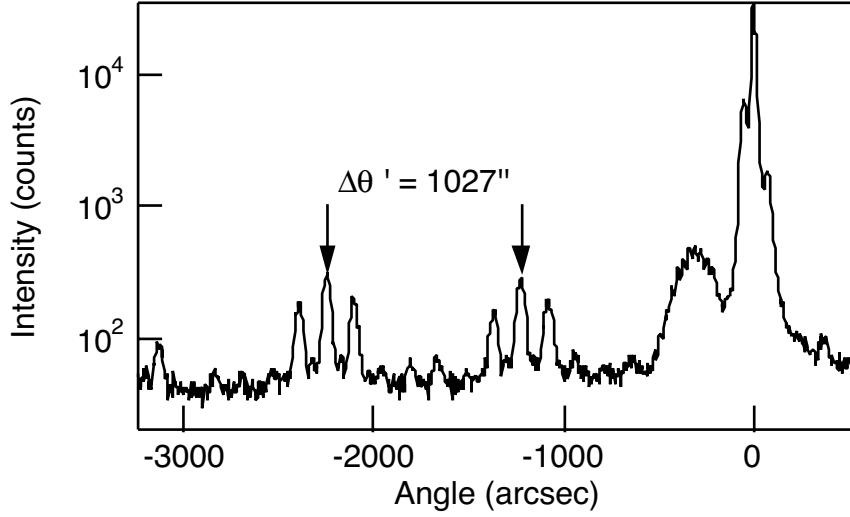


Figure 24. Rocking curves of 9 InGaAs quantum wells place in three groups where the three quantum wells are separated by 10 nm thick GaAs spacer layers. (Sample R3234)

To measure layer thicknesses d we calculate the angular spacing of two consecutive Bragg reflections in the linear approximation of $m \gg 1$:

$$d = \frac{\lambda}{2 \cos \theta} \frac{1}{\Delta \theta'}, \quad (20)$$

where $\Delta \theta'$ is the angular spacing of a repeating pattern in the rocking curve. For thick layers the fringes are narrow spaced and the resolution of the instruments limits the significance of the measurement. However, for thin layers in a periodic structure like a multi-quantum well (MQW) structure, the peaks can be very pronounced and the measurement accurate. In Figure 24 a rocking curve of a quantum well structure is shown. A total number of nine InGaAs quantum wells are grown in stacks of three wells separated by 10 nm GaAs spacers. An average spacing of the fringes is 1027 arcsec corresponding to a thickness of 18.5 nm in physical space or a quantum well thickness of 8.5 nm.

It has to be mentioned here, that much higher resolutions can be achieved with double crystal x-ray diffraction (DCXD). Simulation and fitting to the measurement of such high

resolution rocking curves allows to gather much more data (i.e. layer thicknesses, strain, layer quality [63]) than we can deduce from our measurements.

Transmission Electron Microscopy

Another method to determine the thickness of thin layers is transmission electron microscopy (TEM). In Figure 25 an example of a test structure with three InGaAs quantum wells is shown. The sample is cleave to obtain a clean 90° angle. The electron beam is transmitted through the edge and the sample is oriented to have the growth direction in the image plane (so-called wedge TEM). The picture was taken with electrons accelerated with 200 kV. A cross-section of the image is taken at the marked position and is plotted in the inset. Measuring the well width at half the amplitude gives a thickness of 7.2 nm. Assuming the GaAs thickness is precisely 10 nm (as designed) results in a QW-thickness of 7 nm. This single package of three quantum wells only gives a broad feature in the rocking curve making a comparison with the corresponding X-ray result difficult.

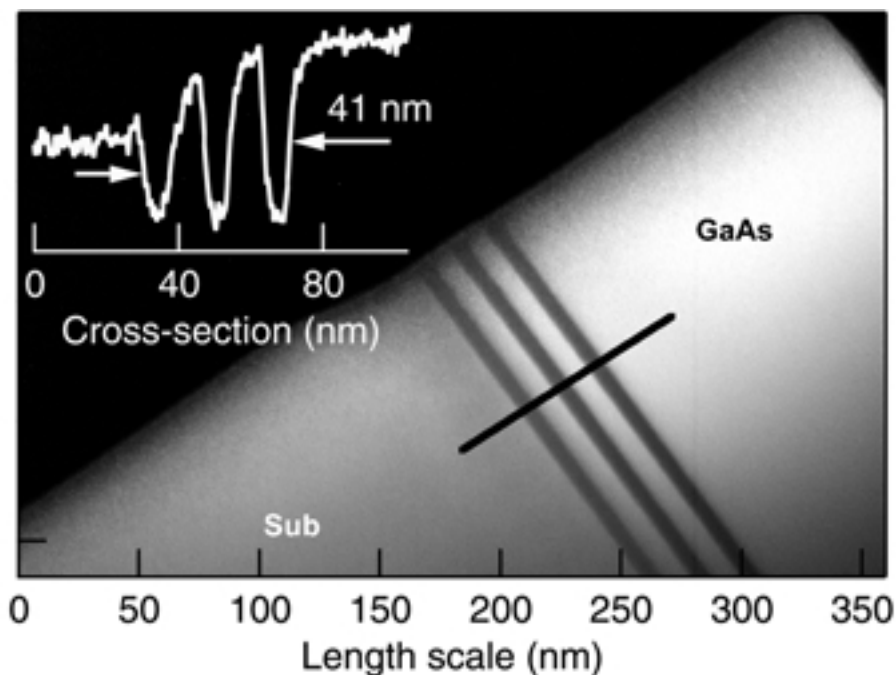


Figure 25. TEM image of a structure with three quantum wells. The inset shows a cross-section perpendicular to the quantum wells at the position marked with the black line. (Sample R3025)

TEM is a powerful tool for semiconductor characterization. Measuring thin layer thicknesses is only one task which can be performed. Additionally, wedge TEM allows to determine material compositions by the different transmission dependence on the distance from the edge. Thinning the structure to a few nanometers and with higher electron energies the crystalline structure can be resolved revealing even single defect states. However, in comparison to x-ray, sample preparation is more time consuming and in our work we used TEM only to check the results determined routinely with x-ray.

3.3.2 Calibration of optical properties

Optical spectrum

The fine tuning of the growth rate is done by measuring and fitting the optical reflectivity spectrum. When using the layer thickness determined by other methods and the literature values for the refractive indices [64, 65], the reflectivity spectrum can not be grown precise enough to achieve a good device. Especially for ternary materials the error in the measurement of the material composition enters over the dispersion relation into the reflectivity spectrum. Therefore it is important to have a method which depends directly on the optical thickness.

For interpretation of a reflectivity spectrum we can regard the amplitude and the wavelength content independently. Considering the simple case of a Bragg mirror we find that the wavelength content (e.g. the wavelengths of the minima in the reflectivity) is determined by the optical thickness of a layer pair. The amplitude depends on the duty cycle (the ratio of the optical thicknesses of the low and the high index layer) and on the contrast of the refractive indices of the two layer materials. Experimentally we can measure the wavelength content very precisely while some inaccuracy has to be faced in the measurement of the amplitude. Some narrow fringes are smeared out by the finite bandwidth of the instrument and by averaging over wafer inhomogeneities with a relatively large spot of a few millimeters. Another source of errors is introduced when the reflection from the back side is not well known (e.g. when the substrate shows some residual absorption in the bandgap reducing the reflection from the back side). Preferably single side polished wafers are used to avoid these errors.

A complex gain structure consists of ≈ 100 layers and for each layer a few parameters influence the reflectivity. To obtain a meaningful result from a fit we need to restrict the open parameters to the ones expected to vary in a MOCVD machine. Taking the growth

rate and composition during a growth run as fixed has proven to be a good assumption. Between different runs the growth rate is seen to drift slightly and a list of current values must be maintained for successful growth of such complex structures. The fitted growth rates can be reproduced very accurately and experimentally delicate tasks such as the absolute amplitude calibration of the spectrum or the smearing of spectrally narrow features are tested to have little influence on the fit result.

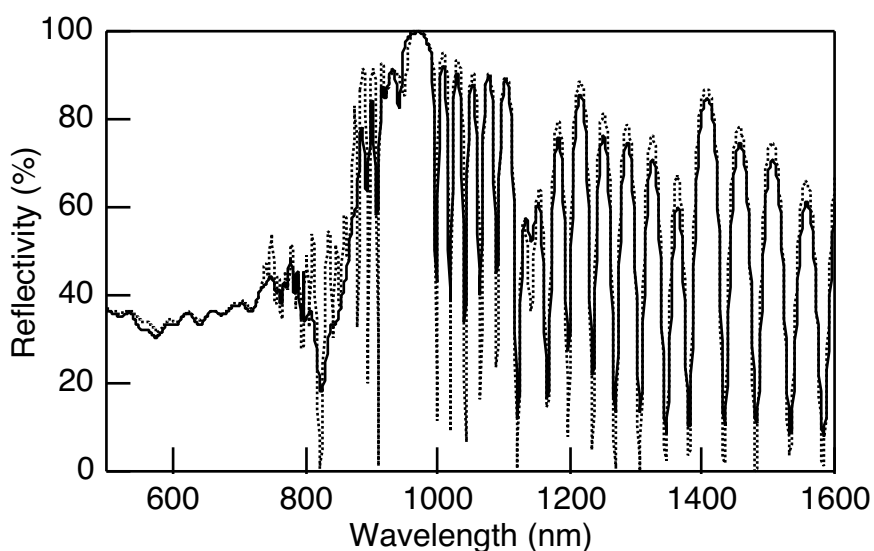


Figure 26. Reflectivity spectrum of a completely processed gain structure. To fit (dotted) the measurement (solid), corrections in the order of 1% for the three AlGaAs materials are needed. (Sample R3350 4b)

In Figure 26 the reflectivity spectrum of a gain structure after soldering and etching is shown. To get a reliable fit, a measurement over a broad spectral range is desirable. Calibration of the spectral amplitude response of the instrument is done with a silver mirror which is assumed to have a spectrally flat reflectivity over the whole range. The absolute scaling is done most precisely by using the stop band in the transparent regime of the quantum wells. For structures without stop band absolute scaling can be done with the reflectivity of the silver mirror, assumed to be 97% resulting in amplitude errors of typically 1%. The fit reveals errors in the growth rate of -0.3% for GaAs, $+1\%$ for AlAs and -0.3% for $\text{Al}_{0.2}\text{Ga}_{0.8}\text{As}$.

Photoluminescence

To calibrate the laser wavelength we use photoluminescence (PL) measurements. Two different setups are used. With a commercially available instrument the PL is measured at room temperature for a low excitation power of ≈ 10 mW. The spectrum is spatially split with a grating and measured with a detector array. This method allows fast data acquisition and the wafer can be mapped revealing growth errors or defects.

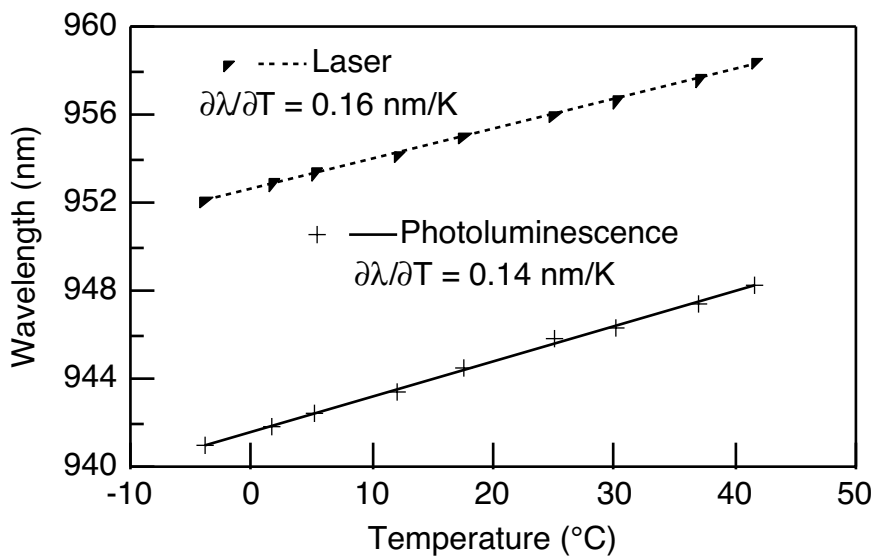


Figure 27. Peak wavelength of photoluminescence and laser for different temperatures. (Sample R3350 4b)

To measure the PL under working condition we collect the light emitted beside a running laser and analyze it with a optical spectrum analyzer. The signal shows the PL as well as scattered light at the laser wavelength. In Figure 27 the peak wavelength for both the laser and the PL is plotted versus the temperature of the heat sink. We measured shifts of the laser wavelength relative to the PL peak between -15 nm to 40 nm on various samples! That is due to the resonance between mirror and the residual reflectivity of the AR structure, which is dominant enough to force the laser to operate near the resonance wavelength even when the intrinsic gain maximum is tens of nanometers away. To find the best offset between PL and laser wavelength further investigation are needed but good devices are demonstrated with the laser wavelength about 10 nm longer than the PL peak.

3.3.3 Wafer inhomogeneity

As discussed in Section 3.3 the growth rate varies over the wafer. Since the wafer is rotated during growth we have rotational symmetry and we can measure the growth rate dependent on the radial position.

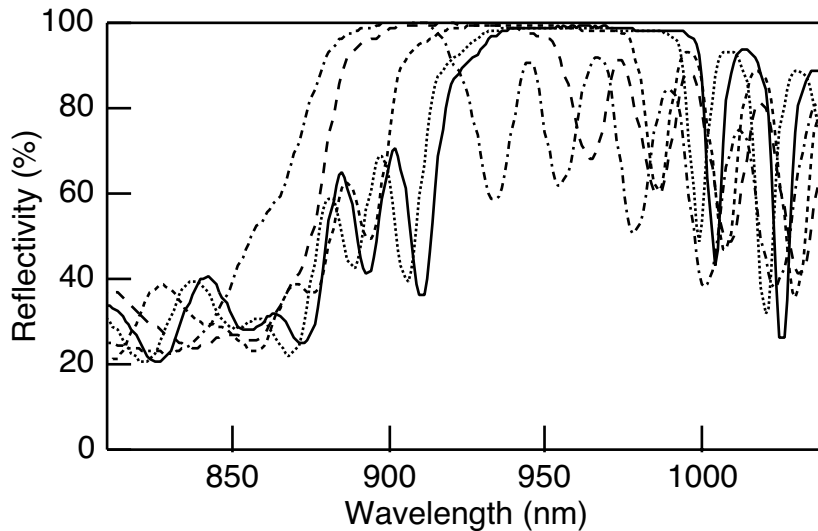


Figure 28. Reflectivity spectra for different radial positions on the wafer. The solid line is measured near the center of the wafer while the consecutive traces are taken with 5 mm spacing toward the edge of the wafer. (Sample R3350 4a-e)

In Figure 28 the reflectivity near the stop band of a gain structure (grown as reversed sequence for ELO) is plotted for different positions on the wafer. The measurement was taken at five points with 5 mm spacing from the center toward the edge. From a 2-inch wafer typically only the inner inch can be used while the stop band shifts too much in the outer ring. The sample shown here has a shift of the center wavelength of 19 nm for the inner inch.

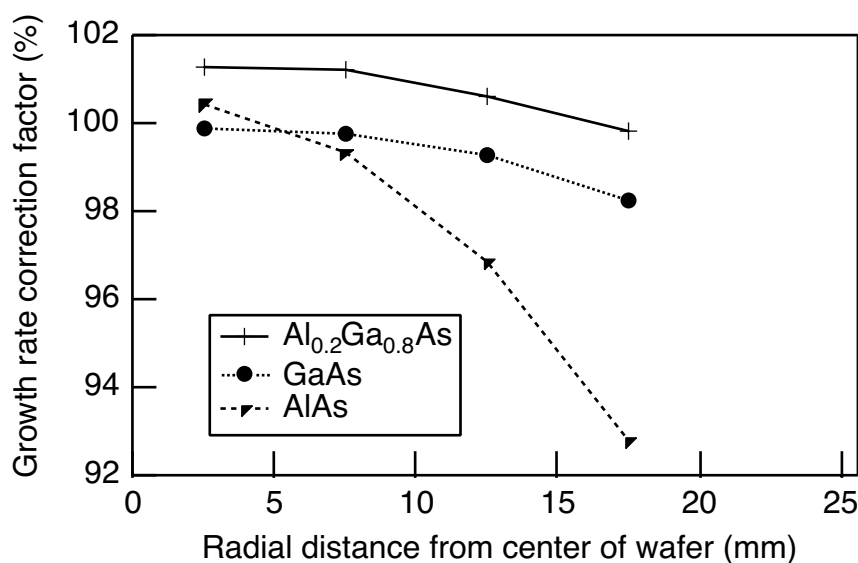


Figure 29. Correction factors for the growth rate measured as function of the radial position on the wafer. The values are extracted from a fit to the reflectivity spectrum. (Sample R3350 4a-d)

The reflectivity spectra are used to fit a correction factor of the growth rate. Figure 29 plots the corrections for the three materials AlAs, GaAs and $\text{Al}_{0.2}\text{Ga}_{0.8}\text{As}$ dependent on the position on the wafer. For the spectrum taken at 22.5 mm radial distance the fit did not converge properly. For calibration of the growth rate the measurement at 7.5 mm is used. The largest contribution to the wafer inhomogeneity is caused by the variation of the AlAs thickness.

3.4 Processing

In Section 3.2 we came to the conclusion that a low thermal impedance is essential for high power performance. We want to have the active region separated from the heat sink only by the semiconductor Bragg mirror. In this Section we describe how soldering and substrate removal is done in a way to achieve a good thermal contact, reliable mechanical support for the structure and a smooth and flat surface.

3.4.1 Soldering

The requirements for soldering are demanding. The remaining semiconductor structure is only $\approx 6 \mu\text{m}$ thick. The solder junction must be hard enough that it can provide mechanical support on the heat sink, but it must be soft enough that the crystal sustains no damage during soldering. Any void in the solder junction locally reduces the heat conductivity and can be seen as burned spot in the device after exposure to the pump light.

Soldering is the formation of an alloy between a substrate metal and a solder. To facilitate this process the solder is melted and brought in intimate contact with the substrate metal. The conditions to achieve the contact are a dirt and oxide free surface of both metals and wetting of the substrate metal. Wetting depends on the surface tension of the solder and on the metal-metal bond energy between the two metals. A measure for the first is the vapor pressure of the solder while the second is in close relation with the solubility of one metal in the other [66].

Typically, oxidation of the solder produces a solid oxide film adhering to the molten metal. Most commonly flux is used to reduce the oxide and to decrease the surface tension of the solder. However, all our attempts to solder a gain structure to a heat sink using flux failed because of voids incorporated in the solder junction. We suspect that vaporizing flux is trapped during the solder process causing these voids.

Note that the semiconductor is not joined directly to a metal by soldering. Sputtering of a 30 nm thick titanium layer on the wafer is used instead, which is known to be highly adhesive. Additionally a 200 nm thick platinum layer is applied to prevent diffusion of the solder metal into the semiconductor.

Sn/Au solder

Eutectic tin-gold alloy is the only solder used commercially for fluxless soldering. It does not oxidize in air even when molten and it is wetting on gold without flux. However, the melting point is relatively high at 280°C and it has a high yield strength, transferring the stress of a different expansion coefficient of the heat sink to the semiconductor crystal. That limits its use to either small devices, where the stress can be incurred by elastic deformation or to heat sink materials with an expansion coefficient matched to GaAs. Submounts with 90% tungsten and 10% copper have the same expansion as GaAs and can be purchased with a Sn/Au film applied to one surface (Sumitomo Electronics

Europe). The heat conductivity is $180 \text{ W}/(\text{K}\cdot\text{m})$ which is 2.2 times lower than pure copper and >5 times lower than synthetic diamond.

For soldering, the wafer is metalized with 30 nm titanium, 200 nm platinum and 100 nm gold. A dice of a few millimeter size is cleaved from the wafer and placed on the submount. Heating to $\approx 300^\circ\text{C}$ under weak pressure (a few grams) in normal ambient gives satisfying results.

Soldering with tin-gold on diamond has also been investigated. After removing the substrate a cross-hatch pattern in $[100]$ directions is observed. We believe that the crystal was crushed along these lines due to the different expansions during cooling phase of the soldering process. The size of the unbroken areas is in the range of $20 \mu\text{m}$. Lasing can be achieved when using a cavity with a small mode area on the gain structure.

Indium solder

Indium is very ductile and thus can incur the stress during cooling down from soldering by plastic deformation. Furthermore, the low melting point of 156°C further reduces the problem of different expansions of sample and heat sink. However, indium has a strong tendency for oxidation, making it difficult to solder without flux.

Recently, W. W. So et al. [67] published a way to circumvent oxidation during soldering. We developed a similar process but replaced the H_2 protection environment during soldering by vacuum. On the epi-side of the wafer a sequence of 30 nm titanium, 200 nm platinum, 5000 nm indium and 100 nm gold is sputtered in one high vacuum cycle. The titanium is used for adhesion on the semiconductor surface, and platinum builds a diffusion barrier for the indium. The indium is protected against oxidation with a stable layer: Still in the vacuum chamber the gold interacts with the indium to form an AuIn_2 intermetallic compound. (The metalization looks silvery and not golden.) With this protection layer the wafer can be handled in air. However, attempts to solder after a month exposure to air revealed some difficulties and might indicate a residual slow oxidation. Copper submounts of $5 \text{ mm} \times 5 \text{ mm} \times 1 \text{ mm}$ are eroded and lapped to have a planarity and roughness of $\approx 1 \mu\text{m}$ and are then coated with 30 nm titanium, 200 nm platinum and 100 nm gold.

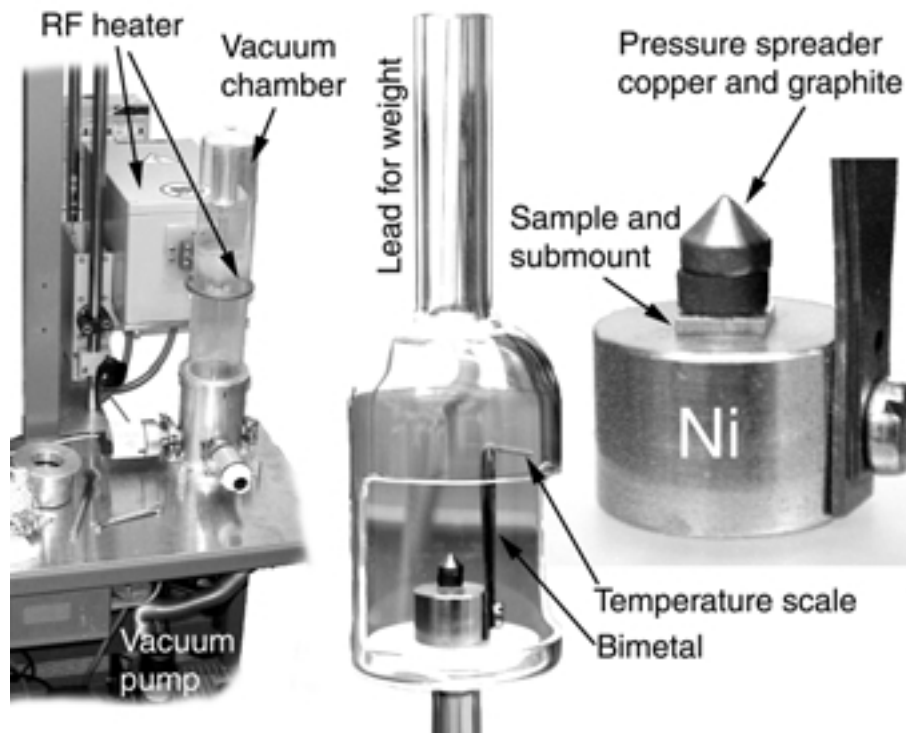


Figure 30. Setup for fluxless indium soldering. The solder is sputtered on the semiconductor wafer and covered with gold to prevent oxidation. A dice of the wafer is placed on a submount and is pressed on with ≈ 300 kPa. To avoid oxidation during the process and to prevent voids in the junction, soldering is executed in vacuum.

In Figure 30 the setup used for soldering is shown. A 4 mm x 4 mm large dice is cleaved from the metalized wafer and is placed on the submount. Avoiding any dust in the gap between sample and submount is important since a maximum of $5 \mu\text{m}$ solder is available. A piece of nickel is used as 'hotplate' because of the high coupling efficiency to the radio frequency (RF) field used for heating. The deflection of a bimetal stripe is used to monitor the temperature. Submount and dice are placed on the nickel piece and are pinned down with a pressure of 300 kPa. The pressure is generated with modular glass weights allowing to adjust the pressure to the size of the dice. To distribute the pressure equally over the sample a metal cone and a graphite disc is used. Everything is placed in a vacuum chamber and a pressure $<10^{-4}$ mbar is maintained for >30 min to allow the air to escape from the gap between sample and submount. With an RF source the nickel is heated to a temperature of $\approx 250^\circ\text{C}$ for about 10 minutes. (The heat transfer to the submount is slow and melting of the solder is typically not observed until the nickel reaches $\approx 200^\circ\text{C}$.) Note that at the melting point of indium (156°C) the solder turns into a mixture of liquid phase

indium with AuIn_2 grains [67]. Using a lower solder temperature might not completely absorb the AuIn_2 layer into the indium matrix, so that the solder junction quality is degraded. On the other hand, a longer process or a higher temperature might solve the platinum layer, allowing the indium to get in contact with the semiconductor.

At this stage, successful soldering can be recognized by droplets of indium pressed out of the solder junction and by a continuous rim around the dice of dissolved indium in the gold coating of the submount (seen only under a microscope).

3.4.2 Etching

After soldering, the structure is mechanically supported by the submount and we can remove the substrate. To leave the structure intact and to achieve a high quality surface, etch stop layers are incorporated in the design and a multi-step selective etch process is used. Typically we use three etchstop layers with 300 nm $\text{Al}_{0.85}\text{Ga}_{0.15}\text{As}$, 20 nm GaAs and 70 nm AlAs. It is most convenient to use thin wafers (200 μm) but chemo-mechanical polishing with bromine or lapping can be used to reduce the thickness of the sample to 100 - 150 μm instead.

The remaining substrate is removed by wet etching under a jet of $\text{H}_2\text{O}_2:\text{NH}_4\text{OH}$ stopping at the $\text{Al}_{0.85}\text{Ga}_{0.15}\text{As}$ layer with a selectivity up to 30 [68]. Wax is used to protect the solder junction and the submount during etching. We use a mixture of $\text{H}_2\text{O}_2:\text{NH}_4\text{OH}$ with pH 8.6 resulting in a etch rate of 6 - 8 $\mu\text{m}/\text{min}$. The mechanism of etching can be described by the growth of an oxide film which cracks into small segments that float away from the surface, permitting new oxide to form [69]. The small gallium content in $\text{Al}_{0.85}\text{Ga}_{0.15}\text{As}$ makes this layer more stable against the etchant than pure AlAs. When the etchstop layer is reached, a color change can be observed. The exact colors depend on the reflectivity spectrum of the structure but since the AlGaAs etch stop layer makes the main contribution to the reflectivity in the visible a sequence of brown-purple-green-yellow-blue can be expected. Typically the etch rate is faster directly under the jet, resulting in colored ring patterns moving toward the edge of the sample.

With this first step the substrate is removed but to achieve a good surface quality three additional steps are needed. The AlGaAs is removed with hydrofluoric acid (HF) stopping on the 20 nm GaAs layer. The selectivity is excellent, allowing to stop with a flat surface. In Table 3 the etch rates are listed for different aluminum content in AlGaAs and for different concentrations of the hydrofluoric acid. Defects in GaAs are etched much faster than a perfect crystal and with anisotropy, resulting in rectangular holes when

exposing to the acid for a too long time. Because of the hazardousness of hydrofluoric acid we tested hydrochloric acid (HCl) as a replacement. However the selectivity is poorer and the attack of defects much more severe making it difficult to achieve a good surface.

Table 3. Etch rate of hydrofluoric acid for AlGaAs in nm/s. The last row gives the material composition where no attack by the etchant could be observed. (Measurements are performed by Siegfried Nau, University Marburg).

Material \ HF conc.	1.5%	10%	40%
AlAs	300	> 1000	
Al _{0.85} Ga _{0.15} As	40	200	
Al _{0.7} Ga _{0.3} As	5	30	200
Al _{0.5} Ga _{0.5} As			8
Rate \approx 0 nm/s	Al _{0.63} Ga _{0.37} As	Al _{0.55} Ga _{0.45} As	Al _{0.4} Ga _{0.6} As

H₂O₂:NH₄OH at pH 7.05 is used to remove the 20 nm GaAs layer. The etch rate is 25 – 55 nm/min for slight agitation by hand. The final 70 nm AlAs etchstop layer is removed by another dip in the hydrofluoric acid.

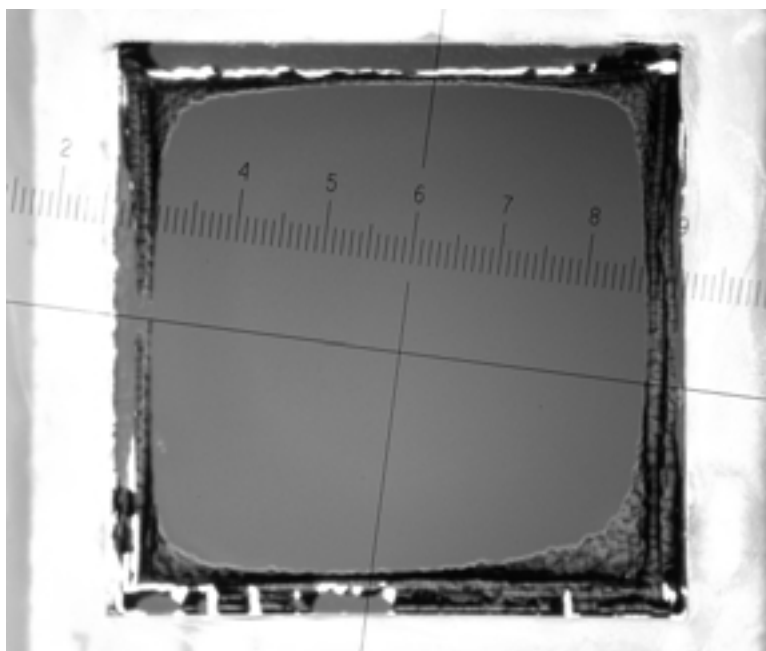


Figure 31. Gain structure after etching. A rim of GaAs substrate remains on the device. Some indium droplets shine through the wax on the side. (Sample R3350 4b)

To remove the wax, trichloroethylene is used with rinsing in acetone, methanol and water. During jet etching some particles stick to the wax. Care must be taken that they are carried away from the device while solving the wax. Usually a rim of substrate remains on the device leaving an open surface of 3 mm x 3 mm for a soldered dice of 4 mm x 4 mm (Figure 31).

3.5 Characterization

With the methods discussed for the calibration of the growth rate (Section 3.2) the precision of the growth can be measured. Additionally in this Section we describe methods to determine the quality of the surface and of the quantum wells.

3.5.1 Dark line defects (photoluminescence microscopy)

The quality of the crystalline structure in the quantum wells is important for both the quantum efficiency of the radiative decay and for the degradation of the device [70, 71]. Several methods have been employed to study misfit dislocations, including transmission electron microscopy, low-temperature photoluminescence spectroscopy, cathodoluminescence spectroscopy, X-ray diffraction, Nomarski contrast microscopy and photoluminescence microscopy. Some techniques as X-ray diffraction and photoluminescence spectroscopy are known to underestimate defects unless used with a very high resolution [63, 72]. We use photoluminescence microscopy because of its non-destructive nature and experimental simplicity.

Matthews and Blackeslee derived a model for the formation of dislocation when growing a crystal layer on a host crystal with different lattice constant [73]. It is based on a thermodynamic model balancing the energy needed for a defect state in the crystal and the energy needed for the compression of the strained layer. The conclusion is that misfits can be accommodated by uniform elastic strain until a critical layer thickness. Thereafter, it is energetically favorable for misfit to be shared between dislocations and strain. For a single InGaAs quantum well on GaAs with the defects characteristics observed for this material the critical layer thickness is

$$h_c = \frac{11}{32\sqrt{2}\pi} \frac{a}{f} \ln\left(\frac{\sqrt{2} h_c}{a} + 1\right) \quad (21)$$

with a the lattice constant and $f = \Delta a/a$ the misfit (Δa is the difference of lattice constant for layer and substrate).

For multiple quantum wells the theoretical and experimental basis is weaker. Investigations of the critical layer thickness for InGaAs quantum wells with different spacer layers lead to the assumption that a structure is under-critical as long as every part of it is below critical layer thickness calculated with the misfit deduced from a weighted average [63]. Note that the critical layer thickness can be enlarged to a certain extent with some epitaxial ‘tricks’ (e.g. precompensation of compressive strain with a tensile strained layer or growth at lower temperatures to get away from thermodynamic equilibrium).

To study the dark line defects in our structures we set up a photoluminescence microscope. A microscope objective is used to image the sample on a CCD camera. Excitation is achieved with the relative homogeneous beam of a fiber-coupled laser diode. Low-pass filters are used to suppress scattered pump light. The resolution of the setup is $\approx 10 \mu\text{m}$.

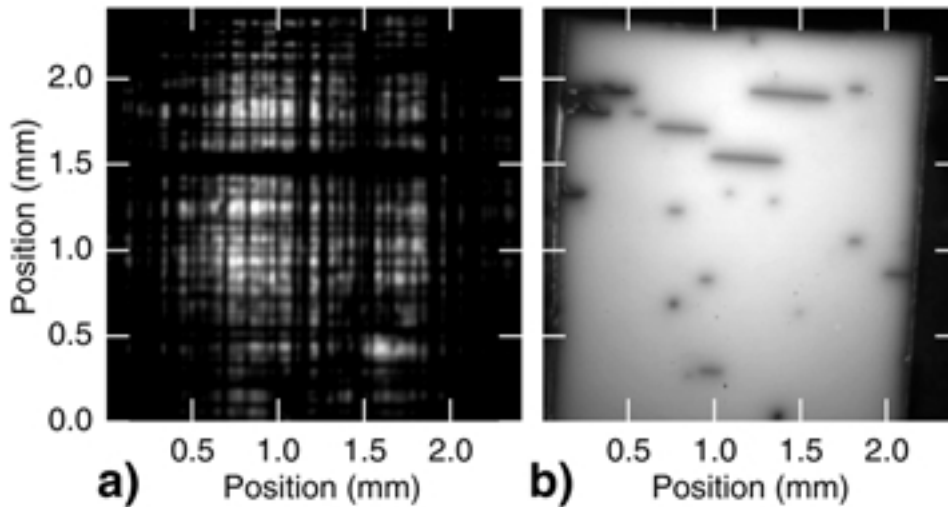


Figure 32. Photoluminescence micrograph of gain structures with and without strain compensation. Structures with (a) nine quantum wells grouped within three antinodes of the standing wave pattern and (b) with twelve quantum wells with GaAsP strain compensation layers are shown. (Samples R3166 1b and QT1462)

In Figure 32 the effect of strain compensation is illustrated. The structure in Figure 32 a) contains nine 8-nm $\text{In}_{0.15}\text{Ga}_{0.85}\text{As}$ quantum wells grouped in three antinodes of the standing-wave pattern. Even though the single quantum wells are well below critical layer

thickness, the accumulation of the strain leads to the dark line defects along [100] directions. By inclusion of layers with strain of opposite sign the total strain can be balanced. Figure 32 b) shows a structure with even twelve quantum wells and higher indium content ($\approx 22\%$) but with strain compensation by GaAsP layers. Strain compensation is not yet perfect but the defects are much less dense and large spots without defects can be selected.

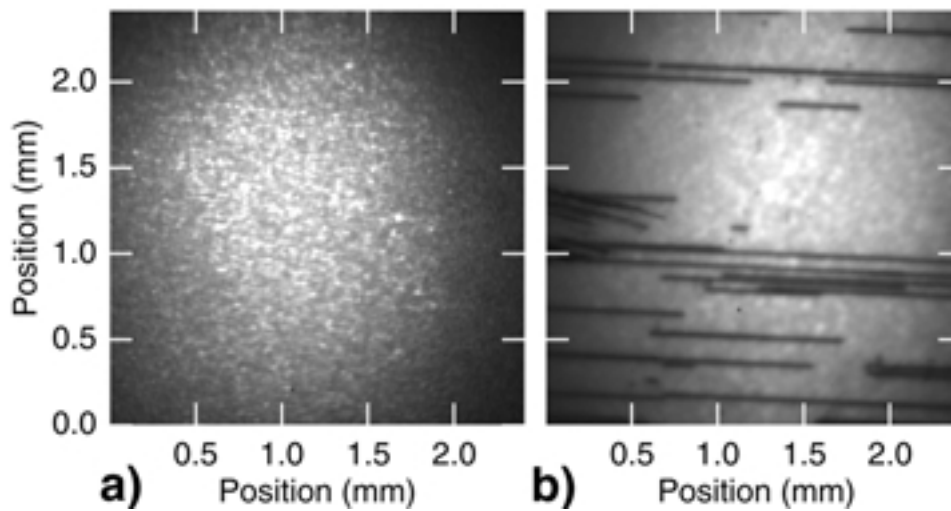


Figure 33. Photoluminescence micrograph with and without mirror. a) Test structure with seven quantum wells. b) Same quantum well sequence but on a Bragg mirror with 29 pairs. (Samples R3315 and R3324)

It is important to note that AlAs with its low misfit on GaAs also contributes to the strain accumulation. In Figure 33 the same quantum well sequence is depicted once just with a thin AlAs layer for carrier confinement (a) and once on a Bragg mirror including $\approx 2.5 \mu\text{m}$ AlAs (b). The seven quantum wells are 8 nm thick with 15% indium spaced by 125 nm GaAs. The sprinkles are mostly due to a residual inhomogeneity in the pump light.

3.5.2 Surface quality (atomic force microscopy)

For the characterization of the surface an atomic force microscope is used.

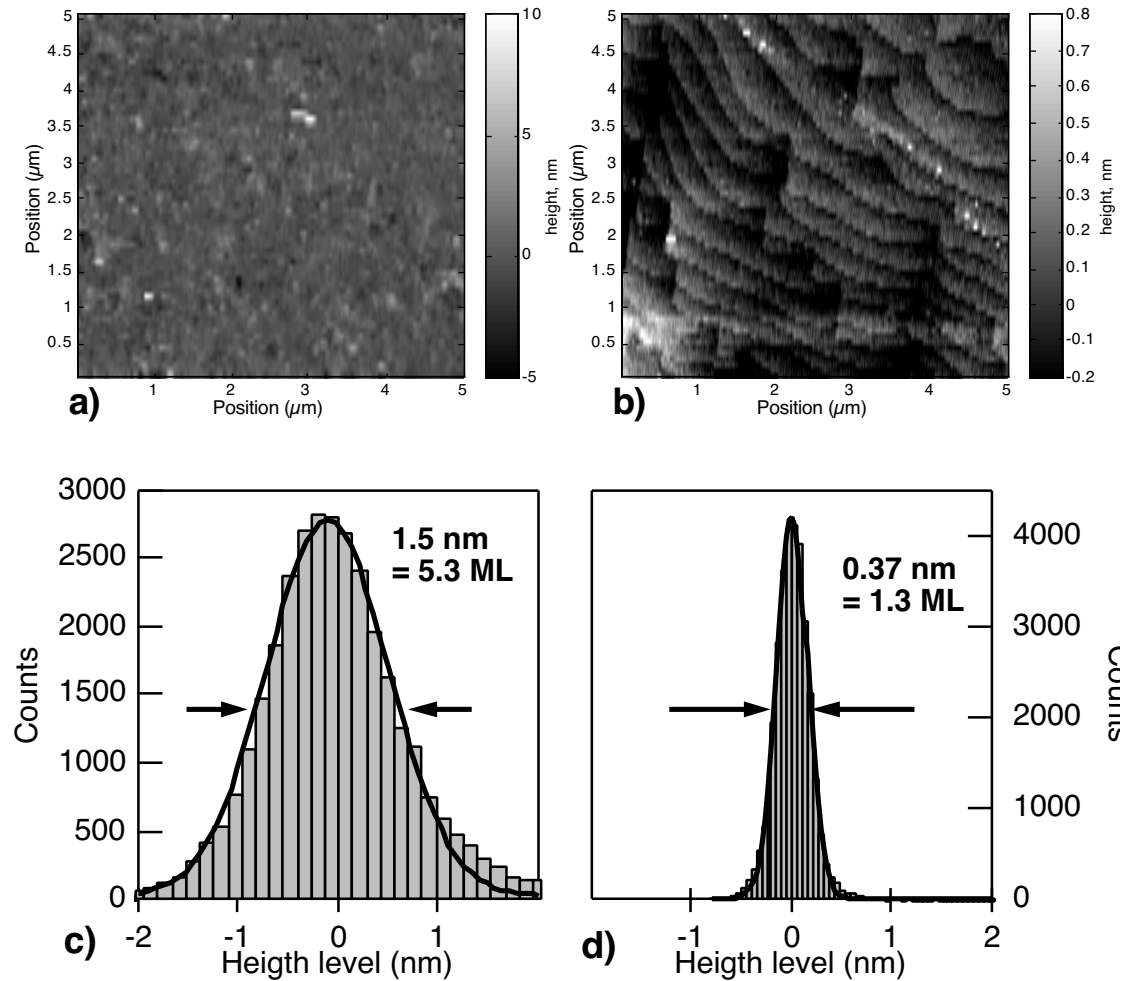


Figure 34. Comparison of surface quality. A $5\ \mu\text{m} \times 5\ \mu\text{m}$ AFM scan of an epitaxial lift-off structure (a) and of a structure remaining on the substrate (b) is shown. Statistics on the heights level of the two scans reveals a roughness of five monolayers for the processed surface (c) and one monolayer for the surface directly from the MOCVD growth. (Samples R3166 and R3238)

In Figure 34 the surface from a processed sample is compared with a surface directly after MOCVD growth. On the surface of a gain structure without processing we can clearly resolve the atomic layers (Figure 34 b) and a statistic of the height levels measured in this

scan reveals a variation of only 0.37 nm or 1.3 monolayers (Figure 34 d). The epitaxial lift-off described in Section 3.4 gives a smooth surface with full-width at half-maximum variation of the thickness of the last layer of 1.5 nm or 5 monolayers (Figure 34 a and c). Seven additional scans on different spots of the sample always gave similar results. Interrupting the growth between AlAs and GaAs layer might make the interface more abrupt and improve the processed surface further. However, scattering losses do not seem to impair the performance of the device.

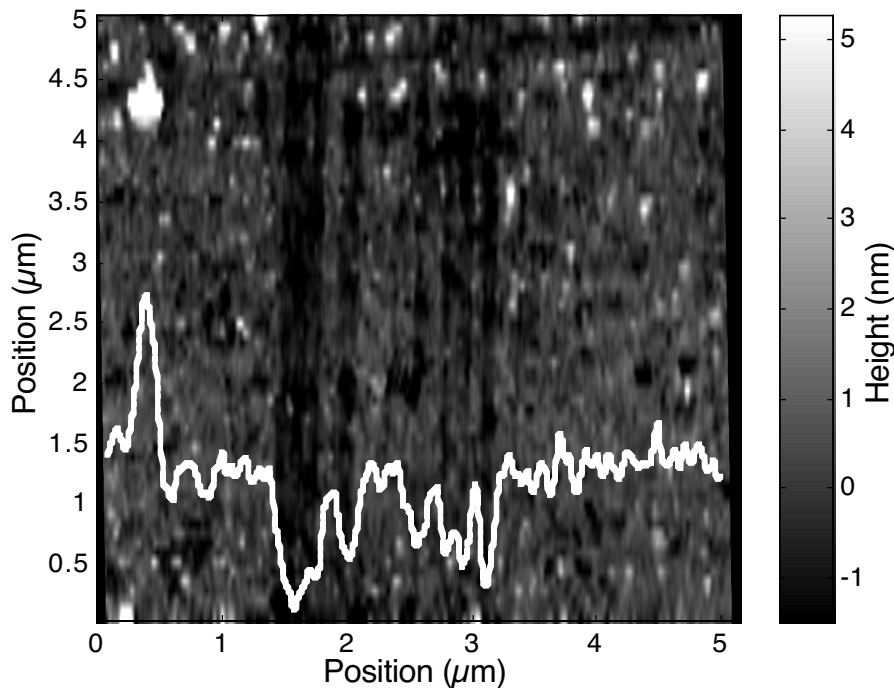


Figure 35. Effect of cleaning a GaAs surface with a lens tissue. The white line is an average of the heights over the picture in one direction. Scratches with ≈ 1.5 nm depth can be seen. (Sample R3166)

Using a device in the laboratory often results in some contamination of the surface by dust. We investigated the effect of mechanical cleaning of a GaAs surface with a lens cleaning tissue and acetone. Figure 35 shows the scratches with ≈ 1.5 nm depth over the sample. Experience has shown that cleaning a dusty surface improves the laser performance but it must be kept in mind that the semiconductor structure will be affected and especially structures with only a thin cap layer protecting a AlAs layer from oxidation might be damaged.

3.5.3 Degradation

A concern is the degradation of the gain structures during laser operation. Two mechanisms are mainly suspected and are investigated: i) Dark line defects incorporated during growth are known to lead to degradation [70, 71], ii) The GaAs cap layer can experience enhanced oxidation when optical excited [74, 75, 76]. Note that both mechanisms can basically be avoided by replacement with different materials: growing the structure below critical layer thickness (e.g. using strain compensation layers) will avoid the dark line defects and an InGaP layer grown lattice matched on GaAs allows to have a transparent, non-oxidizing layer at the semiconductor / air interface.

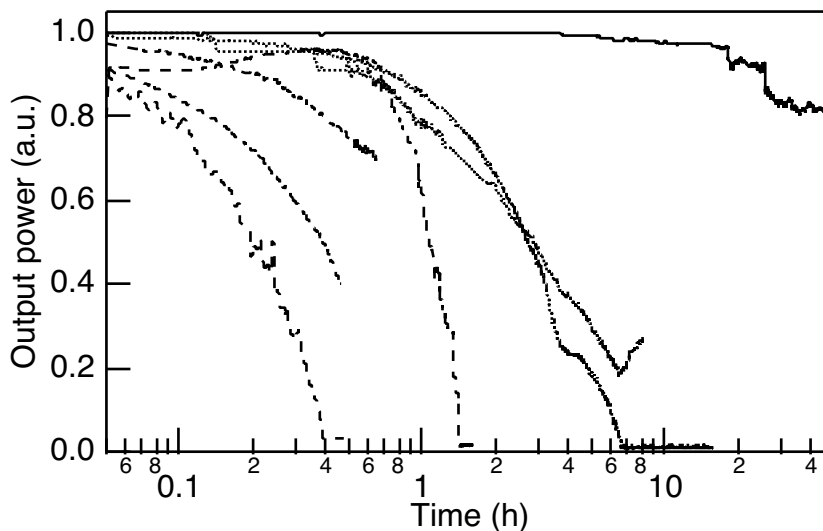


Figure 36. Degradation of gain structures. The output power drop is measured relative to the power at start. The structure with nine quantum wells shows the fastest degradation (dashed). A structure with five quantum wells lasts for about 10 h to complete failure (dotted) and a sample with strain compensation operates significantly longer (solid). (Samples R3166, R3350 and QT1462)

To characterize the degradation we observe the output power over a longer period with fixed pump power. Influence of the heat sink temperature, the ambient gas (air or dry nitrogen), the pump power and the laser power are investigated. The laser power and the ambient gas do not show any influence on the degradation. A slightly faster decay is observed with a raised heat sink temperature and a clear dependence on the pump power is seen. As it is symptomatic for a damage mechanism the variations in data are large and the temporal evolution varies from a smooth nearly linear decrease to step like instantaneous

power drops. Care must be taken for longer measurement when the ambient temperature is reduced over night: Especially cavities close to the stability limit suffer considerable losses by misalignment when the cavity mounts change temperature. We might observe power recovery in the morning when the room is heated again. All measurements are tested for improved performance with realignment after degradation but not more than $\approx 10\%$ of the original power could be recovered, indicating that the major power drop is due to degradation of the structure.

In Figure 36 we compare degradation of different structures. The first structures we achieved with high power performance lasted for only about an hour to complete failure (Figure 36, dashed lines). A structure with a reduced number of quantum wells (five instead of nine) has a significantly longer life-time with ≈ 10 h to complete failure (dotted). With a sample with GaAsP strain compensation layers (with a low density of dark line defects as seen in Figure 32 a) only a slight degradation after 10 h was observed and after 50 h still more than 80% of the original power was achieved. (This sample was kindly provided by Arnaud Garnache, University of Southampton, GB).

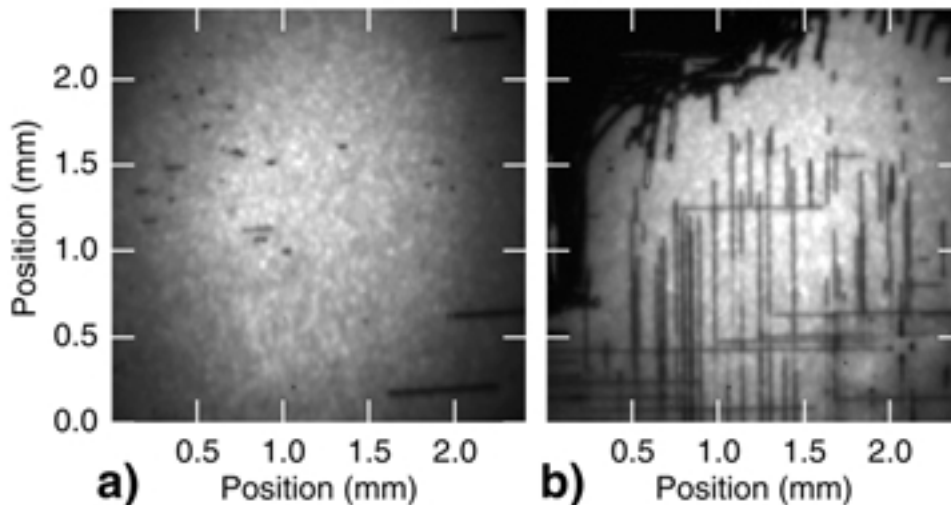


Figure 37. Growth of dark line defects. a) and b) are photoluminescence micrographs from the same sample. a) is taken directly after processing of the device while b) is about one month later and after many hours used in the laser. (Sample R3350 4b)

A further indication for degradation caused by dark line defects are the micrographs shown in Figure 37. A gain structure with five quantum wells shows only a few dark line defects directly after soldering and substrate removal (a). After extensive use in the laser

the dark line defects have grown and multiplied (b). However, the absence of well defined spots where the pump light was applied is not understood.

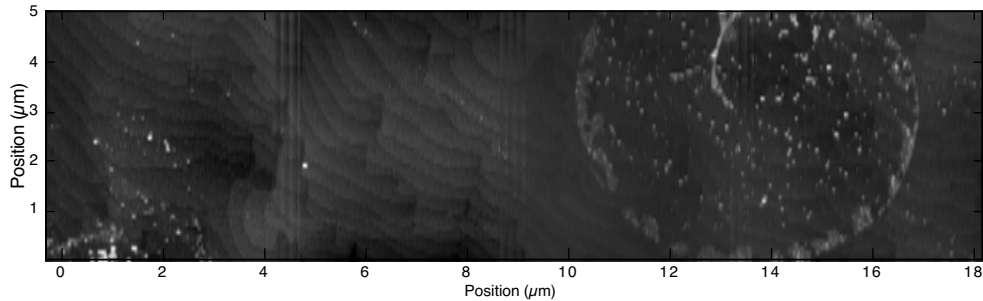


Figure 38. AFM investigation of the surface after lasing. A device was scanned after exposure to the pump light for 1.3 hours resulting in a drop of output power of 33%. The atomic layers can be seen but no sign of oxidation or other damage. (The circle is expected to be a dried droplet, not a defect of the crystal) (Sample R3238)

To investigate a possible oxidation of the GaAs cap layer we use the atomic force microscope to scan the surface after exposure to the pump light. To mark the laser spot on the sample, we run the laser with a heat sink temperature below dew point to let the water precipitate on the surface (normally suppressed with dry nitrogen). This results in well visible dirt particles on the surface of ≈ 100 nm height when the water has dried. The pump laser heats the surrounding of the pump spot above dew point leaving a clear spot in the contaminated surface. In Figure 38 a scan over the center of the spot is shown (actually five scans are concatenated to give a single image). Oxidation would be expected to destroy the crystalline structure. That is not the case as seen in form of the monolayer steps at the surface indicating that the cap layer is not affected by exposure to the pump light in the range of 1 h. The circle like feature is expected to be due to a droplet dried on the surface. It is 60 times smaller than a typical grains used to mark the laser spot.

We conclude that dark line defects incorporated by growing the structure over critical thickness is most likely to be the cause of the performance degradation. Oxidation of the cap layer is shown to have little or no influence. Improved designs with strain-balancing GaAsP layers will increase both lifetime and efficiency of the devices.

CHAPTER 4

Mode locking of Vertical-External-Cavity Surface-Emitting Lasers

A major limitation of conventional mode-locked semiconductor lasers is the relatively low average output power of typically only a few milliwatts average power. Pulsed laser sources with multi-GHz repetition rates and high average powers (≈ 1 W) are required for applications like commercial printing, display systems using single pass frequency conversion or optical clocking of integrated circuits. Edge-emitting semiconductor lasers have been passively mode-locked [77] and ultra-short pulses [78, 79, 80] and extremely high repetition rates [7] have been reported. Techniques to increase average power while maintaining a single lateral mode include flared waveguides [47], compound lasers with a tapered semiconductor amplifier section [48] and master-oscillator-power-amplifier systems with tapered [49] and inverse bow-tie amplifier geometry [50] resulting in average powers up to 400 mW.

A solution for semiconductor oscillators with higher average powers is provided with optically pumped vertical-external-cavity surface-emitting lasers (VECSELs) [16, 17]. Pulsed operation of vertical cavity devices has been reported with synchronous pumping [81, 82] and with active mode locking [83]. To achieve short pulses with continuous-wave pumping we investigate passive mode locking with a semiconductor saturable absorber mirror (SESAM [8, 9, 10]) in the external cavity.

Previously, SESAMs have been extensively used to mode-lock diode-pumped lasers with ion-doped crystals and glasses as gain media. These solid-state lasers used to be the only sources able to achieve mode locking with average powers at the watt level, and indeed even >10 W have recently been achieved [84, 85, 86]. Tremendous progress was also

made in terms of pushing the repetition rate to gigahertz levels, and 77 GHz have been reported with a Nd:YVO₄ laser, although at lower powers of 65 mW [87].

Optically pumped VECSELS offer a number of advantages over those solid-state lasers: The relatively small gain cross-sections of the active ions used in crystals and glasses lead to a tendency for Q-switching instabilities [88]. They become more severe for higher repetition rates, for high average power and for gain materials supporting short pulses. In contrast, with a quantum well gain structure Q-switching instabilities are eliminated by the large gain cross-section despite the large gain bandwidth of ≈ 30 nm, sufficient to support sub-picosecond pulses. Moreover, the variety of semiconductor materials and their ability for continuous tuning of the band gap with ternary and quaternary compounds allows a great freedom in the selection of pumping and lasing wavelengths. We can build on the sophisticated semiconductor technology, which achieved a mature level in the last decade and is driven by the commercial interest greatly stimulated by the mass producibility in wafer technology.

In this Chapter we record three steps in the development of a high power mode-locked VECSEL after giving a short review of the basic mechanisms of passive mode locking (Section 4.1). In Section 4.2 we describe the first realization of a passively mode-locked VECSEL. The gain structure of this first device is not specifically designed for mode locking and disturbing interferences affected the stability of the mode-locking. A device with an enlarged free spectral range is presented in Section 4.3. Epitaxial lift-off structures are used for a low thermal impedance, allowing high power performance and to fully suppress back coupling from the wafer back side. Mode locking of such a device is described in Section 4.4.

4.1 Mode locking mechanisms

Mode locking – the generation of ultrashort laser pulses – can be described in the frequency domain or in the time domain. The expression "mode locking" stems from the frequency domain: The longitudinal modes of the laser cavity build an equally spaced comb with $\Delta f = \frac{1}{2} c / L_{\text{opt}}$, with c being the speed of light and L_{opt} the optical cavity length. To achieve pulses the phase between the modes must be 'locked'. However, despite the name, the principle can be understood more easily in the time domain: A light pulse circulating in the cavity generates a periodic output behind a semitransparent mirror. The

phase condition in the frequency domain can simply be derived by Fourier transformation of this pulse train. That means for mode locking we need to form a pulse shorter than the cavity round-trip time and stabilize this mode of operation against competing states like continuous-wave operation or Q-switching. Most commonly this is achieved with either a periodic modulation of the loss or of the gain. It can be achieved actively (e.g. with an acousto-optic modulator or by modulating the current in a laser diode), or passively with a saturable absorber. Apart from additional electronics needed, active mode locking leads typically to relatively long pulses of several tens of picoseconds. Therefore, we limit ourselves to passive mechanisms.

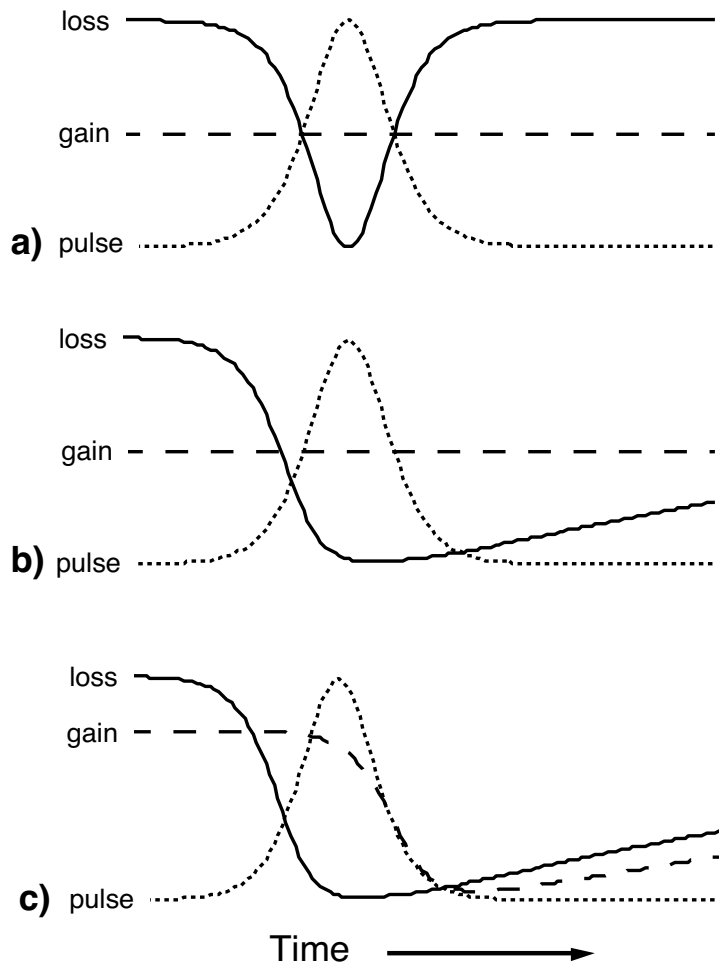


Figure 39. Three fundamental mechanisms of passive mode locking: a) fast saturable absorber mode locking, b) slow saturable absorber mode locking, and c) mode locking with slow saturable absorber with dynamic gain saturation

Mode locking a laser usually implies that there exists only a short time window during a cavity round-trip, in which the net gain is positive (see Figure 39). There are three different ways to achieve the pulse formation, depending on the gain and absorber properties: Fast saturable absorber mode locking [89, 90], mode locking with a slow saturable absorber and additional pulse shaping processes (e.g. pulse delay by the absorber or soliton mode locking) [91, 92, 93, 94, 95], and slow saturable absorber mode locking with dynamic gain saturation [96, 97].

For lasers based on gain materials with ion-doped crystals and glasses, the saturation energy of the gain is large compared to typical intracavity pulse energies, due to the relatively small laser cross-sections. Therefore, the gain is saturated to a constant level by the average intracavity intensity and no dynamic gain saturation can take place. A solid-state laser can be mode-locked by a fast saturable absorber (Figure 39 a) or by a slow saturable absorber and pulse shaping mechanisms like soliton formation (Figure 39 b).

The fast saturable absorber can follow the pulse shape, which leads to the short net gain window. Pulse shaping is achieved with the amplitude modulation of the time dependent gain and loss. Additive pulse mode-locked (APM) lasers [98, 99, 100] were the first ones to use a fast saturable absorber. However, APM and a number of other fast saturable absorbers require critical cavity length stabilization or introduce very high losses. The first simple and reliable technique was Kerr lens mode locking (KLM) [101]. KLM makes use of the nonlinear Kerr effect for self-focusing. The gain window can be opened by an intracavity aperture affecting the high intensity pulse with the additional Kerr lens less than the continuum [102, 103, 104]. Alternatively, the Kerr lens can be used to improve the mode overlap of the pump laser with oscillating modes in the gain element [41, 105]. The time constant of the nonlinear refractive index is very fast, leading to the shortest pulses ever obtained directly out of an oscillator [1, 106, 107]. The disadvantages of KLM is its low tendency for self starting and a limited applicability for diode-pumped lasers because of a weak Kerr lens when using a large pump mode.

KLM is also referred to as artificial saturable absorber: Even though it behaves in many aspects like an absorber there are no states to be saturated as for example in a semiconductor absorber. A consequence is a dependence of the shaping strength on the intensity instead of the fluence as in real absorbers. Real saturable absorber have typically a much longer recovery times than the desired pulse duration. However it was observed that the optical pulses can be significantly shorter than the recovery time of the absorber. To understand why the pulse can be shorter than the net gain window, one must consider additional pulse shaping mechanisms. Note that this does not mean, that an additional

optical element is required. In some configurations (as discussed below) the pulse shaping can be explained by the time dependent absorption while others use a modulation of the temporal and spectral phase.

Such an effect is studied in detail in Ref. [95] and can be described as follows: When a pulse impinges on the absorber, the leading edge sustains more losses than the trailing part of the pulse where the absorber is already bleached. This leads to a steady delay of the pulse. Though any signal in the net gain window behind the pulse is amplified, it is not delayed and eventually it gets wiped up by the delayed pulse. The net gain window can be more than 20 times longer than the pulse until mode locking becomes instable. The effect is relatively sensitive to phase effects like self phase modulation (SPM).

To achieve short pulses with a slow saturable absorber and large SPM, the pulse shaping must be controlled by compensation of the chirp with group delay dispersion (GDD). The pulse can then be treated as a soliton and the mechanism is called soliton mode locking [91, 92, 108]. A qualitative understanding can be obtained by considering a short soliton pulse and a weaker long ‘continuum’ (e.g. a pulse as long as the net gain window) simultaneously in the cavity. The continuum has a narrower bandwidth and hence experiences a higher net gain. However, because of the low intensity of the continuum SPM is much weaker and does not compensate for the GDD adjusted for the soliton. Therefore the ‘continuum’ pulse spreads in time and the saturable absorber is used to reduce the portions of the continuum leaving the net gain window.

For semiconductor lasers (and dye lasers), the saturation energy of the gain is still larger but in the same range to the one of the loss. A short net gain window is obtained with the contribution of dynamic gain saturation (Figure 39 c) [96, 97].

For a general understanding, we can consider a pulse with an energy in the range of the saturation energy of the gain. The absorber is expected to have a significantly smaller saturation energy. That means the absorber is completely bleached already when a small portion of the pulse has passed. Since the gain is then not yet saturated, a net gain window opens up. However, the pulse is strong enough to saturate the gain to an extent to achieve a net loss at the trailing edge of the pulse. It is important to note, that in this case the pulse duration is not dependent on the absorber dynamics but depends on the pulse energy and on New’s saturation parameter s [96] ($s = E_{\text{sat, L}}/E_{\text{sat, A}}$, with $E_{\text{sat, A}}$ and $E_{\text{sat, L}}$ being the saturation energies of the absorber and gain, respectively). In the approximation of a relatively low saturation of the gain and good saturation of the absorber, the pulse width varies inversely with the pulse energy and proportional to the root of $s - 1$ [97].

Also in the case of a dynamic saturation of the gain, phase effects might influence the pulse shaping. Martinez et al. [94] describes a pulse formation mechanism based on an interplay of group delay dispersion and a time dependent refractive index change due to the saturation of gain and absorber during pulse propagation for dye lasers. Some findings are reminiscent of solitons: GDD influences the pulse duration and two regimes with opposite sign of GDD show either strongly chirped or nearly chirp free pulses. However, since the antagonist of the GDD is not SPM but the refractive index change caused by the gain saturation (as understood with Kramers-Krönig relation) there are distinctions: The physical difference is the dependence of SPM on the intensity while the gain saturation is proportional to the pulse fluence. The resulting dependence of the pulse duration is proportional to the root of the GDD (in contrast to a linear dependence for solitons).

The parameters found in mode-locked VECSELs resemble in many aspects dye lasers. Mode locking is obtained in both cases with a slow saturable absorber and with dynamic gain saturation. Moreover the refractive index change due to carrier excitation is found to be rather large in semiconductor lasers. An analysis of the application of this mechanism on mode-locked VECSELs will be published in Reference [109]. Special importance will be attached to the possibility to achieve quasi-solitons with a low chirp and a short pulse duration.

4.2 First demonstration

For the first demonstration of a passively mode-locked VECSEL [110, 111] we use a structure grown according to the specification given in Ref. [16] but without epitaxial lift-off. It consists of an array of 12 compressively-strained $\text{In}_{0.2}\text{Ga}_{0.8}\text{As}$ quantum wells between $\text{GaAs}_{0.94}\text{P}_{0.06}$ tensile-strained barriers, of thickness adjusted to balance the net strain in the structure to zero. The quantum wells are spaced by GaAs layers to intervals of $\lambda/2$. Underneath the multiple quantum well section lies a 27-repeat $\text{AlAs}/\text{Al}_{0.1}\text{Ga}_{0.9}\text{As}$ Bragg mirror. A window layer of 450-nm thick $\text{Al}_{0.43}\text{Ga}_{0.57}\text{As}$ is grown over the multiple quantum well section to keep carriers away from the surface, and this is finished with a capping layer of 10 nm of GaAs. Platelets approximately 5 mm square are cleaved from this wafer, lapped and polished to reduce the GaAs substrate to a thickness of $\approx 200 \mu\text{m}$, and attached to a copper heat sink using indium. The spectrum of photoluminescence emitted from a cleaved platelet edge show a strong peak at $\approx 980 \text{ nm}$. Platelets exhibit

lasing at wavelengths over the range 1000 – 1040 nm, governed by the temperature of the pumped surface, and also by variation in layer thickness across the wafer.

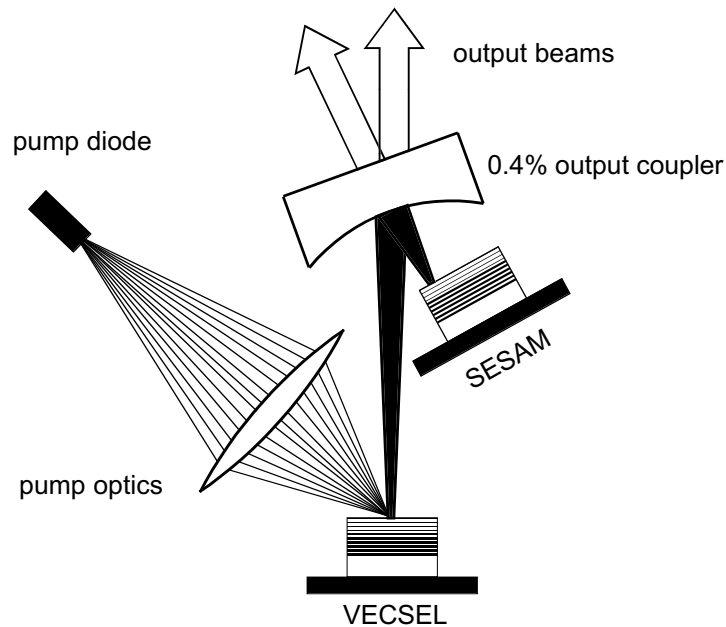


Figure 40. Setup of the laser. A gain structure is optically pumped with a diode laser emitting at 810 nm. With a curved mirror the laser mode is focused tightly on a SESAM. The output is divided equally between two beams.

The cavity setup is shown in Figure 40. A 2-W broad stripe diode laser emitting at 810 nm is used to pump the VECSEL continuously in a region of dimensions $90 \times 90 \mu\text{m}^2$ on the surface of the gain structure. The sample absorbs 60% of the incident pump power. The optically pumped wafer and the SESAM form the cavity end mirrors, and a spherical output coupler mirror, with radius 10 mm and transmission 0.4% at the laser wavelength, was used to fold the cavity.

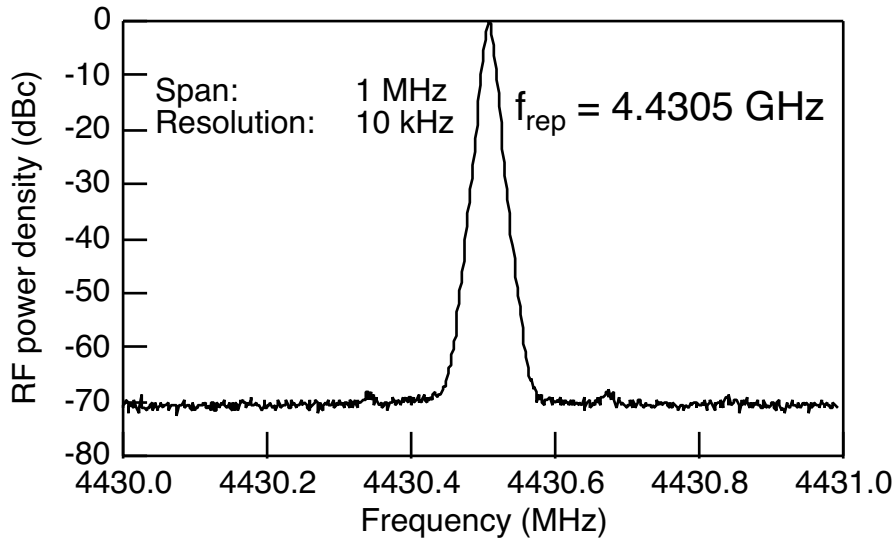


Figure 41. Radio frequency spectrum of the VECSEL output showing mode locking without Q -switching instabilities at a repetition rate of 4.43 GHz. The signal was obtained with a 50-GHz photodiode and a 26-GHz amplifier and spectrum analyzer.

The SESAM used in this laser consists of an AlAs/GaAs Bragg mirror with 25 layer pairs and a low-finesse anti-resonant $\lambda/2$ cavity incorporating a single 20 nm thick $\text{In}_{0.2}\text{Ga}_{0.8}\text{As}$ quantum well grown at low temperature (300°C) by molecular beam epitaxy (MBE). The low-intensity loss of the SESAM is 1.3%, and the bleaching response was bi-temporal, with a 130-fs fast component and a 4-ps recovery time. As shown in Figure 40, the V-cavity is made asymmetric, with cavity legs containing the SESAM and the gain wafer of length 6 mm and 28 mm respectively. The cavity mode is thus focused more tightly on the SESAM than on the gain wafer, with a ≈ 40 times smaller mode area. The absorber saturation energy is therefore sufficiently small relative to the gain saturation energy to ensure faster absorption saturation and strong pulse shaping.

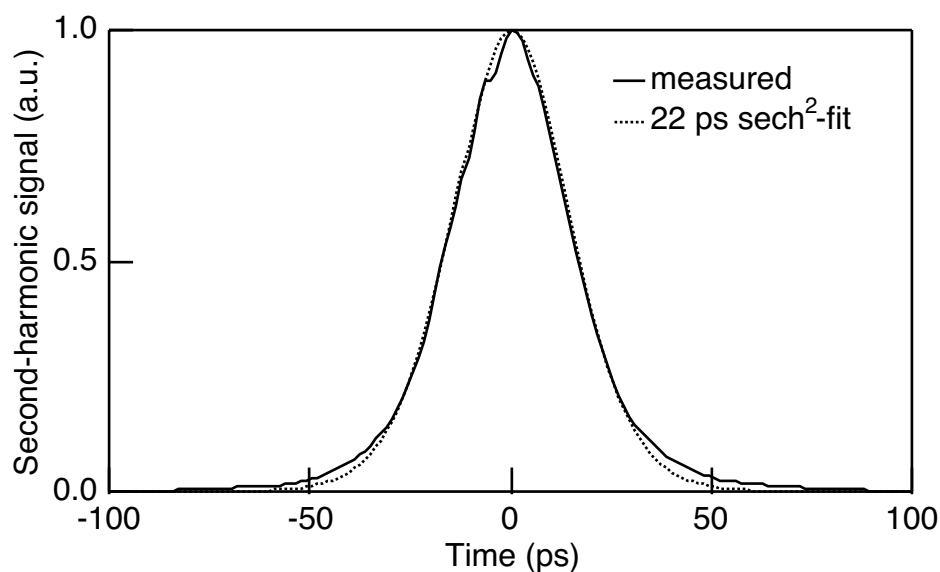


Figure 42. Autocorrelation trace of the mode-locked pulses (solid curve). The dashed line represents a fit to the data assuming a hyperbolic secant pulse profile with 22-ps FWHM.

With 1.4 W of pump power incident on the wafer the VECSEL emits a total power of 21.6 mW divided equally between two beams. Further increase of the pump causes the output power to decrease due to thermal effects. Figure 41 shows the fundamental peak observed in the radio-frequency spectrum of the photocurrent from a fast diode monitoring the laser output, corresponding to the cavity round-trip repetition rate of 4.43 GHz. The trace is free from sidebands down to the level of -70 dBc, demonstrating that the VECSEL exhibited stable, mode locking with no Q-switching instabilities. A measured pulse autocorrelation trace is shown in Figure 42 (solid curve), with a best fit assuming a hyperbolic secant pulse (dashed curve), for which the full-width at half maximum (FWHM) pulse duration is 22 ps.

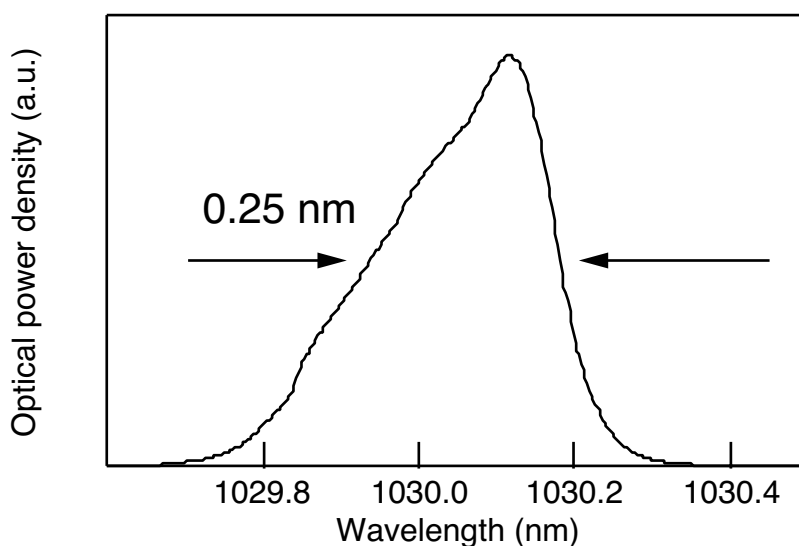


Figure 43. Optical spectrum of the pulse on a linear scale. The resolution of the optical spectrum analyzer is 0.1 nm.

Figure 43 shows the optical spectrum of the laser, with a bandwidth of 0.25 nm FWHM. The time-bandwidth product for these pulses is 1.5, indicating the presence of strong phase modulation effects. Unstable operation was observed when trying to obtain a larger bandwidth. We believed that is due to residual etalon effects in the gain structure.

In summary, we have demonstrated the first passively mode-locked surface-emitting semiconductor laser. The compact, all-semiconductor device generates 22-ps pulses with 21.6 mW average power at a repetition rate of > 4 GHz.

4.3 Improved laser with thinned structure

With the first device we noticed a limitation of the optical bandwidth to ≈ 0.3 nm. Also lasing with two spectral components spaced by ≈ 0.85 nm was observed, making the pulse formation unstable. We suspected this bandwidth limitation to be due to an etalon formed by the Bragg mirror and the back surface of the GaAs substrate, which is attached to a copper mount with indium. To check this, we operated a laser with a gain structure grown on a back side polished substrate in continuous-wave mode with a high reflector instead of the output coupler. The resulting laser spectrum is strongly modulated with a spacing of 0.32 nm corresponding to the 420 μm substrate (see Figure 44). With chemo-mechanical

etching using bromine, the substrate is thinned to a thickness of $\approx 50 \mu\text{m}$. The corresponding free spectral range would be 2.7 nm. However, with etching, the back side has no longer a surface with optical quality and scratches are visible to the naked eye. One might expect to eliminate interfering effects with a such treated back side but modulations in the laser spectrum are still seen (dotted line in Figure 44). The modulations depends on the spot on the sample, but free spectral ranges in the order of 1 – 2 nm can clearly be much larger than without thinning of the substrate.

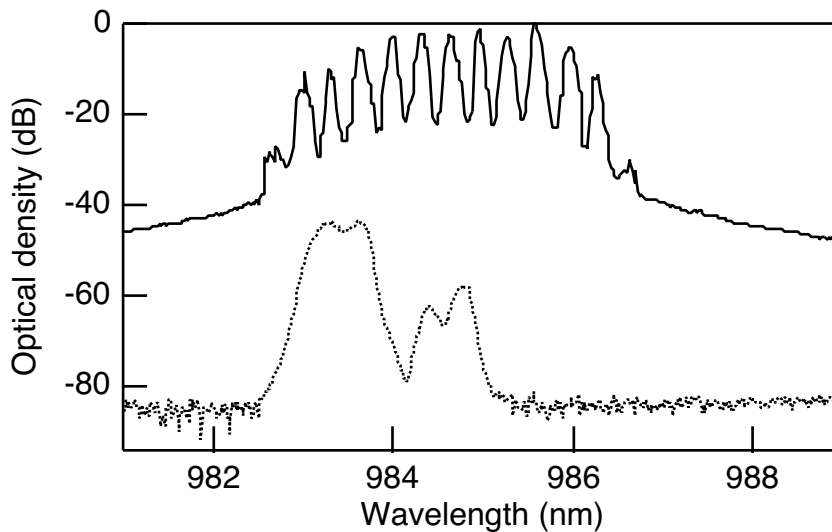


Figure 44. Optical spectrum revealing an etalon effect through the substrate. A continuous-wave laser with low losses shows a fringe pattern with a spacing of 0.32 nm for a structure on a backside polished wafer (solid) and a increased free spectral range for the wafer thinned to 50 μm .

We use this thinned sample for mode locking experiments [110, 112]. An additional advantage of the new device is an anti-reflective structure on top, applied for an increased saturation fluence, allowing the ratio between absorber saturation and gain saturation to be better (see Section 4.1). Note that the free spectral range of the etalon formed by the Bragg mirror and a Fresnel reflection at the top of the structure (as generated by the AlGaAs window in the first device) is much larger than the limiting fringes caused by the substrate. The active region contains three InGaAs quantum wells emitting around 980 nm grown with molecular beam epitaxy [113].

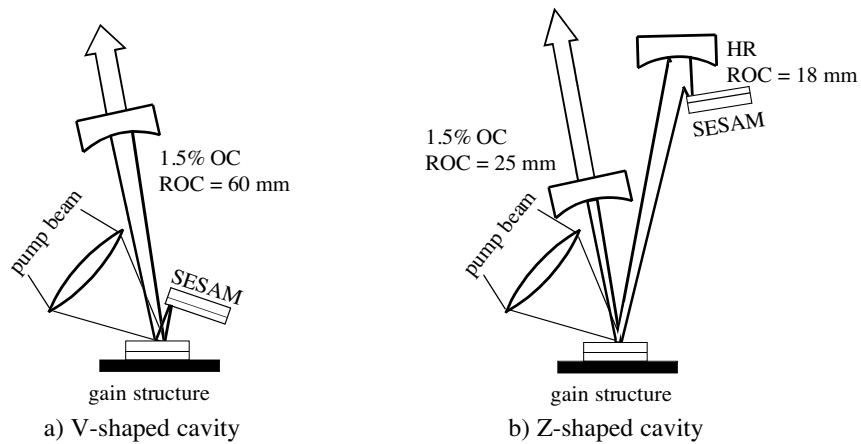


Figure 45. The laser setups. a) The V-shaped cavity allows to change the ratio of the laser mode areas on the gain medium and the SESAM. b) The Z-shaped cavity is uncritical aligned and gives cleaner pulses. HR = high reflector, OC = output coupler, ROC = radius of curvature, SESAM = semiconductor saturable absorber mirror.

First we set up the cavity shown in Figure 45 a). The 60 mm radius of curvature mirror gives a repetition rate of 2.5 GHz. This cavity allows to change the ratio of the mode sizes on the gain and absorber element by simply moving the two legs of the V-cavity while maintaining the total length. Indeed we see a dependence of the pulse duration on the ratio of the saturation energies.

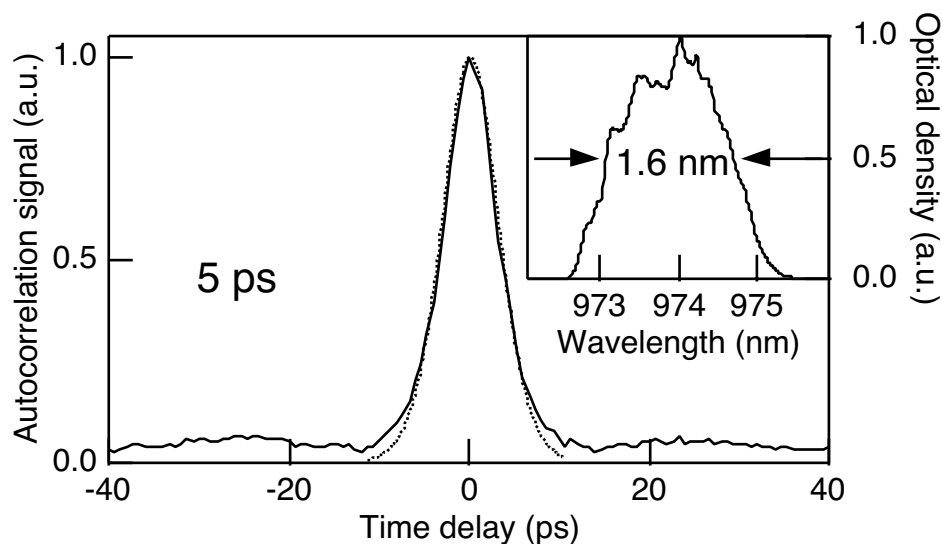


Figure 46. Autocorrelation and optical spectrum of thinned device with V-cavity.

The shortest pulse we could achieve is shown in Figure 46. The autocorrelation shows a 5 ps pulse assuming a sech^2 pulse shape. The optical spectrum is 1.6 nm wide indicating a strong chirp on the pulse. The ratio between the spot sizes on gain structure and SESAM is ≈ 60 , requiring a cavity alignment very close to the stability limit. We believe that this is the reason for a relatively low output power of 15.3 mW and for the noise level seen in the autocorrelation. Therefore, the cavity depicted in Figure 45 b) is tested, allowing a 30 times smaller spot on the SESAM than on the gain structure without critical alignment. It allows us to generate up to 40 mW with a cleaner spectrum, however with a longer pulse duration of 12 ps (Figure 47). The repetition rate is reduced to 1.8 GHz.

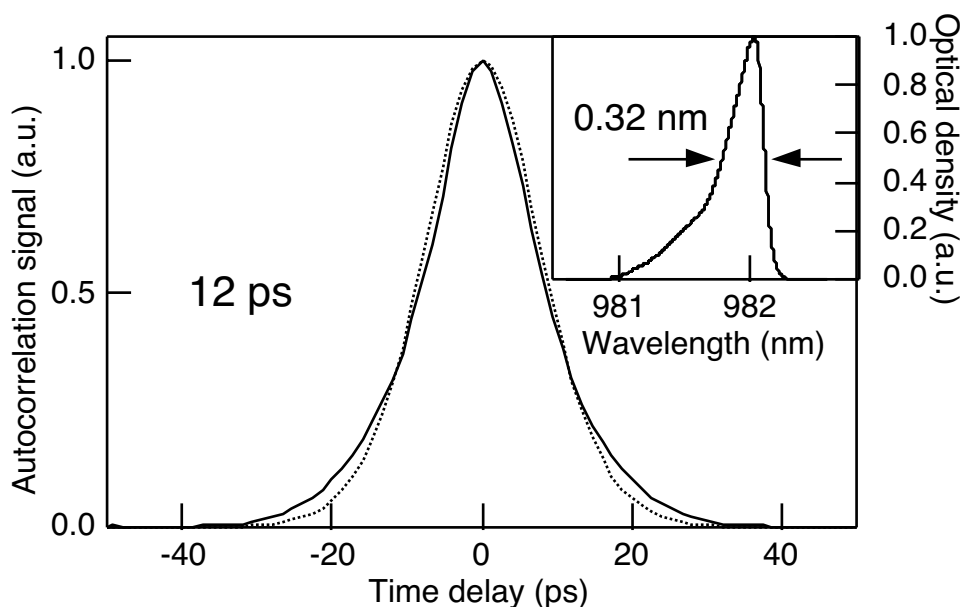


Figure 47. Autocorrelation and optical spectrum of thinned device with Z-cavity.

4.4 Mode locking with ELO structures

It became obvious that a complete cure of the etalon problem is needed to achieve undisturbed mode locking with a smooth gain spectrum. Also a lower thermal impedance would be highly desirable to achieve more output power (see Section 3.2). Angle polishing of the substrate might avoid the fringes in the gain spectrum but would not

improve the thermal impedance. A complete removal of the substrate seems to be the appropriate remedy. It is achieved by epitaxial lift-off (ELO) as described in detail in Chapter 3: First we grow the gain structure in reverse order on a GaAs substrate with intermediate etch-stop layers. We then solder the structure to a heat sink and finally remove the GaAs substrate by etching.

The first ELO structure includes a total of nine $\text{In}_{0.15}\text{Ga}_{0.85}\text{As}$ quantum wells with 8.2 nm well width distributed three-by-three in the anti-nodes of the standing wave pattern [114]. For the bottom mirror we use 7 pairs of GaAs/AlAs and 23 pairs of $\text{Al}_{0.2}\text{Ga}_{0.8}\text{As}/\text{AlAs}$ in a numerically optimized sequence to achieve 99.8% reflectivity for the laser wavelength (950 nm) and 98% reflectivity for the pump wavelength (805 nm) under 60° angle of incidence, allowing to double pass the pump light. The anti-reflective section has $< 1\%$ reflectivity for the laser wavelength under normal incidence and $\approx 20\%$ reflectivity for the pump wavelength under 60° angle of incidence. It contains $\text{Al}_{0.2}\text{Ga}_{0.8}\text{As}$ and AlAs layers apart from a 10 nm thick GaAs cap layer. The gain structure is grown with metal-organic chemical vapor deposition (MOCVD).

The mode-locked laser setup is the same as shown in Figure 45 b). The low thermal impedance allows to use up to 7.4 W of pump light from a fiber-coupled diode array emitting at 805 nm, focused to a spot with a diameter of $260 \mu\text{m}$ on the VECSEL. The heat sink is cooled with a Peltier element to -4°C , while dry N_2 prevents moisture to precipitate on the gain structure. The SESAM is of a low-finesse anti-resonant design consisting of a Bragg mirror with 25 pairs of GaAs/AlAs and a single quantum well absorber, embedded in a GaAs spacer layer of $\lambda/2$ thickness. The absorber is a low-temperature (350°C), 8 nm thick $\text{In}_{0.15}\text{Ga}_{0.85}\text{As}$ quantum well grown with molecular beam epitaxy (MBE). The beam diameter on the gain structure is $200 \mu\text{m}$ while it is significantly smaller ($18 \mu\text{m}$) on the SESAM. The output coupler has a transmission of 1.5%.

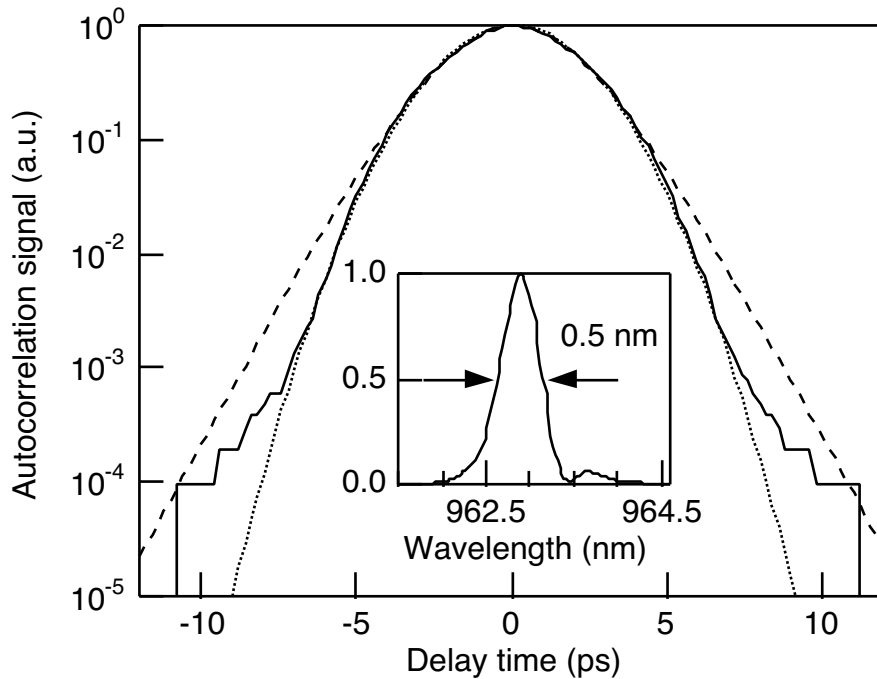


Figure 48. Autocorrelation of output pulse on logarithmic scale. The measured data (solid) are fitted assuming a Gaussian shaped pulse with 3.2 ps duration (dotted) or assuming a sech^2 shaped pulse with 2.8 ps duration. The inset plots the optical spectrum taken with a resolution of 0.1 nm.

A slowly scanning autocorrelator with lock-in amplification was used to measure the pulse shape (Figure 48). The autocorrelation was recorded for the maximum output power of 213 mW, showing that the pulses have a gaussian shape and are free of any pedestals down to -30 dBc. The optical bandwidth (Inset of Figure 48) is 0.5 nm, close to the transform limit for gaussian pulses (0.43 nm). The peak power is 30 W and the repetition rate is 2.06 GHz.

With photoluminescence microscopy we detected dark line defects in the gain structure. That might explain the low efficiency of $\approx 10\%$ for continuous-wave operation, and its observed degradation (see Section 3.5.3). A gain structure with a reduced number of quantum wells is tested: Five 8.5 nm $\text{In}_{0.15}\text{Ga}_{0.85}\text{As}$ quantum wells (QWs) placed in five anti-nodes of the standing wave pattern. The quantum well sequence grown without mirror structure are nearly free of dark line defects but when grown on the mirror photoluminescence microscopy reveals some defects (see Section 3.5.1). Consequently, we see degradation of the performance in the time range of 10 hours and strain

compensated structures will be needed to fully solve the problem. However, the slope efficiency could be improved up to $\approx 35\%$ for devices with a small mode area.

With the same cavity for mode locking the SESAM is damaged with a few hundred milliwatts output power. Therefore, we returned to the cavity shown in Figure 45 a) with a mirror with 25 mm radius of curvature resulting in a repetition rate of 6 GHz. (The problem with the alignment very close to the stability limit is relieved by a larger mode area on the gain structure.) With a pump spot with radii of $270\ \mu\text{m}$ and $350\ \mu\text{m}$, up to 18 W can be applied until roll-over is observed. The heat sink is stabilized at a temperature of 3°C . The most efficient pump absorption we find for an angle of 40° , where only 15% of the pump power is reflected.

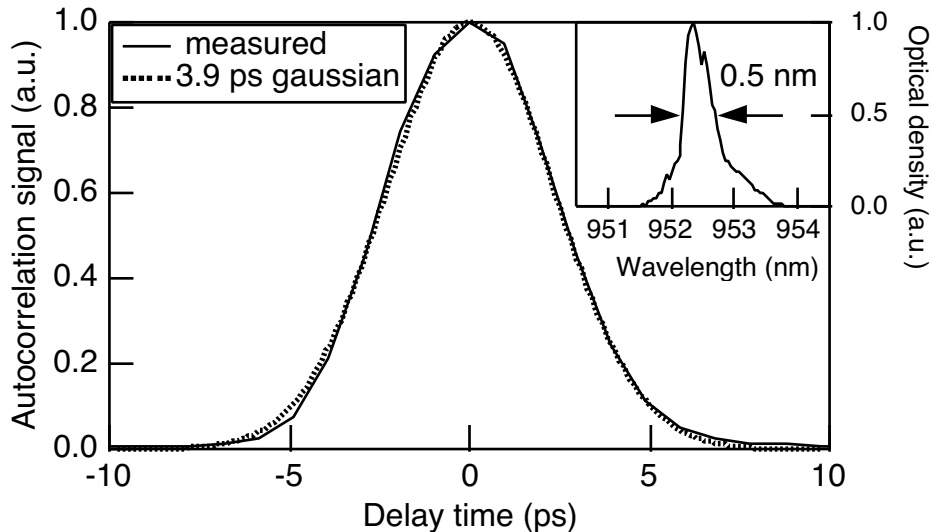


Figure 49. Autocorrelation trace at 530 mW. The solid line are the measured data and the dotted line is a fit assuming gaussian pulse shape. The inset is the optical spectrum taken at a resolution of 0.1 nm.

In Figure 49 the autocorrelation is shown at an average output power of 530 mW. Assuming a gaussian pulse shape results in a pulse duration of 3.9 ps. The inset depicts the optical spectrum of the laser with a width of 0.5 nm at a laser wavelength of 952 nm taken with a optical spectrum analyzer with a resolution of 0.1 nm. The time-bandwidth product is 0.65, 1.5 times over the Fourier limit. In Figure 50 the microwave spectrum of the laser output is shown. The spectrum is free of noise down to the detection limit of $-55\ \text{dBc}$ at a resolution of 300 kHz and the inset shows the signals at the harmonics of the repetition rate of 5.9533 GHz. The output beam is measured to be linearly polarized

with a ratio better than 100:1. The M^2 values are in both directions <1.05 and are measured by scanning the beam profile with the knife-edge method.

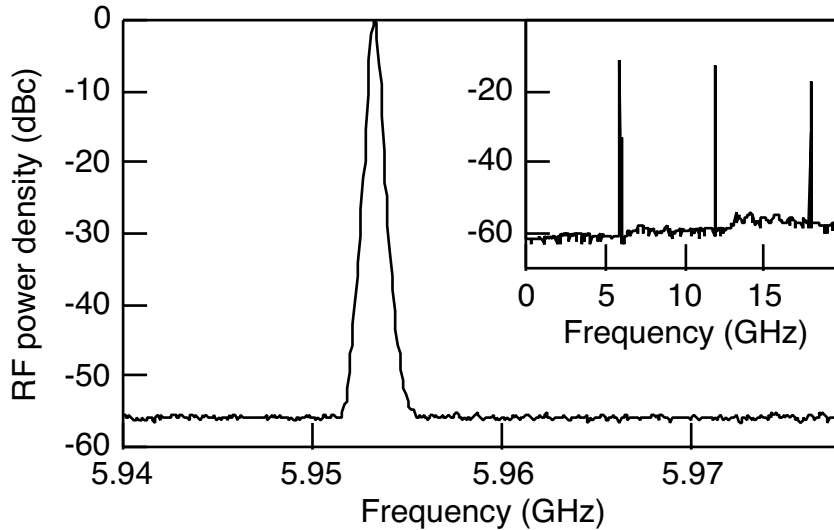


Figure 50. Radio frequency spectrum of the laser output at 530mW. The trace is measured at a resolution of 300 kHz. The inset shows the signals at the harmonics of the repetition rate of 5.9533 GHz.

According to the analysis in Section 3.2 the thermal impedance is dominated by the heat sink with such a large pump spot. A smaller spot would allow a reduced temperature in the active area and thereby increase the efficiency of the laser. We use an aperture to clip part of the pump beam and to achieve a pump spot with radii of $160\ \mu\text{m} \times 206\ \mu\text{m}$. Indeed, in a continuous-wave configuration with the SESAM replaced with a high reflector and using a piece of the wafer with higher efficiency, we can achieve 2.2 W output power at the full available pump power of 15.8 W. In this case the laser is allowed to run with a mode overlapping the pumped area more efficiently. Adjusting the cavity to force the laser to operate on the fundamental transverse mode reduces output by 35%. Introducing the saturable absorber reduces power by another 34% resulting in an output power of 950 mW. The autocorrelation trace and the optical spectrum of this pulse are shown in Figure 51. With 15 ps pulse duration (assuming sech^2) at a wavelength of 957 nm, the pulses are much longer, while the optical spectrum is even broader, indicating a strong chirp.

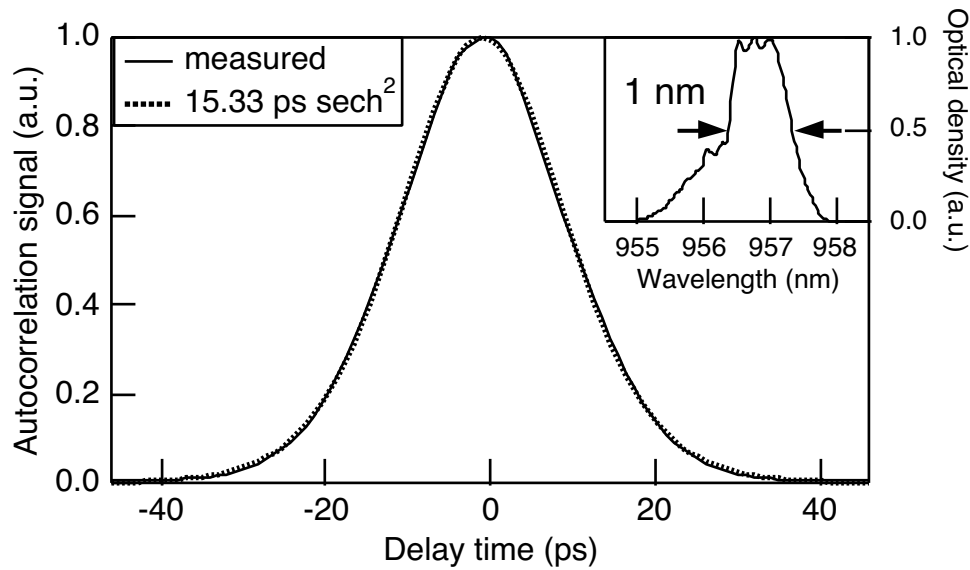


Figure 51. Autocorrelation trace at 950 mW. The solid line are the measured data and the dotted line is a fit assuming sech^2 pulse shape. The inset is the optical spectrum taken at a resolution of 0.1 nm.

There seem to be two regimes of pulses: close to transform limited pulses and strongly chirped ones (the first can be best fitted assuming gaussian pulse shape while sech^2 seems better for the second). The gain structures have a large variation of the GDD in the vicinity of the laser wavelength (e.g. the design used in the 950 mW experiment has a GDD of 0 fs^2 at 950 nm while a maximum of 2000 fs^2 is found at 956 nm). We believe the variation of the GDD together with the observation of different pulse regimens is a strong indication for a similar pulse shaping mechanism as described by Martinez et al. [94] (see Section 4.1). Indeed, numerical simulations suggest that quasi-solitons can be achieved [109], but further investigations will be needed to fully understand the mechanism.

CHAPTER 5

Summary and Outlook

We have investigated two laser sources giving pulse trains with repetition rates reaching from the kilohertz to the gigahertz range.

A laser emitting pulses at a rate of ≈ 1 kHz with peak powers exceeding 10 kW was presented. We used a microchip laser setup facilitating sub-nanosecond pulses from a Q-switched laser in the ‘eye-safe’ wavelength region at $1.5 \mu\text{m}$. It was shown that the damage of InP/InGaAsP semiconductor saturable absorber mirrors (SESAMs) is basically determined by a critical fluence in the order of $10 - 100 \text{ mJ/cm}^2$ for a single pulse within the absorber layer. We can obtain significantly higher pulse energies of up to $11.2 \mu\text{J}$ from such microchip lasers by using antiresonant SESAM designs with relatively high top mirror reflectivity and a thick absorber layer, so that the fluence within the absorber layer is much smaller than the fluence incident on the SESAM. The described performance characteristics make these miniature lasers an excellent pulse source for applications like range finding and three-dimensional imaging.

The other main focus of this thesis is the development of a high power mode-locked semiconductor laser. We used the approach of an optically pumped vertical-external-cavity surface-emitting laser (VECSEL) to generate in a diffraction-limited beam with high average power. Design considerations and the thermal properties of the gain element were discussed in detail. We gave a compilation of methods used to grow and fabricate the gain devices and presented characterization methods to control accuracy of the growth, surface quality after epitaxial lift-off, and the quality of the quantum wells. Passive mode locking of VECSELs was demonstrated successfully and the highest average power from a mode-locked semiconductor laser is reported. We achieved 950 mW average power for a pulse duration of 15 ps at a repetition rate of 6 GHz. Shorter pulses with 4 ps duration are achieved with 530 mW and the beam was measured to be close to the diffraction limit with linear polarization. In both cases the wavelength was near 950 nm.

Photoluminescence microscopy reveals some dark line defects caused by accumulated lattice misfit. Incorporation of strain-compensating layers will improve both efficiency and reliability of the gain structure. We expect that even multiwatt operation is feasible with the VECSEL approach.

We presented indications for a pulse shaping mechanism similar to the one described by Martinez et al. for dye lasers [94]. Quasi-soliton formation is described there by an interplay of group delay dispersion and gain saturation induced refractive index change. Further investigation of the pulse formation mechanism in VECSELS might lead to sub-picosecond pulses with nearly no chirp.

In the presented work the stronger saturation of the absorber was achieved with a smaller laser mode area on the SESAM than on the gain structure. Ways to reduce the intrinsic saturation fluence of the absorber (e.g. using quantum dots instead of quantum wells) or to increase the intensity seen by the absorber by resonant structures might be explored in future devices. A low saturation fluence of the absorber enables incorporation of the absorber into the gain structure. An even simpler setup with the ability to push the repetition rate to 100 GHz seems to be feasible with such a device.

The flexibility achieved with semiconductor compounds allows reaching similar performance with the VECSEL approach in other wavelength regions. The telecommunication wavelengths around $1.5\ \mu\text{m}$ and $1.3\ \mu\text{m}$ are of special interest. These sources would allow to realize new schemes proposed for high throughput data transmission requiring higher pulse energies [13]. The possibility for efficient single-pass frequency conversion makes laser wavelength around 1250 nm, 1050 nm and 910 nm very attractive for red, green and blue generation. These visible sources could be used for the development of laser based home cinema with far better color saturation, resolution and brightness than with today's projection techniques.

References

1. R. Ell, U. Morgner, F. X. Kärtner, J. G. Fujimoto, E. P. Ippen, V. Scheuer, G. Angelow, T. Tschudi, M. J. Lederer, A. Boiko, B. Luther-Davies, "Generation of 5-fs pulses and octave-spanning spectra directly from a Ti:sapphire laser," *Opt. Lett.* **26**, p. 373 (2001).
2. D. H. Sutter, L. Gallmann, N. Matuschek, F. Morier-Genoud, V. Scheuer, G. Angelow, T. Tschudi, G. Steinmeyer, U. Keller, "Sub-6-fs pulses from a SESAM-assisted Kerr-lens modelocked Ti:sapphire laser: At the frontiers of ultrashort pulse generation," *Appl. Phys. B* **70**, p. S5 (2000).
3. U. Morgner, S. H. Cho, J. Fini, F. X. Kärtner, H. A. Haus, J. G. Fujimoto, E. P. Ippen, V. Scheuer, M. Tilsch, T. Tschudi, "5.5-fs pulses from a Kerr-lens modelocked Ti:sapphire laser," in *OSA Technical Digest on Advanced Solid-State Lasers*, (OSA, Washington DC, 1999), paper TuA3, 1999.
4. A. Shirakawa, I. Sakane, M. Takasaka, T. Kobayashi, "Sub-5-fs visible pulse generation by pulse-front-matched noncollinear optical parametric amplification," *Appl. Phys. Lett.* **74**, 16, p. 2268 (1999).
5. A. Baltuska, Z. Wei, M. S. Pshenichnikov, D. A. Wiersma, R. Szipöcs, "All-solid-state cavity dumped sub-5-fs laser," *Appl. Phys. B* **65**, p. 175 (1997).
6. M. Nisoli, S. De Silvestri, O. Svelto, R. Szipöcs, K. Ferenz, C. Spielmann, S. Sartania, F. Krausz, "Compression of High Energy Laser Pulses Below 5 fs," *Optics Lett.* **22**, p. 522 (1997).
7. S. Arahira, Y. Matsui, Y. Ogawa, "Mode-locking at very high repetition rates more than terahertz in passively mode-locked distributed-Bragg-reflector laser diodes," *IEEE J. Quantum Electron.* **32**, 7, p. 1211 (1996).
8. U. Keller, D. A. B. Miller, G. D. Boyd, T. H. Chiu, J. F. Ferguson, M. T. Asom, "Solid-state low-loss intracavity saturable absorber for Nd:YLF lasers: an antiresonant semiconductor Fabry-Perot saturable absorber," *Opt. Lett.* **17**, p. 505 (1992).

9. U. Keller, K. J. Weingarten, F. X. Kärtner, D. Kopf, B. Braun, I. D. Jung, R. Fluck, C. Hönninger, N. Matuschek, J. Aus der Au, "Semiconductor saturable absorber mirrors (SESAMs) for femtosecond to nanosecond pulse generation in solid-state lasers," *IEEE J. Sel. Top. Quantum Electron.* **2**, 3, p. 435 (1996).
10. U. Keller, in *Nonlinear Optics in Semiconductors* E. Garmire, A. Kost, Eds. (Academic Press, Inc., Boston, 1999), **59**, pp. 211.
11. V. P. Gapontsev, S. M. Matitsin, A. A. Isineev, V. B. Kravchenko, "Erbium glass lasers and their applications," *Optics and Laser Technology* **14**, p. 189 (1982).
12. Kigre Inc., QX Laser Glasses, Data Sheet (1996).
13. B. C. Collings, M. L. Mitchell, L. Boivin, W. H. Knox, "A 1021 Channel WDM System," *IEEE Photon. Tech. Lett.* **12**, 7, p. 906 (2000).
14. R. Wallenstein, "Advanced solid state sources for high power visible light generation," in *Conference on Electro-Optics*, paper CThC3, 2001.
15. A. Nebel, B. Ruffing, R. Wallenstein, "Diode pumping sharpens large laser displays," *Laser Focus World* **35**, 5, p. 263 (2001).
16. F. Kuznetsov, F. Hakimi, R. Sprague, A. Mooradian, "High-Power (>0.5-W CW) Diode-Pumped Vertical-External-Cavity Surface-Emitting Semiconductor Lasers with Circular TEM₀₀ Beams," *IEEE Photon. Technol. Lett.* **9**, 8, p. 1063 (1997).
17. F. Kuznetsov, F. Hakimi, R. Sprague, A. Mooradian, "Design and Characteristics of High-Power (>0.5-W CW) Diode-Pumped Vertical-External-Cavity Surface-Emitting Semiconductor Lasers with Circular TEM₀₀ Beams," *IEEE J. Sel. Top. Quantum Electron.* **5**, 3, p. 561 (1999).
18. W. J. Alford, T. D. Raymond, M. H. Crawford, A. A. Allerman, "High power (>1 W), good beam quality surface-emitting semiconductor laser," in *OSA Annual Meeting and Exhibit 2000*, paper WS3, 2000.
19. T. D. Raymond, W. J. Alford, M. H. Crawford, A. A. Allerman, "Intracavity frequency doubling of a diode-pumped external-cavity surface-emitting semiconductor laser," *Optics Letters* **24**, 13, p. 1127 (1999).

20. J. J. Zayhowski, A. L. Wilson, "Miniature sources of subnanosecond 1.4-4.3 μm pulses with high peak power," in *Advanced Solid State Lasers*, (OSA), p. 308, 2000.
21. J. J. Zayhowski, "Periodically poled lithium niobate optical parametric amplifiers pumped by high-power passively Q-switched microchip lasers," *Opt. Lett.* **22**, 3, p. 169 (1997).
22. J. J. Zayhowski, S. C. Buchter, A. L. Wilson, "Miniature Gain Switched Lasers," in *Advanced Solid-State Lasers*, (OSA), 308, 2001.
23. K. V. Yumashev, I. A. Denisov, N. N. Posnov, V. P. Mikhailov, R. Moncorgé, D. Vivien, B. Ferrand, Y. Guyot, "Nonlinear spectroscopy and passive Q-switching operation of a $\text{Co}^{2+}:\text{LaMgAl}_{11}\text{O}_{19}$," *J. Opt. Soc. Am. B* **16**, 12, p. 2189 (1999).
24. P. Thony, B. Ferrand, E. Molva, "1.55 μm passive Q-switched microchip laser," in *Advanced Solid-state Lasers*, (OSA), 150, 1998.
25. K. Spariosu, R. D. Stultz, M. Birnbaum, T. H. Allik, J. A. Hutchinson, "Er: $\text{Ca}_5(\text{PO}_4)_3\text{F}$ saturable-absorber Q switch for the Er:glass laser at 1.53 μm ," *Appl. Phys. Lett.* **62**, 22, p. 2763 (1993).
26. R. D. Stultz, M. B. Camargo, M. Birnbaum, "Passive Q-switch at 1.53 μm using divalent uranium ions in calcium fluoride," *J. Appl. Phys.* **78**, 5, p. 2959 (1995).
27. R. D. Stultz, M. B. Camargo, M. Lawler, D. Rockafellow, M. Birnbaum, "Diode-Pumped Er:Yb:Glass Mini-Transmitter," in *Advanced Solid State Lasers*, p. 155, 1998.
28. R. D. Stultz, M. B. Camargo, S. T. Montgomery, M. Birnbaum, K. Spariosu, "U:SrF efficient saturable absorber Q switch for the 1.54 μm erbium:glass laser," *Appl. Phys. Lett.* **64**, 8, p. 948 (1994).
29. M. Birnbaum, M. B. Camargo, S. Lee, F. Unlu, R. D. Stultz, "Co:ZnSe saturable absorber Q-switch for the 1.54 μm Er/Yb:glass laser," *OSA TOPS on ASSL* **10**, p. 148 (1997).
30. A. V. Podlipensky, V. G. Shcherbitsky, N. V. Kuleshov, V. P. Mikhailov, V. I. Levchenko, V. N. Yakimovich, " $\text{Cr}^{2+}:\text{ZnSe}$ and $\text{Co}^{2+}:\text{ZnSe}$ saturable-absorber Qswitches for 1.54- μm Er:glass," *Opt. Lett.* **24**, 14, p. 960 (1999).

31. R. Fluck, R. Häring, R. Paschotta, E. Gini, H. Melchior, U. Keller, "Eyesafe pulsed microchip laser using semiconductor saturable absorber mirrors," *Appl. Phys. Lett.* **72**, p. 3273 (1998).
32. S. Kück, K. Petermann, U. Pohlmann, G. Huber, "Near-infrared emission of Cr⁴⁺-doped garnets: Lifetimes, quantum efficiencies, and emission cross sections," *Phys. Rev. B* **51**, p. 17323 (1995).
33. A. Diening, P. E.-A. Möbert, G. Huber, "Diode-pumped continuous-wave, quasi-continuous wave, and Q-switched laser operation of Yb³⁺,Tm³⁺:YLiF₄ at 1.5 and 2.3 μm," *J. Appl. Phys.* **84**, 11, p. 5900 (1998).
34. R. Brinkmann, W. Sohler, H. Suche, "Continuous-wave erbium-diffused LiNbO₃ waveguide laser," *Electron. Lett.* **27**, 5, p. 415 (1991).
35. S. Taccheo, P. Laporta, S. Longhi, O. Svelto, C. Svelto, "Diode-pumped bulk erbium-ytterbium lasers," *Appl. Phys. B* **63**, 5, p. 425 (1996).
36. G. J. Spühler, R. Paschotta, R. Fluck, B. Braun, M. Moser, G. Zhang, E. Gini, U. Keller, "Experimentally confirmed design guidelines for passively Q-switched microchip lasers using semiconductor saturable absorbers," *J. Opt. Soc. Am. B* **16**, 3, p. 376 (1999).
37. B. Braun, F. X. Kärtner, M. Moser, G. Zhang, U. Keller, "56 ps passively Q-switched diode-pumped microchip laser," *Opt. Lett.* **22**, p. 381 (1997).
38. B. Braun, F. X. Kärtner, U. Keller, J.-P. Meyn, G. Huber, "Passively Q-switched 180 ps Nd:LSB microchip laser," *Opt. Lett.* **21**, p. 405 (1996).
39. R. Fluck, B. Braun, E. Gini, H. Melchior, U. Keller, "Passively Q-switched 1.34 μm Nd:YVO₄ microchip laser using semiconductor saturable-absorber mirrors," *Opt. Lett.* **22**, p. 991 (1997).
40. J. J. Zayhowski, A. Mooradian, "Single-frequency microchip Nd lasers," *Opt. Lett.* **14**, p. 24 (1989).
41. F. Salin, J. Squier, "Gain guiding in solid-state lasers," *Opt. Lett.* **17**, p. 1352 (1992).

42. J. J. Zayhowski, "Thermal Guiding in Microchip Lasers," in *Advanced Solid-State Lasers*, p. 9, 1990.
43. R. Häring, R. Paschotta, E. Gini, H. Melchior, U. Keller, "Sub-nanosecond pulses from passively Q-switched microchip lasers at 1.53 μm ," in *Conference on Lasers and Electro-Optics CLEO '99*, (OSA), 518, 1999.
44. J. J. Zayhowski, P. L. Kelley, "Optimization of Q-switched Lasers," *IEEE J. Quantum Electronics* **27**, p. 2220 (1991).
45. L. R. Brovelli, U. Keller, T. H. Chiu, "Design and Operation of Antiresonant Fabry-Perot Saturable Semiconductor Absorbers for Mode-Locked Solid-State Lasers," *J. Opt. Soc. Am. B* **12**, 2, p. 311 (1995).
46. B. C. Stuart, M. D. Feit, S. Herman, A. M. Rubenchik, B. W. Shore, M. D. Perry, "Nanosecond-to-femtosecond laser-induced breakdown in dielectrics," *Phys. Rev. B* **53**, 4, p. 1749 (1996).
47. A. Mar, R. Helkey, W. X. Zou, D. B. Young, J. E. Bowers, "High-power modelocked semiconductor lasers using flared waveguides," *Appl. Phys. Lett.* **66**, p. 3558 (1995).
48. L. Goldberg, D. Mehuys, D. Welch, "High Power Mode-locked Compound Laser using a Tapered Semiconductor Amplifier," *IEEE Photon. Technol. Lett.* **6**, 9, p. 1070 (1994).
49. A. Mar, R. Helkey, J. Bowers, D. Mehuys, D. Welch, "Modelocked Operation of a Master Oscillator Power Amplifier," *IEEE Photonics Technology Lett.* **6**, p. 1067 (1994).
50. S. Gee, G. Alphonse, J. Connolly, P. Delfyett, "High-Power Mode-Locked External Cavity Semiconductor Laser Using Inverse Bow-Tie Semiconductor Optical Amplifiers," *IEEE J. Sel. Top. Quantum Electron.* **4**, 2, p. 209 (1998).
51. M. Brunner, K. Gulden, R. Hövel, M. Moser, M. Ilegems, "Thermal lensing effects in small oxide confined vertical-cavity surface-emitting lasers," *Appl. Phys. Lett.* **76**, 1, p. 7 (2000).
52. R. G. Ulbrich, in *Optical Nonlinearities and Instabilities in Semiconductors* H. Haug, Eds. (Academic, New York, 1988)

53. H. J. Unold, M. C. Riedl, S. W. Z. Mahmoud, R. Jäger, K. J. Ebeling, "Long monolithic cavity VCSEL for high singlemode output power," *Electron. Lett.* **37**, 3, p. 178 (2001).
54. M. Grabherr, R. Jäger, M. Miller, C. Thalmaier, J. Heerlein, R. Michalzik, K. J. Ebeling, "Bottom-emitting VCSEL for high cw optical output power," *IEEE Photon. Technol. Lett.* **10**, 8, p. 1061 (1998).
55. E. Yablonovitch, E. O. Kane, "Reduction of Lasing Threshold Current Density by Lowering the Valence Band Effective Mass," *Journal of Lightwave Technology* **LT-4**, 5, p. 504 (1986).
56. E. Yablonovitch, E. O. Kane, "Correction to 'Reduction of Lasing Threshold Current Density by Lowering the Valence Band Effective Mass'," *Journal of Lightwave Technology* **LT-4**, 7, p. 961 (1986).
57. A. R. Adams, "Band-structure engineering for low-threshold high-efficiency semiconductor lasers," *Electron. Lett.* **22**, 5, p. 249 (1986).
58. A. R. Adams, L. G. Shantharama, R. J. Nicholas, C. K. Sarkar, "Pressure induced changes in the effective mass of electrons in GaAs, InP and (GaIn)(AsP)/InP," *Physica-B-&-C* **139B+C & 140B+C**, 1-3, p. 401 (1986).
59. P. S. Zory, *Quantum Well Lasers*. P. F. Liao, P. L. Kelley, Eds., Quantum Electronics - Principles and Applications (Academic Press, Inc., San Diego, 1993)
60. S. Adachi, Eds., *Properties of Aluminium Gallium Arsenide*, vol. 7 (INSPEC, London, 1993).
61. E. Veuhoff, in *Handbook of Compound Semiconductors* P. H. Holloway, G.E. McGuire, Eds. (Noyes Publications, New Jersey, 1995) pp. 29.
62. M. J. Ludowise, "Metalorganic chemical vapor deposition of III-V semiconductors," *J. Appl. Phys.* **58**, 8, p. R31 (1985).
63. C. A. Wang, S. H. Groves, J. H. Reinold, D. R. Calawa, "Critical Layer Thickness of Strained-Layer InGaAs/GaAs Multiple Quantum Wells Determined by Double-Crystal X-Ray Diffraction," *Journal of Electronic Materials* **22**, 11, p. 1365 (1993).

64. M. A. Afromowitz, "Refractive index of Ga(1-x)Al(x)As," *Solid-State Communications* **15**, p. 59 (1974).
65. M. A. Afromowitz, "Refractive index of In(x)Ga(1-x)As," *Japanese Journal of Applied Physics* **17**, p. 1813 (1978).
66. R. J. K. Wassink, *Soldering in Electronics* (Electrochemical Publications Ltd, Ayr, Scotland, 1989)
67. W. W. So, C. C. Lee, "Fluxless Process of Fabricating In-Au Joints on Copper Substrates," *IEEE Trans. Comp. Packag. Technol.* **23**, 2, p. 377 (2000).
68. J. J. LePore, "An improved technique for selective etching of GaAs and Ga(1-x)Al(x)As," *J. Appl. Phys.* **51** (12), p. 6441 (1980).
69. R. A. Logan, F. K. Reinhart, "Optical waveguides in GaAs-AlGaAs epitaxial layers," *J. Appl. Phys.* **44**, 9, p. 4172 (1973).
70. W. D. Johnston, W. M. Callahan, B. I. Miller, "Observation of dark-line degradation sites in AlGaAs/GaAs DH laser material by etching and phase-contrast microscopy," *J. Appl. Phys.* **45**, 2, p. 505 (1974).
71. H. Wang, A. A. Hopgood, G. I. Ng, "Analysis of dark-line defect growth suppression in In_xGa_{1-x}As/GaAs strained heterostructures," *J. Appl. Phys.* **81**, 7, p. 3117 (1997).
72. I. J. Fritz, "role of experimental resolution in measurements of critical layer thickness for strained-layer epitaxy," *Appl. Phys. Lett.* **51**, 14, p. 1080 (1987).
73. J. W. Matthews, A. E. Blakeslee, "Defects in epitaxial multilayers," *Journal of Crystal Growth* **27**, p. 118 (1974).
74. T. Suzuki, M. Ogawa, "Degradation of photoluminescence intensity caused by excitation-enhanced oxidation of GaAs surfaces," *Appl. Phys. Lett.* **31**, 7, p. 473 (1977).
75. T. Yuasa, M. Ogawa, K. Endo, H. Yonezu, "Degradation of (AlGa)As DH lasers due to facet oxidation," *Appl. Phys. Lett.* **32**, 2, p. 119 (1978).

76. M. Gasser, E. E. Latta, International Business Machines Corporation, Armonk, N.Y., Patent Number 5 063 173 (1990).
77. P. T. Ho, L. A. Glasser, E. P. Ippen, H. A. Haus, "Picosecond pulse generation with a cw GaAlAs laser diode," *Appl. Phys. Lett.* **33**, p. 241 (1978).
78. Y. Silberberg, P. W. Smith, D. J. Eilenberger, D. A. B. Miller, A. C. Gossard, W. Wiegmann, "Passive modelocking of a semiconductor diode laser," *Optics Letters* **9**, p. 507 (1984).
79. J. P. van der Ziel, W. T. Tsang, R. A. Logan, R. M. Mikulyak, W. M. Augustyniak, "Subpicosecond pulses from passively modelocked GaAs buried optical guide semiconductor lasers," *Appl. Phys. Lett.* **39**, p. 525 (1981).
80. S. Gee, G. Alphonse, J. Connolly, C. Barty, P. Delfyett, "Ultrashort Pulse Generation by Intracavity Spectral Shaping and Phase Compensation of External-Cavity Modelocked Semiconductor Lasers," *IEEE J. Quantum Electron.* **36**, 9, p. 1035 (2000).
81. W. H. Xiang, S. R. Friberg, K. Watanabe, S. Machida, Y. Sakai, H. Iwamura, Y. Yamamoto, "Sub-100 femtosecond pulses from an external-cavity surface-emitting InGaAs/InP multiple quantum well laser with soliton effect-compression," *Appl. Phys. Lett.* **59**, 17, p. 2076 (1991).
82. W. Jiang, J. Bowers, in *Compact Sources of Ultrashort Pulses* I. I. N. Duling, Eds. (Cambridge University Press, New York, 1995) pp. 208.
83. M. A. Holm, P. Cusumano, D. Burns, A. I. Ferguson, M. D. Dawson, "Mode-locked operation of a diode-pumped, external-cavity GaAs/AlGaAs surface emitting laser," in *Conference on Lasers and Electro-Optics, CLEO'99*, 1999 OSA Technical Digest Series (Optical Society of America, Washington D.C., 1999), paper CTuK63, 1999.
84. J. Aus der Au, G. J. Spühler, T. Südmeyer, R. Paschotta, R. Hövel, M. Moser, S. Erhard, M. Karszewski, A. Giesen, U. Keller, "16.2 W average power from a diode-pumped femtosecond Yb:YAG thin disk laser," *Opt. Lett.* **25**, p. 859 (2000).

85. G. J. Spühler, T. Südmeyer, R. Paschotta, M. Moser, K. J. Weingarten, U. Keller, "Passively mode-locked high-power Nd:YAG lasers with multiple laser heads," *Appl. Phys. B* **71**, 1, p. 19 (2000).
86. D. Burns, M. Hetterich, A. I. Ferguson, E. Bente, M. D. Dawson, J. I. Davies, S. W. Bland, "High-average-power (>20 W) Nd:YVO₄ lasers mode locked by strain-compensated saturable Bragg reflectors," *J. Opt. Soc. Am. B* **17**, p. 919 (2000).
87. L. Krainer, R. Paschotta, M. Moser, U. Keller, "77 GHz soliton modelocked Nd:YVO₄ laser," *Electron. Lett.* **36**, 22, p. 1846 (2000).
88. C. Hönninger, R. Paschotta, F. Morier-Genoud, M. Moser, U. Keller, "Q-switching stability limits of continuous-wave passive mode locking," *J. Opt. Soc. Am. B* **16**, 1, p. 46 (1999).
89. H. A. Haus, "Theory of modelocking with a fast saturable absorber," *J. Appl. Phys.* **46**, p. 3049 (1975).
90. H. A. Haus, J. G. Fujimoto, E. P. Ippen, "Structures for additive pulse modelocking," *J. Opt. Soc. Am. B* **8**, p. 2068 (1991).
91. F. X. Kärtner, U. Keller, "Stabilization of soliton-like pulses with a slow saturable absorber," *Opt. Lett.* **20**, 1, p. 16 (1995).
92. F. X. Kärtner, I. D. Jung, U. Keller, "Soliton Modelocking with Saturable Absorbers," *IEEE J. Sel. Topics in Quantum Electron.* **2**, 3, p. 540 (1996).
93. O. E. Martinez, R. L. Fork, J. P. Gordon, "Theory of passively modelocked lasers including self-phase modulation and group-velocity dispersion," *Optics Lett.* **9**, p. 156 (1984).
94. O. E. Martinez, R. L. Fork, J. P. Gordon, "Theory of passively modelocked lasers for the case of a nonlinear complex propagation coefficient," *J. Opt. Soc. Am. B* **2**, p. 753 (1985).
95. R. Paschotta, U. Keller, "Passive mode locking with slow saturable absorbers," to appear in *Appl. Phys. B*, p. (2001).

96. G. H. C. New, "Modelocking of quasi-continuous lasers," *Opt. Commun.* **6**, p. 188 (1972).
97. H. A. Haus, "Theory of Mode Locking with a Slow Saturable Absorber," *IEEE J. Quantum Electron.* **11**, p. 736 (1975).
98. K. J. Blow, B. P. Nelson, "Improved modelocking of an F-center laser with a nonlinear nonsoliton external cavity," *Opt. Lett.* **13**, p. 1026 (1988).
99. P. N. Kean, X. Zhu, D. W. Crust, R. S. Grant, N. Landford, W. Sibbett, "Enhanced modelocking of color center lasers," *Opt. Lett.* **14**, p. 39 (1989).
100. E. P. Ippen, H. A. Haus, L. Y. Liu, "Additive Pulse Modelocking," *JOSA B* **6**, p. 1736 (1989).
101. D. E. Spence, P. N. Kean, W. Sibbett, "60-fsec pulse generation from a self-mode-locked Ti:sapphire laser," *Opt. Lett.* **16**, p. 42 (1991).
102. U. Keller, G. W. 'tHooft, W. H. Knox, J. E. Cunningham, "Femtosecond Pulses from a Continuously Self-Starting Passively Mode-Locked Ti:Sapphire Laser," *Opt. Lett.* **16**, p. 1022 (1991).
103. D. K. Negus, L. Spinelli, N. Goldblatt, G. Feugnet, in *Advanced Solid-State Lasers* G. Dubé, L. Chase, Eds. (Optical Society of America, Washington, D.C., 1991), **10**, pp. 120.
104. F. Salin, J. Squier, M. Piché, "Modelocking of Ti:Sapphire lasers and self-focusing: a Gaussian approximation," *Optics Lett.* **16**, p. 1674 (1991).
105. M. Piché, F. Salin, "Self-mode locking of solid-state lasers without apertures," *Opt. Lett.* **18**, p. 1041 (1993).
106. U. Morgner, F. X. Kärtner, S. H. Cho, Y. Chen, H. A. Haus, J. G. Fujimoto, E. P. Ippen, V. Scheuer, G. Angelow, T. Tschudi, "Sub-two-cycle pulses from a Kerr-lens mode-locked Ti:sapphire laser," *Opt. Lett.* **24**, p. 411 (1999).
107. D. H. Sutter, G. Steinmeyer, L. Gallmann, N. Matuschek, F. Morier-Genoud, U. Keller, V. Scheuer, G. Angelow, T. Tschudi, "Semiconductor saturable-absorber mirror-assisted Kerr-lens mode-locked Ti:sapphire laser producing pulses in the two-cycle regime," *Opt. Lett.* **24**, 9, p. 631 (1999).

108. I. D. Jung, F. X. Kärtner, L. R. Brovelli, M. Kamp, U. Keller, "Experimental verification of soliton modelocking using only a slow saturable absorber," *Opt. Lett.* **20**, p. 1892 (1995).
109. R. Paschotta, R. Häring, U. Keller, A. Garnache, S. Hoogland, A. C. Tropper, "Soliton-like pulses formation mechanism in passively mode-locked surface-emitting semiconductor lasers," *in preparation for Appl. Phys. B*, p. (2002).
110. R. Häring, R. Paschotta, F. Morier-Genoud, U. Keller, J. S. Roberts, S. Hoogland, S. Dhanjal, A. C. Tropper, "Passively mode-locked diode-pumped surface-emitting semiconductor laser," *in Advanced Solid-State Lasers*, (Optical Society of America, Washington, DC, 2000), TuC5, 2000.
111. S. Hoogland, S. Dhanjal, A. C. Tropper, S. J. Roberts, R. Häring, R. Paschotta, U. Keller, "Passively mode-locked diode-pumped surface-emitting semiconductor laser," *IEEE Photon. Technol. Lett.* **12**, 9, p. 1135 (2000).
112. R. Häring, R. Paschotta, F. Morier-Genoud, U. Keller, A. Garnache, U. Oesterle, J. S. Roberts, S. Hoogland, S. Dhanjal, A. C. Tropper, "Passively mode-locked diode-pumped surface-emitting semiconductor laser," *in Conference on Lasers and Electro-Optics CLEO'00*, (Optical Society of America, Washington, D. C., 2000), 2000.
113. A. Garnache, A. A. Kachnov, F. Stoeckel, R. Houdre, "Diode-pumped broadband vertical external cavity surface emitting semiconductor laser applied to high sensitivity intracavity absorption spectroscopy," *JOSA B* **17**, 9, p. 1589 (2000).
114. R. Häring, R. Paschotta, E. Gini, F. Morier-Genoud, H. Melchior, D. Martin, U. Keller, "Picosecond surface-emitting semiconductor laser with >200 mW average power," *Electron. Lett.* **37**, 12, p. 766 (2001).

Curriculum Vitae

Reto Andreas Häring

Born 9. January 1971 in Basel, Switzerland
Scheuchzerstrasse 161, 8057 Zürich, Switzerland
Swiss citizenship

Education and work experience

May 1976- April 1987	Compulsory School in Arisdorf and Liestal
May 1987 - Dec. 1991	Gymnasium Liestal
Feb. 1992 - June 1992	Military service
Oct. 1992 – Sept. 1997	Higher education in physics at the Swiss Federal Institute of Technology, ETH Zürich
Jan. 1995 – June 1995	Exchange program with the Norwegian University of Science and Technology (NTNU, formerly NTH) in Trondheim, Norway
July 1995 – Sept. 1995	Practical training at NAGRA (Swiss National Cooperative for the Disposal of Radioactive Waste) Topic: correlation of compositions of radioactive waste from different sources
Oct. 1997	Diploma in physics Diploma Thesis under the direction of Prof. Dr. Ursula Keller: “Pulsed Pumping of Passively Q-switched Microchip Lasers”
Dec. 1997 – Dec. 2001	PhD studies at the Swiss Federal Institute of Technology, ETH Zürich, under the direction of Prof. Dr. Ursula Keller <ul style="list-style-type: none">• Passively Q-switching of microchip lasers using semiconductor saturable absorber mirrors (SESAMs)• Vertical-External-Cavity Surface-Emitting Lasers (VECSEL): design, processing and characterization of these devices• Passively mode locking of VECSELs

Danksagung

Allen Personen, die zum Erfolg dieser Doktorarbeit beigetragen haben, möchte ich an dieser Stelle danken. Insbesondere gilt mein Dank:

Prof. Dr. Ursula Keller für die Möglichkeit in ihrer Gruppe die vorliegende Doktorarbeit auszuführen und für ihre Unterstützung. Speziell erwähnt sei hier ihr tatkräftiger Einsatz für das Wachstum der Halbleiterstrukturen.

Prof. Dr. Anne C. Tropper, for sponsoring the idea of passively mode-locked VECSELS, for the collaboration and for being my co-examiner.

Dr. Rüdiger Paschotta für die kompetente Betreuung und für die Bereitschaft das Koreferat zu übernehmen.

Dr. Emilio Gini für die Verstärkerstrukturen und für die gute Betreuung bezüglich Halbleitermaterialien und -technologie.

Prof. Dr. Hans Melchior für die Möglichkeit seine Reinräume und sein MOCVD-System zu benützen.

Dr. Regula Fluck dafür, dass ich ihr Projekt mit gütegeschalteten Mikrochiplasern weiterführen konnte.

Meinen Nachfolgern Alex Aschwanden und Dirk Lorenser dafür, dass sie das VECSEL-Projekt übernehmen und weiterführen.

Den ehemaligen und jetzigen Mitgliedern der Gruppe für Ultrakurzzeit-Laserphysik (in alphabetischer Reihenfolge unter Vernachlässigung aller Titel):

Marc Achermann (ob sportlich oder spielerisch, mit oder ohne blaue Flecken, vielen Dank für die gute Zeit auch ausserhalb des Institutes), Gunnar Arisholm (det var fint å kunne prate litt Norsk igjen), Sebastian (Pep) Arlt, Jürg Aus der Au (Mostindien goes Hollywood), Jens Biegert, Bernd Braun, Felix Brunner (die einheimische Vertretung in der Gruppe), Rosmarie Ehrsam (der ruhende Pol auch bei heftiger Brandung), Henry Frick, Tobias Fritz, Lukas Gallmann (nächstes Mal begreife ich die Hintergründe bei so einem Zimmertausch schneller...), Markus Haiml (organisierte das Sozialleben der Gruppe), Christoph Hauri (sorgt für die Verstärkung), Florian Helbing, Clemens Hönninger, Edith Innerhofer (Frauenpower in unserem Büro, Highpower im Labor), Isabella Jung, Franz

Kärtner, Daniel Kopf, Lukas Krainer (going fast and easy), Jens Kunde (lass uns mal wieder einen Vulkan erklimmen), Steve Lecomte (der Gegenbeweis für den Röstigraben), Nicolai Matuschek, Francois Morier-Genoud (merci pour les SESAM), Bettina Nechay, Arti Prasad, Thomas Rupp, Birgit Schenkel (...und werde meine neugierigen Fragen stellen), Silke Schön, Uwe Siegner, Gabriel Spühler (wohl nicht nur in Jones' Tagebuch), Günter Steinmeyer, Thomas Südmeyer (versuchte auch die Akustik in den nichtlinearen Bereich zu bekommen), Dirk Sutter, John Tisch (uf dr Suächi nach dä schwiizer Wurzlä), Wouter Kornelis.

Allen die mir mit Rat und Tat zur Seite standen (in alphabetischer Reihenfolge unter Vernachlässigung aller Titel):

Richard Bartlome (für die Temperaturmessungen), Peter Brühwiler, Sukhminder Dhanjal (for the coloboration on the first mode-locked VECSEL), Martin Ebnöter (für das Wachsen), Andreas Fuhrer (für die Einführung ins AFM), Arnaud Garnache (pour les échantillons), Harald Hediger (und der Werkstatt für die präzise Ausführung mechanischer Bauteile), Sjoerd Hoogland (for the contibution to successfully mode-lock the first VECSEL), Martin Hofmann, Christoph Keck, Andreas Lange (für die Degradationsmessungen), Denis Martin, Michael Moser (für Tipps im Umgang mit GaAs), Siegfried Nau (für die Hinweise bezüglich Ätzprozessen), Bruno Nussberger (für die Lötapparatur), Ursula Oesterle (für das Wachsen der ersten eigenen Verstärkerstrukturen), Keith Price (for providing diamond submounts), Alok Rudra (für seine Tipps zum AlGaAs Wachstum), Hansruedi Scherrer (für die Metalisierungen und die Verwendung des Vakuumlötaufbaues), Wolfgang Schüsselbauer, Peter Selbmann, Alexei Sirbu (for bonding VECSEL structures to sapphire), Jean-Pierre Stucki (für die Politur der Kühlkörper), Wolfgang Stolz, Satoru Takagi (for providing Cu/W submounts), Stefan Weiss (für seine Hinweise zur Löttechnik).

Ganz besonders bedanken möchte ich mich bei meinen Eltern für die Unterstützung in allen Phasen meiner Studienzeit, bei meinen Geschwistern und bei Silke Wendt für ihr Verständnis für die Hoch und Tiefs einer Dissertation, für ihre moralische Unterstützung in den Tiefs und für Ihre Fähigkeit, meine Augen auch für anderes als die Laserphysik offen zu halten.

Zürich, Dezember 2001



Reto Häring